

BODY-WAVE AND EARTHQUAKE SOURCE STUDIES

Thesis by  
Ta-Liang Teng

In Partial Fulfillment of the Requirements  
For the Degree of  
Doctor of Philosophy

California Institute of Technology  
Pasadena, California

1966

(Submitted April 28, 1966)

## ACKNOWLEDGEMENT

The author is greatly indebted to Drs. Don L. Anderson and Frank Press for their advice and encouragement during the course of the present study.

The author's wife, Evelyn, is gratefully thanked for her confidence and her help in many matters.

Valuable discussions held with Drs. Ari Ben-Menahem, James Brune, David Harkrider, and Stewart Smith have in various stages benefited the present study. Thanks are also due to Mr. Laszlo Lenches, so helpful and competent, for his preparation of the figures.

This research was supported by the Advanced Research Project Agency and was monitored by the Air Force Office of Scientific Research under contract AF-49(638)-1337.

ABSTRACT

The present work concerns a study on the radiation and propagation of seismic body waves. Based on a reformulated seismic ray theory and supplemented by the results of several associated boundary value problems, a method of body wave equalization is described which enables the extrapolation of body-wave fields from one point to another.

Applications of the above method to studies of earthquake source mechanism and earth's structure, specifically its anelasticity, are presented. The findings for two deep-focus earthquakes can be summarized by: (1) a displacement dislocation source, or an equivalent double couple, can generally explain the observed radiation fields, (2) the source time functions can be explained by a build-up step  $(1 - e^{-t/\tau})H(t)$ , and  $\tau$  appears to be longer for larger earthquakes, (3) the total energy calculated from equalized spectrums is: for the Banda Sea earthquake ( $M = 6-1/4 - 6-3/4$ ),  $E = 1.01 \times 10^{22}$  ergs; and for the Brazil earthquake ( $M = 6-3/4 - 7$ ),  $E = 2.56 \times 10^{23}$  ergs.

From the spectral ratios of  $pP/P$  and  $P/P$ , it is found (1) that the upper 430 km of the mantle has an average  $Q_\alpha = 105$ , (2) that  $Q_\alpha$  increases very slowly until a depth of about 1000 km, and (3) that  $Q_\alpha$  rises rapidly beyond a depth of 1000 km, remains a high value in the lower mantle and drops sharply toward the core-mantle boundary.

TABLE OF CONTENTS

<u>Chapter</u>		<u>Page</u>
1	Introduction	1
	(1.1) Historical Background	1
	(1.2) Objectives	2
	(1.3) A Sketch of the Contents	4
	PART I. THEORY	8
2	Elastodynamic Source Theory and Body-Wave Radiation	9
	(2.1) Governing Differential Equations	9
	(2.2) Green's Dyadic for the Vector Helmholtz Equation	11
	(2.3) A Three Dimensional Representation Theorem	15
	(2.4) Radiation of Elastic Waves in an Infinite Medium	19
	(2.4.1) Green's Dyadics in an Infinite Medium	20
	(2.4.2) Radiation of Body Waves	23
	(2.4.2.a) Shear Fault	24
	(2.4.2.b) Tensile Fault	26
	(2.4.2.c) Explicit Expressions for the Radiation Patterns	28
	(2.4.3) Body Force Equivalents	30
	(2.4.4) Energy Calculation	36

<u>Chapter</u>		<u>Page</u>
3	Propagation of Body Waves	38
	(3.1) The Ray Theory as an Asymptotic Wave Theory	40
	(3.1.1) Historical Remarks	41
	(3.1.2) Asymptotic Ray Theory	43
	(3.2) Rays in a Spherically Symmetrical Medium	52
	(3.2.1) The Path and Transit Time of a Ray	53
	(3.2.2) The Geometrical Spreading	57
	(3.3) Attenuation Along the Ray	59
	(3.4) Reflection and Transmission Across Layered Boundaries	63
	(3.5) Diffraction by the Core of the Earth	66
4	Method of Body-Wave-Equalization	72
	(4.1) The Earth as a Linear System	72
	(4.2) Computation of the Transfer Functions	75
	PART II. APPLICATIONS	78
5	Mechanism of Deep Earthquakes from Spectrums of Isolated Body-Wave Signals -- The Banda Sea Earthquake of March 21, 1964	79
	(5.1) Introduction	79
	(5.2) Data	80
	(5.3) Data Analysis	82
	(5.3.1) Choice of the Time Window and its Effect on the Resulting Spectrum	82
	(5.3.2) Equalization of the Spectrums	84
	(5.3.3) Spectral Radiation Patterns of P Waves	86
	(5.3.4) Determination of Source Parameters	87

<u>Chapter</u>		<u>Page</u>
	(5.4) Auxiliary Studies	88
	(5.4.1) Radiation Pattern of S Waves	88
	(5.4.2) Results from First Motion	89
	(5.5) Time Function and Energy of the Source	90
6	Mechanism of Deep Earthquakes from Spectrum of Isolated Body-Wave Signals -- The Brazil Earthquake of November 9, 1963	93
	(6.1) Introduction	93
	(6.2) Data	94
	(6.3) Transfer Functions	95
	(6.4) Spectral Radiation Patterns and Source Parameters	97
	(6.5) Results from First Motion	101
	(6.6) Source Mechanism	102
7	Attenuation of Body Waves and an Attempt to Estimate the Q-Depth Structure in the Mantle	106
	(7.1) Introduction	106
	(7.2) Method of Spectral Ratios	107
	(7.3) Data Analysis - Spectral Ratios of P/P, S/P, pP/P	111
	(7.4) $\delta A_{pP/P}$ and the Average $Q_a$ in the Upper Mantle	115
	(7.5) $\delta A_{P/P}$ and the Q-Structure in the Lower Mantle	117

<u>Chapter</u>	<u>Page</u>
References	122
Table Captions	127
Tables	128
Figure Captions	145
Figures	148
APPENDIX	
	189
(1) Some Vector and Dyadic Identities	190
(2) List of Symbols Used in the Text	194
(3) Computations Concerning the Seismic Rays	200

## Chapter 1

### INTRODUCTION

#### 1.1. Historical Background

Seismologists began to notice more than forty years ago that for a given earthquake, there existed a systematic distribution of P-wave polarities over the earth's surface. This led to the development of a technique now known as the method of fault-plane solution. Based on Nakano's (1923) theoretical work, the method was gradually evolved in a series of papers (Byerly, 1926, 1928, 1934, 1938), in which the first motion data were interpreted in terms of the orientation of an equivalent force system acting at the source. Further refinements of the method were made chiefly by Hodgson and his co-workers (for references, see Honda, 1962), making it applicable to practically all the observable body-wave phases. Subsequently, a large number of earthquakes have been analyzed by various investigators, and statistical studies on the resulting fault-plane solutions of earthquakes from a given tectonic region have furnished valuable insight into the broad pattern of the regional stress field. The simplicity and elegance of the fault-plane solution method, which has produced much important knowledge, is evident. Nevertheless, it must be emphasized that only the sense of the very first motion of a wave signal is utilized in the above method. From the theory of wave propagation, there is little doubt that all propagating wave signals carry information about the emitting source. A good example is the case of the radio-wave communication. The marvels of today's

radio technology strongly suggest the potentials in the seismic body waves which could deliver much more information about the exciting source in addition to the orientation of its equivalent force system. This idea is not new. In fact from time to time in the past, many seismologists have attempted to make body-wave amplitude measurements, only to find themselves hampered from obtaining meaningful measurements, let alone the source information. The failures have chiefly been attributed to the obscure responses from the various instruments. Later, in an experiment using identical instruments, Gutenberg (1957) further confirmed that the geology at different recording sites also causes an amplitude variation as large as an order of magnitude. In order to account for this ground-effect, the station constant was determined, so as to permit correlation of wave amplitudes among stations. This, again, was not very successful, mainly because the station constant, not known as the crustal transfer function, is a rapidly oscillatory function of frequency particularly for short-period waves.

## 1.2. Objectives

The main theme of the present thesis is to develop and elucidate a new approach to the problem of body-wave amplitude and earthquake source studies.

In addition to the response obscurity due to the instruments and the ground effect, there were still other factors that have hindered the progress in body-wave amplitude and source studies. Lack of information concerning the anelasticity of the earth was an

important one, particularly in the early years when long-period instruments were not available. The lack of theory to calculate the reflected and transmitted wave fields in a layered crust was another. Moreover, the interpretation of body waves beyond first motions and travel times involves lengthy computations which were rather formidable before the common use of computers.

Recent progress in several fronts has opened up new possibilities for our problem. The establishment of the World-Wide Standardized Seismograph Network marks a new era in seismological research. With the well-calibrated long-period instruments having peak response at around 25 seconds, we can now record highly reliable long-period waves around the world, a task that was not possible before. In the papers by Thomson (1950) and Haskell (1953, 1960, 1962), the mathematical problem of plane waves in plane parallel layers has largely been solved in terms of the products of the so-called Thomson-Haskell matrices. The numerical evaluation of these matrices is quite straightforward on the high-speed computer. The generalization of the Thomson-Haskell steady-state solution to one for an arbitrary waveform is a direct application of the Fourier integral theorem. Increasing knowledge of the crustal structures has recently resulted from long-range seismic refraction experiments, regional gravity surveys, and surface-wave dispersion data. With known crustal structures and the Thomson-Haskell method, a complex function can be found at least numerically which would account for what Gutenberg has attributed to as the

ground-effect. Anderson and Archambeau (1964) have obtained a measure of the anelasticity  $Q$  of the earth from data of free oscillations and propagating surface waves. A further study (Anderson et al., 1964) has made the resulting  $Q$  applicable to body waves. All these recent developments are made use of in the present approach to the problem of body-wave amplitude and earthquake source studies, as will be detailed in the following.

### 1.3 A Sketch of the Contents

The theoretical part of the present approach to body-wave and earthquake source studies will be presented in Part I (Chapters 2, 3, and 4), and three examples of its application will be presented in Part II (Chapters 5, 6, and 7).

It is intended to formulate the theory in a relatively self-contained manner, with the basic assumption of a linear elastic wave equation. The first three sections of Chapter 2 are devoted to a quite general derivation of a three-dimensional representation theorem suitable for the calculation of the P-wave and the S-wave fields for a given exciting source. These results are different from the representation theorems by de Hoop (1958) and by Knopoff (1956) in that the vector notations are used in our case and the Green's function use here is a dyadic which, for the far field in an infinite medium, is compact in form and clear in physical interpretations. In comparison, de Hoop and Knopoff employ the cartesian tensor notations and their Green's function is defined by an integral operator. Also they have separated the displacement and stress into

two explicit terms which makes their results most appropriate to mixed boundary value problems such as the problem of diffraction. On the other hand, the present results are distinct from the results by Archambeau (1964), Banaugh (1964), and Love (1944) in that these authors introduce into the vector problem a set of potential functions which reduce the vector wave equation under consideration to a scalar one. Therefore only a scalar Green's function is involved and their resulting representation theorems are written for the displacement potentials. The present formulation follows the approach outlined in Morse and Feshback (1953) but gives a more thorough derivation which ends up with two formulas particularly convenient for the calculation of seismic P- and S-wave radiations. Section 2.4 then gives a detailed calculation of various radiation fields for a dislocation source in an infinite medium. By the notion of body-force equivalents, a simple formula is derived at the end of this section which easily leads to the calculation of the total seismic energy.

Chapter 3 deals with the propagation of body waves in which ray theory is employed instead of the normal mode theory. The current seismic ray theory (e.g., Bullen, 1963; Savarensky and Kirnos, 1955; Macelwane and Schon, 1936) relies largely on the results of the classical geometrical optics, which, in turn, is based mainly on the original paper by Sommerfeld and Runge (1911). In addition to the objections to Sommerfeld and Runge's formulation discussed in Section 3.1.1, their results for a scalar wave problem is

in general inapplicable to seismological problems involving vector waves in an inhomogeneous elastic medium. Their derivations of the travel-time and distance integrals start from an intuitively proven Snell's law, and offers little insight as to the relationship among the rays, the eikonals, and the associated boundary value problem. Moreover, the standard derivation of the geometrical spreading factor (e.g., Jeffreys, 1962, p. 49; Bullen, 1963, p. 126) is not sound in several respects, and the result is generally incorrect except for some special cases. It appears therefore desirable to reformulate the seismic ray theory on a more rigorous basis. In section 3.1 and 3.2, a self-consistent ray theory is presented based on the vector wave equation in an inhomogeneous medium. The results are essentially an extension of the works by Luneberg (1944) and Karal and Keller (1959).

Within the ray approximation, attenuation of body waves is discussed in section 3.3. Wherever the ray theory is insufficient to describe the wave process, it is supplemented with a more rigorous wave theory. Accordingly, the reflection and transmission of body waves across layered boundaries are discussed in section 3.4 and the diffraction in section 3.5.

All the efforts in Chapter 2 and Chapter 3 are aimed at the preparation for the formulation of a method by which the body-wave fields can be extrapolated from one point to another. This method of body-wave equalization is presented in Chapter 4.

In Part II, three examples are given as direct applications

of the above method. Each example is by itself an independent study. In Chapter 5 and Chapter 6, two deep-focus earthquakes are studied thoroughly with regard to their source mechanism. The last chapter is devoted to the extraction of information about the Q-depth structure.

PART I  
THEORY

## Chapter 2

### ELASTODYNAMIC SOURCE THEORY AND BODY-WAVE RADIATION

#### 2.1 Governing Differential Equations

The equation of motion of an isotropic, homogeneous, elastic medium has the general form

$$\alpha^2 \nabla(\nabla \cdot \vec{f}) - \beta^2 \nabla \times \nabla \times \vec{f} - \frac{\partial^2 \vec{f}}{\partial t^2} = -4\pi \vec{q} \quad (2.1)$$

where

$$\alpha = [(\lambda + 2\mu)/\rho]^{1/2}, \quad \beta = (\mu/\rho)^{1/2}$$

are the longitudinal and transverse wave velocities respectively.

$\vec{q} = \vec{q}(\vec{r}, t)$  is the force density, or the source, which produces a vector field  $\vec{f} = \vec{f}(\vec{r}, t)$  that may be the displacement.

Let us assume that the source function can be analyzed by the Fourier integral

$$\vec{q}(\vec{r}, t) = \int_{-\infty}^{\infty} \vec{Q}(\vec{r}, \omega) e^{i\omega t} d\omega \quad (2.2)$$

which has the Fourier inversion

$$\vec{Q}(\vec{r}, \omega) = \frac{1}{2\pi} \int_{-\infty}^{\infty} \vec{q}(\vec{r}, t) e^{-i\omega t} dt \quad (2.3)$$

Similarly, we may analyze the general vector field  $\vec{f}(\vec{r}, t)$  into Fourier components,

$$\vec{f}(\vec{r}, t) = \int_{-\infty}^{\infty} \vec{F}(\vec{r}, \omega) e^{i\omega t} d\omega \quad (2.4)$$

with a corresponding inverse relation

$$\vec{F}(\vec{r}, \omega) = \frac{1}{2\pi} \int_{-\infty}^{\infty} \vec{f}(\vec{r}, t) e^{-i\omega t} dt \quad (2.5)$$

By substitution of (2.2) and (2.4) into (2.1), we see that the Fourier component obeys the differential relation

$$\alpha^2 \nabla(\nabla \cdot \vec{F}) - \beta^2 \nabla \times \nabla \times \vec{F} + \omega^2 \vec{F} = -4\pi \vec{Q} \quad (2.6)$$

which is recognized to be the vector Helmholtz equation in elastodynamics.

Any vector field may be decomposed into a longitudinal and a transverse part

$$\vec{F} = \vec{F}_\ell + \vec{F}_t \quad (2.7)$$

with

$$\vec{F}_\ell = \nabla \phi, \quad \vec{F}_t = \nabla \times \vec{A} \quad (2.8)$$

and consequently

$$\nabla \times \vec{F}_\ell = 0, \quad \nabla \cdot \vec{F}_t = 0 \quad (2.9)$$

where  $\phi$  is the scalar potential and  $\vec{A}$  the vector potential. In order that the right-hand side of (2.7) be a solution of (2.6) it is sufficient that  $\vec{F}_\ell$  and  $\vec{F}_t$  satisfy the equations

$$\nabla^2 \vec{F}_\ell + k_\alpha^2 \vec{F}_\ell = -4\pi \vec{Q}_\ell / \alpha^2 \quad (2.10)$$

$$\nabla^2 \vec{F}_t + k_\beta^2 \vec{F}_t = -4\pi \vec{Q}_t / \beta^2 \quad (2.11)$$

Here, by the same token we have written  $\vec{Q} = \vec{Q}_l + \vec{Q}_t$  as the longitudinal and transverse parts of the source density,  $k_\alpha = \omega/a$  and  $k_\beta = \omega/b$  are wave numbers.

## 2.2 Green's Dyadic for the Vector Helmholtz Equation

In general, Green's function is the kernel of an integral operator which serves to transform the boundary conditions and the source densities into the solution. When the solution is to be a scalar, this kernel is a scalar operator. But in the case of a vector boundary value problem as the one we shall be dealing with, the Green's function must be a dyadic, or a vector operator, in order to transform the vector boundary values and source densities into the vector solution. Analogous to the scalar case, the Green's dyadic obeys its own reciprocal theorem. In other words, Green's dyadic is symmetric with respect to the source and field coordinates, and satisfies the inhomogeneous dyadic equations (Morse and Feshbach, 1953).

$$\nabla^2 \mathcal{G}_l(\vec{r}, \vec{r}', k_\alpha) + k_\alpha^2 \mathcal{G}_l(\vec{r}, \vec{r}', k_\alpha) = -4\pi \mathcal{D}_l(\vec{r} - \vec{r}') \quad (2.12)$$

$$\nabla^2 \mathcal{G}_t(\vec{r}, \vec{r}', k_\beta) + k_\beta^2 \mathcal{G}_t(\vec{r}, \vec{r}', k_\beta) = -4\pi \mathcal{D}_t(\vec{r} - \vec{r}') \quad (2.13)$$

Here  $\mathcal{G}_l$  and  $\mathcal{G}_t$  are the longitudinal and the transverse part of the Green's dyadic, respectively associated with the differential equations (2.10) and (2.11). Unlike the case in electromagnetic waves,  $\mathcal{G}_l$  and  $\mathcal{G}_t$  must be obtained separately and then put together to form the complete Green's dyadic  $\mathcal{G}(\vec{r}, \vec{r}', \omega)$ ,

$$G(\vec{r}, \vec{r}', \omega) = \frac{1}{2} G_l(\vec{r}, \vec{r}', k_a) + \frac{1}{\beta} G_t(\vec{r}, \vec{r}', k_\beta) \quad (2.14)$$

which is associated with the differential equation (2.6).

In (2.12) we introduced the dyadic operator  $\mathcal{D}_l(\vec{r} - \vec{r}')$  which is defined (Morse and Feshbach, 1953) as the operator which, when applied to any vector field  $\vec{F}(\vec{r}')$ , implies an integration over  $\vec{r}'$  and yields only the longitudinal part of  $\vec{F}(\vec{r})$ . Likewise in (2.13) the operator  $\mathcal{D}_t(\vec{r} - \vec{r}')$ , when applied to  $\vec{F}(\vec{r}')$ , yields the transverse part of  $\vec{F}(\vec{r})$ .  $\mathcal{D}_l(\vec{r} - \vec{r}')$  and  $\mathcal{D}_t(\vec{r} - \vec{r}')$  are connected by the relation

$$\mathcal{J} \delta(\vec{r} - \vec{r}') = \mathcal{D}_l(\vec{r} - \vec{r}') + \mathcal{D}_t(\vec{r} - \vec{r}') \quad (2.15)$$

where  $\delta(\vec{r} - \vec{r}')$  is the Dirac delta function, and  $\mathcal{J}$  is the unity dyadic known as the idemfactor with the property that, for any vector  $\vec{A}$ ,

$$\mathcal{J} \cdot \vec{A} = \vec{A}$$

Notice that in the case of electromagnetic waves equations (2.12) and (2.13) reduce to a single equation

$$\nabla^2 G(\vec{r}, \vec{r}', k) + k^2 G(\vec{r}, \vec{r}', k) = -4\pi \mathcal{J} \delta(\vec{r} - \vec{r}') \quad (2.16)$$

and in this case, the Green's dyadic for electromagnetic wave can be obtained directly from (2.16) without being first decomposed into longitudinal and transverse parts.

It is not always possible to obtain Green's dyadics  $G_l$  and

$G_t$  in a given coordinate system. There are only six coordinate systems, the rectangular, the three cylindrical, the spherical and the conical coordinates, in which separation of the vector Helmholtz equation is possible. And only in these coordinates can one construct the Green's dyadics. The most convenient way to obtain Green's dyadics, at least formally, is by way of eigenfunction expansion.

So long as the coordinates are separable, the solution of the vector Helmholtz equation can always be expanded in terms of the three sets of mutually perpendicular eigenvectors  $\vec{L}_n$ ,  $\vec{M}_n$  and  $\vec{N}_n$  as defined by Morse and Feshbach (1953). These three sets of eigenvectors are constructed on the basis of three scalar potential functions, all being solutions of the scalar Helmholtz equation. Therefore each are naturally labeled by a trio of quantum numbers, symbolized here by the subscript  $n$ , and have the property of orthogonal functions

$$\iiint \vec{L}_n^* \cdot \vec{L}_m \, dv = \delta_{mn} \quad (2.17)$$

for all values of  $m$  and  $n$ , where the integration is over the volume enclosed by the boundary with respect to which the eigenfunctions are expanded and the superscript asterisk denotes the complex conjugate. Same relations of the type expressed in (2.17) also hold for  $\vec{M}_n$  and  $\vec{N}_n$ .

If we expand  $G_l$  and  $G_t$  by

$$Q_l = \sum_n c_n \vec{L}_n^* \vec{L}_n$$

$$Q_t = \sum_n [ c'_n \vec{M}_n^* \vec{M}_n + c''_n \vec{N}_n^* \vec{N}_n ]$$

and  $\mathcal{D}_l$  and  $\mathcal{D}_t$

$$\mathcal{D}_l = \sum_n d_n \vec{L}_n^* \vec{L}_n$$

$$\mathcal{D}_t = \sum_n [ d'_n \vec{M}_n^* \vec{M}_n + d''_n \vec{N}_n^* \vec{N}_n ]$$

where the juxtaposition of two vectors denotes a dyadic, and  $c$ 's and  $d$ 's are arbitrary constants, then through equations (2.13) and (2.14), it is not difficult to show that

$$Q_l(\vec{r}, \vec{r}', k_\alpha) = -4\pi \sum_n d_n \frac{\vec{L}_n^* \vec{L}_n}{(k_n^2 - k_\alpha^2)} \quad (2.18)$$

$$Q_t(\vec{r}, \vec{r}', k_\beta) = -4\pi \sum_n \left[ \frac{d'_n \vec{M}_n^* \vec{M}_n + d''_n \vec{N}_n^* \vec{N}_n}{(k_n^2 - k_\beta^2)} \right] \quad (2.19)$$

Here  $k_n^2$  is the set of eigenvalues. In a finite domain,  $k_n^2$  forms a discrete set. If  $Q$  is regarded as a function of  $k$ , it has poles at  $k = k_n$ , which physically corresponds to an infinite response to a driving force at a resonant frequency. However, in an infinite domain, the eigenvalues form a continuous set, and one can transform the sums in (2.18) and (2.19) into integrals so that

close-form Green's dyadics are sometimes obtainable. This will be discussed in a later section.

### 2.3. Three Dimensional Representation Theorem

In this section we shall obtain a three dimensional representation theorem for the vector Helmholtz equation (2.6). Before doing so, we first need a generalized Green's theorem which can easily be obtained from a generalized Gauss' theorem

$$\iiint_V (\nabla \cdot \mathcal{G}) dv = \iint_S \vec{n} \cdot \mathcal{G} ds \quad (2.20)$$

where  $\vec{n}$  is the outward unit vector normal to the boundary surface  $S$  enclosing a volume  $V$ .  $\mathcal{G}$  is a dyadic. The validity of (2.20) is obvious in light of the linearity of the integral operator which allows superposition.

Now, putting into (2.20)

$$\mathcal{G} = \vec{F}(\nabla \cdot \mathcal{Q})$$

where  $\mathcal{Q}$  is a dyadic and, as will be seen later, will become our Green's function, we then have

$$\iiint_V \nabla \cdot [\vec{F}(\nabla \cdot \mathcal{Q})] dv = \iint_S (\vec{n} \cdot \vec{F})(\nabla \cdot \mathcal{Q}) ds \quad (2.21)$$

Next, putting into (2.20)

$$\mathcal{G} = \vec{F} \times \nabla \times \mathcal{Q}$$

we have

$$\begin{aligned} \iiint \nabla \cdot [\vec{F} \times \nabla \times \mathcal{G}] \, dv &= \iint \vec{n} \cdot (\vec{F} \times \nabla \times \mathcal{G}) \, ds \\ &= \iint \vec{F} \cdot (\nabla \times \mathcal{G} \times \vec{n}) \, ds \end{aligned} \quad (2.22)$$

By virtue of the identities (Appendix 1)

$$\begin{aligned} \nabla \cdot [\vec{F}(\nabla \cdot \mathcal{G})] &= \vec{F} \cdot [\nabla(\nabla \cdot \mathcal{G})] + (\nabla \cdot \vec{F})(\nabla \cdot \mathcal{G}) \\ \nabla \cdot (\vec{F} \times \nabla \times \mathcal{G}) &= (\nabla \times \vec{F}) \cdot (\nabla \times \mathcal{G}) - \vec{F} \cdot (\nabla \times \nabla \times \mathcal{G}) \end{aligned}$$

(2.21) and (2.22) become

$$\begin{aligned} \iiint \{ \vec{F} \cdot \nabla(\nabla \cdot \mathcal{G}) - \mathcal{G} \cdot [\nabla(\nabla \cdot \vec{F})] \} \, dv \\ = \iint [(\nabla \cdot \mathcal{G})(\vec{F} \cdot \vec{n}) - (\nabla \cdot \vec{F})(\mathcal{G} \cdot \vec{n})] \, ds \end{aligned} \quad (2.23)$$

$$\begin{aligned} \iiint [\mathcal{G} \cdot (\nabla \times \nabla \times \vec{F}) - \vec{F} \cdot (\nabla \times \nabla \times \mathcal{G})] \, dv \\ = \iint [(\vec{n} \times \vec{F}) \cdot (\nabla \times \mathcal{G}) + (\vec{n} \times \nabla \times \vec{F}) \cdot \mathcal{G}] \, ds \end{aligned} \quad (2.24)$$

Adding (2.24) to (2.23) and noting that (Appendix 1)

$$\nabla^2 \mathcal{G} = \nabla(\nabla \cdot \mathcal{G}) - \nabla \times \nabla \times \mathcal{G}$$

$$\nabla^2 \vec{F} = \nabla(\nabla \cdot \vec{F}) - \nabla \times \nabla \times \vec{F}$$

We finally obtain the generalized Green's theorem.

$$\begin{aligned}
 & \iiint (\vec{F} \cdot \nabla^2 \vec{Q} - \vec{Q} \cdot \nabla^2 \vec{F}) \, dv = \\
 & = \iint \left\{ [(\vec{F} \cdot \vec{n})(\nabla \cdot \vec{Q}) - (\vec{Q} \cdot \vec{n})(\nabla \cdot \vec{F}) \right. \\
 & \quad \left. + (\nabla \times \vec{Q}) \cdot (\vec{n} \times \vec{F}) + \vec{Q} \cdot (\vec{n} \times \nabla \times \vec{F}) \right\} \, ds \quad (2.25)
 \end{aligned}$$

With (2.25), we now proceed to obtain the dyadic representation theorem for the vector boundary value problem. In view of (2.7) and (2.8), we can write (2.6) in the form

$$\alpha^2 \nabla^2 \vec{F}_\ell + \beta^2 \nabla^2 \vec{F}_t + \omega^2 (\vec{F}_\ell + \vec{F}_t) = -4\pi \vec{Q} \quad (2.26)$$

Adding (2.12) to (2.13), we obtain, by the definition of (2.14) and (2.15)

$$\nabla^2 \vec{Q}_\ell + \nabla^2 \vec{Q}_t + \omega^2 \vec{Q} = -4\pi \mathcal{J} \delta(\vec{r} - \vec{r}') \quad (2.27)$$

Dotting (2.27) from the left by  $\vec{F} = \vec{F}_\ell + \vec{F}_t$  and dotting (2.26) from the left by  $\vec{Q} = \vec{Q}_\ell / \alpha^2 + \vec{Q}_t / \beta^2$ , we form the difference of the two expressions and integrate the resulting vector field over the total volume, which gives

$$\begin{aligned}
 & \iiint [(\vec{F}_\ell \cdot \nabla^2 \vec{Q}_\ell - \vec{Q}_\ell \cdot \nabla^2 \vec{F}_\ell) + (\vec{F}_t \cdot \nabla^2 \vec{Q}_t - \vec{Q}_t \cdot \nabla^2 \vec{F}_t)] \, dv \\
 & + \iiint [(\vec{F}_t \cdot \nabla^2 \vec{Q}_\ell - \frac{\alpha^2}{\beta^2} \vec{Q}_t \cdot \nabla^2 \vec{F}_\ell) - (\vec{F}_\ell \cdot \nabla^2 \vec{Q}_t + \frac{\beta^2}{\alpha^2} \vec{Q}_\ell \cdot \nabla^2 \vec{F}_t)] \, dv \\
 & = -4\pi \iiint \vec{F} \cdot \mathcal{J} \delta(\vec{r} - \vec{r}') \, dv + 4\pi \iiint \vec{Q} \cdot \vec{Q} \, dv \quad (2.28)
 \end{aligned}$$

On the left-hand side of (2.28) the second volume integral has to be transformed so that Gauss' theorem can be applied. Through the dyadic identities

$$\begin{aligned}\nabla \cdot (\vec{E} \vec{F}) &= (\nabla \cdot \vec{E}) \vec{F} + \vec{E} \cdot \nabla \vec{F} \\ \nabla \cdot (\vec{E} \times \mathcal{E}) &= (\nabla \times \vec{E}) \cdot \mathcal{E} - \vec{E} \cdot (\nabla \times \mathcal{E})\end{aligned}$$

it is easy to show that

$$\left. \begin{aligned}\vec{F} \cdot \nabla^2 \mathcal{G}_l &= \nabla \cdot [\vec{F}_t (\nabla \cdot \mathcal{G}_l)] \\ \mathcal{G}_t \cdot \nabla^2 \vec{F}_l &= \nabla [\mathcal{G}_t (\nabla \cdot \vec{F}_l)] \\ \vec{F}_l \cdot \nabla^2 \mathcal{G}_t &= \nabla \cdot (\vec{F}_l \times \nabla \times \mathcal{G}_t) \\ \mathcal{G}_l \cdot \nabla^2 \vec{F}_t &= \nabla \cdot [(\nabla \times \vec{F}_t) \times \mathcal{G}_l]\end{aligned}\right\} \quad (2.29)$$

Substituting (2.29) into (2.28), we then apply Green's theorem to the first volume integral, and Gauss' theorem to the second volume integral. With some straightforward algebra and by interchanging  $\vec{r}$  and  $\vec{r}'$  we finally can represent the vector field  $\vec{F}(\vec{r})$  inside and on the boundary surface in terms of the body force and the boundary values

$$\begin{aligned}\vec{F}_l(\vec{r}) &= \frac{1}{\alpha^2} \iiint \mathcal{G}_l \cdot \vec{Q} \, dv' \\ &+ \frac{1}{4\pi} \iint [(\mathcal{G}_l \cdot \vec{n})(\nabla' \cdot \vec{F}) - \alpha^2 (\vec{F} \cdot \vec{n})(\nabla' \cdot \mathcal{G}) \\ &\quad - \frac{\beta^2}{\alpha^2} \mathcal{G}_l \cdot (\mathbf{n} \times \nabla' \times \vec{F})] \, ds'\end{aligned} \quad (2.30)$$

$$\begin{aligned}
 \vec{F}_t(\vec{r}) = & \frac{1}{\beta^2} \iiint Q_t \cdot \vec{Q} \, dv' \\
 & - \frac{1}{4\pi} \iint [Q_t \cdot (\vec{n} \times \nabla' \times \vec{F}) + \beta^2 (\nabla' \times Q) \cdot (\vec{n} \times \vec{F}) \\
 & \quad - \frac{a^2}{\beta^2} (Q_t \cdot \vec{n})(\nabla' \cdot \vec{F})] \, ds' \qquad (2.31)
 \end{aligned}$$

and, of course

$$\vec{F}(\vec{r}) = \vec{F}_l(\vec{r}) + \vec{F}_t(\vec{r})$$

where integrations are to be taken with respect to the  $\vec{r}'$  coordinates. Notice that the last term of the surface integral in both (2.30) and (2.31) is not present in the case of electromagnetic waves.

#### 2.4. Radiation of Elastic Waves in an Infinite Medium

In this section we shall use the representation theorems obtained in the previous section to calculate the radiation field. It is sufficient for our purpose to assume that the excitation source is embedded in an infinite, homogeneous, elastic medium and has a source dimension which is small as compared with its distance to the nearest observation point. We also assume for the moment that the source displacement vector is either tangential or normal to a plane surface. The former corresponds to a shear fault, the latter, a tensile fault. A radiation field corresponding to a more general type of source motion can, of course, be obtained by way of superposition. Moreover, by the notion of equivalent source

theory we shall further obtain a virtue moment of a volume source which leads in a simple way to an expression enabling the estimation of total seismic energy.

#### 2.4.1. Greens Dyadics in an Infinite Medium

As indicated before, Green's dyadics,  $G_{\alpha}$  and  $G_{\beta}$  can, for an infinite domain, be obtained from (2.18) and (2.19) by transforming the sums into integrals, and by choosing appropriate integration path so as to obtain correct forms for outgoing waves. A more elegant way would probably be to construct them from Green's function  $g$  for scalar Helmholtz equation.

To find the Green's function  $g$ , we start from the differential equation

$$\nabla^2 g(\vec{r}, \vec{r}', \omega) + k^2 g(\vec{r}, \vec{r}', \omega) = -4\pi\delta(\vec{r} - \vec{r}')$$

and note that, in view of the absence of any preferred direction in space,  $g(\vec{r}, \vec{r}', \omega)$  must not be a function of  $\theta$  and  $\phi$ . Equation (2.32) therefore reduces to

$$\frac{d^2}{dR^2} (gR) + k^2 (gR) = -4\pi\delta(\vec{R}) \quad (2.33)$$

in a spherical coordinate system centered at  $\vec{r} = \vec{r}'$ . The general solution of (2.33), taken into account Sommerfeld's radiation condition, is

$$g_{\alpha, \beta} = A \frac{e^{ik_{\alpha, \beta} R}}{R}$$

Putting this back into (2.32), the unknown coefficient is found to be 1, and we therefore obtain

$$g_{\alpha, \beta} = \frac{e^{ik_{\alpha, \beta} |\vec{r} - \vec{r}'|}}{|\vec{r} - \vec{r}'|} \quad (2.34)$$

Since  $G_{\alpha}$  must have a zero curl, and  $G_{\beta}$  a zero divergence, one would expect  $G_{\alpha}$  to be the gradient of some scalar functions of  $\vec{r}$  and  $\vec{r}'$  and  $G_{\beta}$  to be connected to the curl of some vector functions of  $\vec{r}$  and  $\vec{r}'$ . The symmetry of Green's dyadics  $G_{\alpha, \beta}$  between  $\vec{r}$  and  $\vec{r}'$  further requires that if it is a gradient or curl in the  $\vec{r}$  coordinates, it must also be the gradient or curl in the  $\vec{r}'$  coordinates. Indeed, an operation of the double gradient  $\nabla \nabla'$  transforms a scalar into a dyadic. The simplest way to construct a dyadic through an operation of curl is to take the curl of a dyadic. With these remarks, and after dimensionality and singularity at the source are taken care of, one finds the longitudinal and the transverse Green's dyadics to be of the forms which indeed satisfy (2.12) and (2.13)

$$G_{\alpha}(\vec{r}, \vec{r}', k_{\alpha}) = \frac{1}{k_{\alpha}^2} [\nabla g_{\alpha}(\vec{r}, \vec{r}', k_{\alpha}) \nabla' - 4\pi \delta_{\ell}(\vec{r} - \vec{r}')] \quad (2.35)$$

$$G_{\beta}(\vec{r}, \vec{r}', k_{\beta}) = \frac{1}{k_{\beta}^2} [-\nabla \times g_{\beta}(\vec{r}, \vec{r}', k_{\beta}) \times \nabla' - 4\pi \delta_t(\vec{r} - \vec{r}')] \quad (2.36)$$

In view of (2.34), close forms of  $G_{\alpha}$  and  $G_{\beta}$ , valid everywhere except at the source point, are

$$\begin{aligned}
 G_{\alpha} = & \left[ \vec{e}_r \vec{e}_r \left( 1 - \frac{2}{k_{\alpha}^2 |\vec{r} - \vec{r}'|^2} \right) \right. \\
 & \left. - (\vec{e}_{\theta} \vec{e}_{\theta} + \vec{e}_{\phi} \vec{e}_{\phi}) \left( \frac{i}{k_{\alpha} |\vec{r} - \vec{r}'|} - \frac{1}{k_{\alpha}^2 |\vec{r} - \vec{r}'|^2} \right) \right] \frac{e^{-ik_{\alpha} |\vec{r} - \vec{r}'|}}{|\vec{r} - \vec{r}'|}
 \end{aligned} \tag{2.37}$$

$$\begin{aligned}
 G_{\beta} = & \left[ (\vec{e}_{\theta} \vec{e}_{\theta} + \vec{e}_{\phi} \vec{e}_{\phi}) \left( 1 + \frac{i}{k_{\beta} |\vec{r} - \vec{r}'|} - \frac{1}{k_{\beta}^2 |\vec{r} - \vec{r}'|^2} \right) \right. \\
 & \left. - \vec{e}_r \vec{e}_r \left( \frac{2}{k_{\beta}^2 |\vec{r} - \vec{r}'|^2} \right) \right] \frac{e^{ik_{\beta} |\vec{r} - \vec{r}'|}}{|\vec{r} - \vec{r}'|}
 \end{aligned} \tag{2.38}$$

For the far field where the distance to the observation point is large as compared to the wavelength in concern, the Green's dyadic takes up a particularly simple form

$$\begin{aligned}
 G(\vec{r}, \vec{r}', \omega) &= \frac{1}{\alpha^2} G_{\alpha} + \frac{1}{\beta^2} G_{\beta} \\
 &= \frac{1}{\alpha^2} \frac{e^{-ik_{\alpha} |\vec{r} - \vec{r}'|}}{|\vec{r} - \vec{r}'|} (\vec{e}_r \vec{e}_r) + \frac{1}{\beta^2} \frac{e^{-ik_{\beta} |\vec{r} - \vec{r}'|}}{|\vec{r} - \vec{r}'|} (\vec{e}_{\theta} \vec{e}_{\theta} + \vec{e}_{\phi} \vec{e}_{\phi})
 \end{aligned} \tag{2.39}$$

$$k_{\alpha, \beta} |\vec{r} - \vec{r}'| \gg 1$$

### 2.4.2. Radiation of Body Waves

With the foregoing preparations, we shall in this section calculate the radiation field of body waves for various source models. It is sufficient for our purpose to obtain for a point source model the far field contributions, as we shall be concerned with the body wave spectral data which have periods of between a few seconds to 100 seconds, and are recorded farther than  $20^\circ$  of distance away from the source region.

We start by considering an infinite, homogeneous elastic medium  $V$  in which there is no body force acting. Across a surface  $S$  inside  $V$  there occurs a displacement dislocation  $\vec{U}_0$  which excites a wave field in this otherwise quiet medium. We can simulate both a shear fault by requiring  $\vec{U}_0$  to be tangential to  $S$  and a normal fault by requiring  $\vec{U}_0$  to be perpendicular to  $S$ . At the source region, we set up two coordinate systems: a spherical system  $(r, \theta, \phi)$  with a right-hand base vector  $(\vec{e}_r, \vec{e}_\theta, \vec{e}_\phi)$ , and a Cartesian system  $(x_1, x_2, x_3)$  with a right-hand base vector  $(\vec{e}_1, \vec{e}_2, \vec{e}_3)$  as are shown in Figure 2.1. Note that the surface  $S$  in Figure 2.1, being the plane of motion, encloses a region exterior to  $V$ . In our case this enclosed region is sandwiched between the two sides of the plane of motion and is of little importance except in the definition of the outward normal vector  $\vec{n}$ . In the following discussion we shall choose to define that the positive direction of  $\vec{n}$  always points to this exterior region or toward the plane of motion.

2.4.2.a. Shear Fault. A shear fault is characterized by the displacement dislocation which is tangential to the fault plane. Assume that  $\vec{U}_0$  is the displacement dislocation vector on S and is a build-up step time function of strength  $L_0$  and a spatial delta function directing along a unit vector  $\vec{a}$  (cf. Figure 2.1)

$$\vec{U}_0 = \vec{U}_+ - \vec{U}_- = L_0 \left\{ \frac{e^{i\omega t}}{i\omega(1+i\omega\tau)} \right\} \delta(|\vec{r}'|) \vec{a} \quad (2.40)$$

where  $\tau$  is a parameter governing the rapidity of the build-up step.

Putting (2.40) into (2.30) and (2.31), and noting that

$$\begin{aligned} \vec{Q} &= 0 \\ \vec{U}'_0 \cdot \vec{n} &= 0 \\ \nabla \cdot \mathcal{G} &= \frac{1}{\alpha^2} \nabla \cdot \mathcal{G}_\alpha \\ \nabla \times \mathcal{G} &= \frac{1}{\beta^2} \nabla \times \mathcal{G}_\beta \end{aligned}$$

we have

$$\vec{U}_P(\vec{r}) = \frac{1}{4\pi} \iint [(\mathcal{G}_\alpha \cdot \vec{n})(\nabla' \cdot \vec{U}'_0) - \frac{\beta^2}{\alpha^2} \mathcal{G}_\alpha \cdot (\vec{n} \times \nabla' \times \vec{U}'_0)] ds' \quad (2.41)$$

$$\begin{aligned} \vec{U}_S(\vec{r}) = & - \frac{1}{4\pi} \iint [\mathcal{G}_\beta \cdot (\vec{n} \times \nabla' \times \vec{U}'_0) + (\nabla' \times \mathcal{G}_\beta) \cdot (\vec{n} \times \vec{U}'_0) \\ & - \frac{\alpha^2}{\beta^2} (\mathcal{G}_\beta \cdot \vec{n})(\nabla' \cdot \vec{U}'_0)] ds' \end{aligned} \quad (2.42)$$

where  $\vec{U}_P$  stands for P-wave motion, propagating at the velocity  $\alpha$ , and  $\vec{U}_S$  stands for S-wave motion, propagating at the velocity  $\beta$ .

Following the law of vector and dyadic analysis, we calculate the integrands of (2.41) and (2.42) and retain only the far field contributions.

$$\zeta_\alpha \cdot \vec{n} = g_\alpha (\vec{e}_r \cdot \vec{n}) \vec{e}_r \quad (2.43)$$

$$\zeta_\beta \cdot \vec{n} = g_\beta [(\vec{e}_\theta \cdot \vec{n}) \vec{e}_\theta + (\vec{e}_\phi \cdot \vec{n}) \vec{e}_\phi] \quad (2.44)$$

$$\nabla' \times \zeta_\beta = ik_\beta g_\beta (\vec{e}_\theta \vec{e}_\phi - \vec{e}_\phi \vec{e}_\theta) \quad (2.45)$$

$$\nabla' \cdot \vec{U}_0 = L_0 \left\{ \frac{e^{i\omega t}}{i\omega(1+i\omega\tau)} \right\} \delta'(|\vec{r}'|) (\vec{a} \cdot \vec{e}_r) \quad (2.46)$$

$$\vec{n} \times \nabla' \times \vec{U}_0 = -L_0 \left\{ \frac{e^{i\omega t}}{i\omega(1+i\omega\tau)} \right\} \delta'(|\vec{r}'|) (\vec{n} \cdot \vec{e}_r) \vec{a} \quad (2.47)$$

In obtaining (2.46), the differential property of the delta function,

$$\delta^{(m)}(x) = (-1)^m m! \frac{\delta(x)}{x^m} \quad (2.48)$$

is used. By substitution of (2.43) to (2.47) into (2.41) and (2.42) and by virtue of the integral property of the delta function

$$\int_{-\infty}^{\infty} f(x) \delta^{(m)}(x - x_0) dx = (-1)^m f^{(m)}(x_0) \quad (2.49)$$

we finally obtain the displacement field for a shear fault with a build-up step-function time dependence.

$$\vec{U}_P = - \frac{L_o ds}{4\pi} \frac{1}{a} \left( \frac{\beta^2}{a^2} + 1 \right) \frac{e^{i\omega \left( t - \frac{|\vec{r}|}{a} \right)}}{|\vec{r}| (1 + \omega^2 \tau^2)^{\frac{1}{2}}} (\vec{a} \cdot \vec{e}_r) (\vec{e}_r \cdot \vec{n}) \vec{e}_r \quad (2.50)$$

$$\begin{aligned} \vec{U}_{SV} = - \frac{L_o ds}{4\pi} \frac{1}{\beta} \frac{e^{i\omega \left( t - \frac{|\vec{r}|}{\beta} \right)}}{|\vec{r}| (1 + \omega^2 \tau^2)^{\frac{1}{2}}} & \left[ 2(\vec{a} \cdot \vec{e}_\theta) (\vec{n} \cdot \vec{e}_r) \right. \\ & \left. + \left( \frac{a^2}{\beta^2} - 1 \right) (\vec{a} \cdot \vec{e}_r) (\vec{n} \cdot \vec{e}_\theta) \right] \vec{e}_\theta \quad (2.51) \end{aligned}$$

$$\begin{aligned} \vec{U}_{SH} = - \frac{L_o ds}{4\pi} \frac{1}{\beta} \frac{e^{i\omega \left( t - \frac{|\vec{r}|}{\beta} \right)}}{|\vec{r}| (1 + \omega^2 \tau^2)^{\frac{1}{2}}} & \left[ 2(\vec{a} \cdot \vec{e}_\phi) (\vec{n} \cdot \vec{e}_r) \right. \\ & \left. + \left( \frac{a^2}{\beta^2} - 1 \right) (\vec{a} \cdot \vec{e}_r) (\vec{n} \cdot \vec{e}_\phi) \right] \vec{e}_\phi \quad (2.52) \end{aligned}$$

Here the transverse displacement has been written into a vertically polarized motion  $\vec{U}_{SV}$  and a horizontally polarized motion  $\vec{U}_{SH}$ . They take up positive signs if the motions are in the same direction as  $\vec{e}_\theta$  and  $\vec{e}_\phi$ , respectively, and negative signs when otherwise.

2.4.2.b. Tensile Fault. On replacing the vector  $\vec{a}$  in (2.40) by  $\vec{n}$ , thus

$$\vec{U}_o = L_o \left\{ \frac{e^{i\omega t}}{i\omega(1 + i\omega\tau)} \right\} \delta(|\vec{r}'|) \vec{n} \quad (2.53)$$

we construct a pure compressional source giving rise to a tensile fault. Assuming again that the medium is free from body force and

noting now that

$$\vec{n} \times \vec{U}_0 = 0$$

we then have from (2.30), (2.31), and (2.53)

$$\begin{aligned} \vec{U}_P(\vec{r}) = \frac{1}{4\pi} \iint [ (\zeta_a \cdot \vec{n})(\nabla' \cdot \vec{U}_0) - (\vec{U}_0 \cdot \vec{n})(\nabla' \cdot \zeta_a) \\ - \frac{\beta^2}{a^2} \zeta_a \cdot (\vec{n} \times \nabla' \times \vec{U}_0) ] ds' \end{aligned} \quad (2.54)$$

$$\vec{U}_S(\vec{r}) = - \frac{1}{4\pi} \iint [ \zeta_\beta \cdot (\vec{n} \times \nabla' \times \vec{U}_0) - \frac{a^2}{\beta^2} (\zeta_\beta \cdot \vec{n})(\nabla' \cdot \vec{U}_0) ] ds' \quad (2.55)$$

Next we evaluate the following quantities

$$\nabla' \cdot \vec{U}_0 = L_0 \left\{ \frac{e^{i\omega t}}{i\omega(1+i\omega\tau)} \right\} \delta'(|\vec{r}'|) (\vec{n} \cdot \vec{e}_r) \quad (2.56)$$

$$\vec{n} \times \nabla' \times \vec{U}_0 = L_0 \left\{ \frac{e^{i\omega t}}{i\omega(1+i\omega\tau)} \right\} \delta'(|\vec{r}'|) [ \vec{e}_r - (\vec{n} \cdot \vec{e}_r) \vec{n} ] \quad (2.57)$$

$$\nabla' \cdot \zeta_a = ik_a g_a \vec{e}_r \quad (2.58)$$

Putting (2.56), (2.57), and (2.58) into (2.54) and (2.55), and again using the relation (2.49), we obtain the far displacement fields for a tensile fault with the same time function

$$\vec{U}_P(\vec{r}) = \mp \frac{L_o ds}{4\pi} \frac{1}{a} \frac{e^{i\omega\left(t - \frac{|\vec{r}|}{a}\right)}}{|\vec{r}|(1+\omega^2\tau^2)^{\frac{1}{2}}} \left[ \left(1 - \frac{\beta^2}{a^2}\right) + \left(1 + \frac{\beta^2}{a^2}\right) (\vec{n} \cdot \vec{e}_r)^2 \right] \vec{e}_r \quad (2.59)$$

$$\vec{U}_{SV}(\vec{r}) = \mp \frac{L_o ds}{4\pi} \frac{1}{\beta} \frac{e^{i\omega\left(t - \frac{|\vec{r}|}{\beta}\right)}}{|\vec{r}|(1+\omega^2\tau^2)^{\frac{1}{2}}} \left(1 + \frac{a^2}{\beta^2}\right) (\vec{e}_\theta \cdot \vec{n})(\vec{n} \cdot \vec{e}_r) \vec{e}_\theta \quad (2.60)$$

$$\vec{U}_{SH}(\vec{r}) = \mp \frac{L_o ds}{4\pi} \frac{1}{\beta} \frac{e^{i\omega\left(t - \frac{|\vec{r}|}{\beta}\right)}}{|\vec{r}|(1+\omega^2\tau^2)^{\frac{1}{2}}} \left(1 + \frac{a^2}{\beta^2}\right) (\vec{e}_\phi \cdot \vec{n})(\vec{n} \cdot \vec{e}_r) \vec{e}_\phi \quad (2.61)$$

where the upper signs are for  $\vec{U}_O$  having the same direction of  $\vec{n}$  which corresponds to a volume collapse; the lower signs are for  $\vec{U}_O$  having the opposite direction of  $\vec{n}$  which therefore corresponds to a volume expansion.

#### 2.4.2.c. Explicit Expressions for the Radiation Patterns.

For practical purposes, it is necessary to establish the spatial relationship between the source and the receiving stations. Within the limit of a point source model, the two previously defined coordinate systems occupy a common origin. We have oriented the Cartesian system such that the  $x_1$ -axis coincides with the strike direction, and the  $x_3$ -axis points vertically upward. The transformation relations of the base vectors

$$\left. \begin{aligned}
 \vec{e}_r &= \sin \theta \cos \phi \vec{e}_1 + \sin \theta \sin \phi \vec{e}_2 + \cos \theta \vec{e}_3 \\
 \vec{e}_\theta &= \cos \theta \cos \phi \vec{e}_1 + \cos \theta \sin \phi \vec{e}_2 - \sin \theta \vec{e}_3 \\
 \vec{e}_\phi &= -\sin \theta \vec{e}_1 + \cos \phi \vec{e}_2
 \end{aligned} \right\} \quad (2.62)$$

define the connection to the spherical system in which a receiving station is represented by a pair of its coordinates  $(\theta, \phi)$ . As is easily seen from Figure 2.1,  $\theta$  will be the take-off angle of a specific ray and  $\phi$  the azimuthal angle counting from the strike direction. We then express the two constant unit vectors  $\vec{n}$  and  $\vec{a}$  in terms of the Cartesian base

$$\left. \begin{aligned}
 \vec{a} &= \cos \lambda \vec{e}_1 + \sin \lambda \cos \delta \vec{e}_2 + \sin \lambda \sin \delta \vec{e}_3 \\
 \vec{n} &= \sin \delta \vec{e}_2 - \cos \delta \vec{e}_3
 \end{aligned} \right\} \quad (2.63)$$

As defined in Figure 2.1,  $\delta$  is the dip angle and  $\lambda$ , the slip angle. Note that  $\vec{n}$  conforms with the definition of an outward normal. The explicit expressions for the radiation patterns from a fault of arbitrary dip and slip are obtained in a straightforward fashion by the combined use of equations (2.50) to (2.52), (2.59) to (2.61), (2.62) and (2.63). The radiation pattern itself will be a normalized surface in a three-dimensional space and can be regarded as a function of  $\theta$  and  $\phi$ , i.e.,  $A_s(\theta, \phi)$ . When  $\theta$  is constant,  $A_s(\theta_0, \phi)$  defines a horizontal radiation pattern which predicts amplitudes of the body waves from observation points of equal epicentral distances, or of equal take-off angles  $\theta_0$ . On the other hand, when  $\phi$  is constant,

$A_s(\theta, \phi_0)$  defines a vertical radiation pattern which predicts the amplitudes along a fixed azimuthal direction. Both patterns are found to be useful and they are summarized in Tables 2.1 and 2.2, in which we have defined the following parameters

$$b \equiv \frac{1}{2} \left( \frac{a^2}{\beta^2} - 1 \right) = \frac{1}{2(1 - 2\sigma)}$$

$$S_o \equiv \left( 1 - \frac{\beta^2}{a^2} \right) / \left( 1 + \frac{\beta^2}{a^2} \right) = \frac{1}{3 - 4\sigma}$$

$\sigma$  being the Poisson's ratio. Notice that for a Poisson's solid, where  $b = 1$  and  $S_o = \frac{1}{2}$ , our results become identical to those obtained in an earlier paper (Ben-Menahem, Smith, and Teng, 1965), which also conform with the results obtained by Knopoff and Gilbert (1960) for a slip dislocation with a continuous normal stress field.

#### 2.4.3. Body Force Equivalents

It has been pointed out by Vvedenskaya (1956) that the displacement field due to a displacement dislocation can be identically reproduced in the absence of dislocation surface by a certain properly chosen combination of body forces. Mathematically it means that in (2.30) and (2.31) the vector fields  $\vec{F}_l$  and  $\vec{F}_t$  inside a domain  $V$  generated by a distribution of  $\vec{F}$  over  $S$  in the absence of  $\vec{Q}$  can be reproduced by a proper choice of distribution of  $\vec{Q}$  in  $V$  in the absence of  $S$ . Studies along this line have been advanced by Knopoff and Gilbert (1960) and by Maruyama (1963, 1964). Using the property

of the delta function, Burridge and Knopoff (1964) were able to obtain an explicit expression to calculate the equivalent body forces with a given dislocation. On the assumption of continuity of normal stress across the dislocation sheet, Burridge and Knopoff have shown that a displacement dislocation tangential to the dislocation sheet is equivalent to a double couple body force with zero net moment, and the one normal to the dislocation sheet is equivalent to a double force with zero moment plus a pure dilatation. Similar results had been obtained in an earlier paper (Knopoff and Gilbert, 1960).

In this section we shall approach the problem in a different way. We begin with assuming that in an infinite domain  $V$  free from dislocation surface, there exists a force density  $\vec{Q}$  of an undetermined strength  $f_0$  in the following form

$$\vec{Q} = f_0 \left\{ \frac{e^{i\omega t}}{i\omega(1 + i\omega\tau)} \right\} \delta(|\vec{r}|) \vec{a} \quad (2.64)$$

We then compute the far displacement field due to a couple force constructed from  $\vec{Q}$  and then ask the question: what value can one assign to  $f_0$  so that an identical radiation field as described by (2.50) to (2.52) can be reproduced? It will be shown that the answer to this question enables us to define the moment of a seismic source which will lead easily to the calculation of the total seismic energy.

Using (2.30) and (2.31), we can write the displacement fields due to  $\vec{Q}$  in (2.64) in an infinite domain free from dislocation surface as

$$\begin{aligned}\vec{U}_P^s(\vec{r}) &= \frac{1}{\rho} \iiint \left[ \frac{1}{a^2} \frac{e^{-ik_a |\vec{r}-\vec{r}'|}}{|\vec{r}-\vec{r}'|} \vec{e}_r \vec{e}_r \right] \cdot \left[ f_o \left\{ \frac{e^{i\omega t}}{i\omega(1+i\omega\tau)} \right\} \delta(|\vec{r}'|) \vec{a} \right] dv' \\ &= \frac{F_o}{\rho a^2} \left\{ \frac{e^{i\omega t}}{i\omega(1+i\omega\tau)} \right\} \frac{e^{-ik_a |\vec{r}|}}{|\vec{r}|} (\vec{a} \cdot \vec{e}_r) \vec{e}_r\end{aligned}\quad (2.65)$$

Similarly, we have

$$\vec{U}_{SV}^s(\vec{r}) = \frac{F_o}{\rho \beta^2} \left\{ \frac{e^{i\omega t}}{i\omega(1+i\omega\tau)} \right\} \frac{e^{-ik_\beta |\vec{r}|}}{|\vec{r}|} (\vec{a} \cdot \vec{e}_\theta) \vec{e}_\theta \quad (2.66)$$

$$\vec{U}_{SH}^s(\vec{r}) = \frac{F_o}{\rho \beta^2} \left\{ \frac{e^{i\omega t}}{i\omega(1+i\omega\tau)} \right\} \frac{e^{-ik_\beta |\vec{r}|}}{|\vec{r}|} (\vec{a} \cdot \vec{e}_\phi) \vec{e}_\phi \quad (2.67)$$

where the superscript  $s$  denotes single force, and  $F_o = f_o dv$  is the total force inside  $V$ . The displacement field due to a couple force  $\vec{U}^c$  is obtained by the application of a differential operator to  $\vec{U}^s$  such that

$$\vec{U}^c = -d(\vec{n} \cdot \nabla) \vec{U}^s \quad (2.68)$$

where  $d$  is the spacing of the two opposite single forces. In the curvilinear coordinate system  $(\xi_1, \xi_2, \xi_3)$ , an operation of the above type can be expressed by writing out the  $\xi_1$  component of the result

$$\begin{aligned}[d(\vec{n} \cdot \nabla) \vec{U}^s]_1 &= \frac{d_1}{h_1} \frac{\partial U_1^s}{\partial \xi_1} + \frac{d_2}{h_2} \frac{\partial U_1^s}{\partial \xi_2} + \frac{d_3}{h_3} \frac{\partial U_1^s}{\partial \xi_3} \\ &+ \frac{U_2^s}{h_1 h_2} \left[ d_1 \frac{\partial h_1}{\partial \xi_1} - d_2 \frac{\partial h_2}{\partial \xi_1} \right] + \frac{U_3^s}{h_1 h_3} \left[ d_1 \frac{\partial h_1}{\partial \xi_3} - d_3 \frac{\partial h_3}{\partial \xi_1} \right]\end{aligned}\quad (2.69)$$

where  $d_i = d(\vec{n} \cdot \vec{e}_i)$ ; and  $h_i$ 's are the metrical coefficients.

Clearly, the other components of the type of (2.69) can be obtained by cyclic permutations of the subscripts. By performing the indicated operations, we find the far field displacements due to a couple force

$$\vec{U}_P^c(\vec{r}) = \frac{F_o d}{\rho a^3} \frac{e^{i\omega(t - \frac{|\vec{r}|}{a})}}{|\vec{r}|(1 + \omega^2 \tau^2)^{\frac{1}{2}}} (\vec{a} \cdot \vec{e}_r)(\vec{e}_r \cdot \vec{n}) \vec{e}_r \quad (2.70)$$

$$\vec{U}_{SV}^c(\vec{r}) = \frac{F_o d}{\rho \beta^3} \frac{e^{i\omega(t - \frac{|\vec{r}|}{\beta})}}{|\vec{r}|(1 + \omega^2 \tau^2)^{\frac{1}{2}}} (\vec{a} \cdot \vec{e}_\theta)(\vec{e}_r \cdot \vec{n}) \vec{e}_\theta \quad (2.71)$$

$$\vec{U}_{SH}^c(\vec{r}) = \frac{F_o d}{\rho \beta^3} \frac{e^{i\omega(t - \frac{|\vec{r}|}{\beta})}}{|\vec{r}|(1 + \omega^2 \tau^2)^{\frac{1}{2}}} (\vec{a} \cdot \vec{e}_\phi)(\vec{e}_r \cdot \vec{n}) \vec{e}_\phi \quad (2.72)$$

These fields cannot be made equal to those given in (2.50) to (2.52)<sup>\*</sup>, whatever choice of  $f_o$  is to be made. Study of (2.70) to (2.72) reveals that the only possibility is to add the contributions from another couple force obtained from the field due to the single force

$$\vec{Q}^* = C f_o \left\{ \frac{e^{i\omega t}}{i\omega(1 + i\omega\tau)} \right\} \delta(|\vec{r}|) \vec{n} \quad (2.73)$$

by applying again the operator  $-d(\vec{a} \cdot \nabla)$ , where  $C$  is a constant to be determined. Because of the symmetry existing in  $\vec{a}$  and  $\vec{n}$  between the two couple forces, the radiation patterns of the second couple can be obtained simply by interchanging the two vectors  $\vec{a}$  and  $\vec{n}$  in (2.70) to (2.72). When this is done, we add up both

contributions which give

$$\vec{U}_P(\vec{r}) = \frac{F_o d}{\rho a^3} \frac{e^{i\omega\left(t - \frac{|\vec{r}|}{a}\right)}}{|\vec{r}|(1+\omega^2\tau^2)^{\frac{1}{2}}} (1+C)(\vec{a} \cdot \vec{e}_r)(\vec{e}_r \cdot \vec{n})\vec{e}_r \quad (2.74)$$

$$\vec{U}_{SV}(\vec{r}) = \frac{F_o d}{2\rho\beta^3} \frac{e^{i\omega\left(t - \frac{|\vec{r}|}{\beta}\right)}}{|\vec{r}|(1+\omega^2\tau^2)^{\frac{1}{2}}} \left[ 2(\vec{a} \cdot \vec{e}_\theta)(\vec{n} \cdot \vec{e}_r) + 2C(\vec{a} \cdot \vec{e}_r)(\vec{n} \cdot \vec{e}_\theta) \right] \vec{e}_\theta \quad (2.75)$$

$$\vec{U}_{SH}(\vec{r}) = \frac{F_o d}{2\rho\beta^3} \frac{e^{i\omega\left(t - \frac{|\vec{r}|}{\beta}\right)}}{|\vec{r}|(1+\omega^2\tau^2)^{\frac{1}{2}}} \left[ 2(\vec{a} \cdot \vec{e}_\phi)(\vec{n} \cdot \vec{e}_r) + 2C(\vec{a} \cdot \vec{e}_r)(\vec{n} \cdot \vec{e}_\phi) \right] \vec{e}_\phi \quad (2.76)$$

In order to equalize the fields in (2.74) to (2.76) to those in (2.50) to (2.52), it is sufficient to require that

$$2C = \frac{a^2}{\beta^2} - 1 \quad (2.77)$$

and

$$F_o d = \frac{L_o ds}{2\pi} \mu \quad (2.78)$$

Comparing (2.64) and (2.73) in view of (2.77) and (2.78), we conclude that, to reproduce the field generated by the dislocation defined in (2.40), it will be sufficient to superpose the fields produced by two perpendicular force couples with opposite but not necessarily equal moments. One couple has the moment  $(L_o ds/2\pi)\mu$ , the other  $-(L_o ds/4\pi)(\lambda + \mu)$ ; the two moments cancel out each other only if the Poisson's relation holds. In general, the net moment is

$$\frac{L_o ds}{4\pi} (\lambda - \mu) = \frac{L_o ds}{2\pi} \mu \frac{4\sigma - 1}{2(1 - 2\sigma)} \quad (2.79)$$

the quantity inside the brackets approaches zero in the earth's crust where  $\sigma$  is around 0.25, and becomes  $1/4$  in a depth of about 600 km where  $\sigma$  is about 0.3. Therefore our model predicts a net moment which can be as large as a quarter of the dipole moment. Many authors, e.g., Steketee (1958) and Keilis-Borok (1957), have pointed out that the direct P- and S-waves give information which concerns with a non-equilibrium state, for the occurrence of an earthquake is essentially a break-down of static equilibrium. So far as the radiation of P- and S-waves is concerned, there is no a priori reason that it has to satisfy the condition of equilibrium at every instant during the rupture process. However, as soon as the rupture process has ceased, and the P- and the S-wavefronts have left the source region, equilibrium in the source neighborhood must be restored. Further, from the consideration of conservation of angular momentum, there should be no net moment after the rupture process if there is no external force acting on the source region. Therefore it is only plausible that a source model appropriate to the initial motions does not have to be in equilibrium, but a complete source model explaining the entire seismic signals ought to be a statically balanced one. Recalling that we started in section (2.4.2) with the source displacement (2.40) and ended up with the S-wave radiation patterns (2.51) and (2.52) which, as checked by the results

(2.75) and (2.76) calculated from a double-couple source model, are found to represent an unbalanced source. Therefore, it is concluded that in order to construct a balanced source model, the displacement (2.40) has to be modified to a dislocation of Volterra type or one of Somigliana type (Steketee, 1958) so as to insure vanishing moment. These results have been obtained by various authors (e.g., Knopoff and Gilbert, 1960), which we shall not repeat here. However, we have obtained the equivalent results from the body-force approach (if setting  $C = 1$  in (2.74), (2.75) and (2.76), or  $b = 1$  in Tables 2.1 and 2.2) which, of course, is appropriate for a double-couple force of vanishing moment. These results will be used in chapters 5 and 6.

#### 2.4.4 Energy Calculation

In the previous section we have arrived at an expression of the moment for an equivalent force couple in terms of source displacement  $L_0$  and area  $ds$  of a dislocation sheet. By the theory of body-wave amplitude equalization which we shall formulate in the following section, the quantity  $L_0 ds$  can be estimated from body-wave amplitude spectrums observed on the surface of the earth. This points to a way in which seismic energy can be calculated in terms of deformation work done upon the occurrence of the dislocation.

Considering a fictitious force of magnitude  $F_0$  acting at the source and causing a net displacement  $L_0$  we define the energy emitted by a seismic source to be equal to the work done by  $F_0$ :

$$\text{Energy} = \int_0^{L_0} F_0 \, dl \quad (2.80)$$

Assuming that  $F_0$  remains constant over the process of displacement, we then have for a double-couple force

$$\text{Energy} = \frac{\lambda + 3\mu}{4\pi} [L_0 \, ds] \frac{L_0}{d} \quad (2.81)$$

Notice that this is not the partial energy carried by the P- or S-wave alone. It is the total energy of the seismic source, provided that the presence of a free surface does not significantly change the partition of energy among P, S, and other wave types. The quantity inside the brackets of (2.81) is directly measurable from the body-wave amplitude observed on the surface of the earth. The quantity  $L_0/d$  is equivalent to a shear strain.

### Chapter 3

#### PROPAGATION OF BODY WAVES

The formal solution to the wave equation in an isotropic, elastic, and spherical earth comes from the formulation of the natural boundary value problem. The result is generally expressed by a triply infinite sum of zonal harmonics that reduce to a doubly infinite sum when azimuthal independence of the source term is assumed (Sato, et al., 1963; Gilbert and MacDonald, 1960). Each term of the series has an unambiguous physical interpretation in terms of normal modes of the earth's free oscillation; while the triple sum is over surface wavelength, radial mode number, and azimuthal mode degree. Since the earth is a finite body, its eigenvalues constitute a discrete set which becomes quite compact toward the higher terms. Each discrete mode corresponds to a standing wave pattern, and the interference of the standing waves gives rise to the travelling waves which show on a conventional seismogram. Further, it can be shown that the higher modes contribute mainly to the body waves, while the lower modes are primarily responsible to the surface waves (Sato et al., 1963). It has been pointed out by Brune (1964) that the energy in the lower modes, especially the fundamental mode, is usually sufficiently separated from the neighboring modes that each individual mode can be analyzed separately. However, the energy in the higher modes is always so closely associated in frequency and time that no part of the time record at any observation point can be analyzed in terms of one mode.

Mathematically, this is equivalent to the statement that the surface waveform can usually be realized by one or a few terms of the series solution. Whereas the realization of a body-wave signal requires the summation of a large number of higher-order terms of the harmonic series which makes the normal mode approach to the body wave problem very impractical, if not impossible. This difficulty does not necessarily suggest that the physical mechanism of body-wave propagation per se is more complex. Rather, it indicates that normal mode expansion in terms of zonal harmonics is efficient only for a long sinusoidal wave train such as the surface waves, but becomes quite inefficient for pulse-like body waves. There are ways to overcome this difficulty (Bremmer, 1949; Ben-Menahem, 1964). By applying the Watson's transformation to the series solution followed by taking the saddle-point approximation of the resulting complex integral, it is possible to reach an approximate solution for the body waves. The phase term of this approximate solution gives expressions of the ray path and the travel time, while the amplitude term gives the factor of geometric spreading. A study of the ray theory reveals that the above saddle-point solution, despite its laborious mathematical derivations, provides hardly any more information than that furnished by the simple ray method.

In the two following sections the ray theory will be expanded and its limitations discussed. In the third section, we shall discuss within the framework of the ray theory the attenuation of seismic waves due to the anelasticity of the earth. Wherever the situation

fails to satisfy the conditions of the ray theory, it will be supplemented with the more rigorous wave theory. Thus in regions like the earth's crust or the core-mantle boundary where the variation of seismic velocities is large within one wavelength, Thomson-Haskell's formulation will be used to account for the effects of reflection and transmission across the layered boundaries, and these will be presented in the fourth section. Inside the shadow zone the observed body waves have gone through a diffracted path along the core-mantle boundary. Wave phenomenon along this path cannot be accounted for by the simple ray theory, we therefore have to make use of the solution to the appropriate boundary value problem. We shall discuss this in the fifth section. In Appendix 3, we shall derive some practical formulas suitable for the electronic computer to calculate the integrals for travel time, ray path, attenuation and the factor of geometrical spreading.

### 3.1. The Ray Theory as an Asymptotic Wave Theory

In the study of certain initial boundary value problems for linear partial differential equations, an important class of asymptotic methods is characterized by the fact that certain space curves, known as "rays," play a fundamental role. All the functions that make up the various terms of the asymptotic expansion can be shown to obey some ordinary differential equations along the rays. Often these equations can be solved immediately, yielding explicit expressions for the asymptotic solution. This asymptotic method is useful because it usually gives necessary information without invoking the

exact solution.

### 3.1.1. Historical Remarks

The original idea of the ray approximation was formulated by Sommerfeld and Runge (1911) following a suggestion from P. Debye. In their argument a scalar function  $u$ , which in our case may represent the displacement field of a longitudinal or transverse wave motion, is assumed to obey the scalar wave equation

$$\nabla^2 u + k^2 u = 0 \quad (3.1)$$

where  $k$  is the wave number, representing either  $\omega/a$  or  $\omega/\beta$ .

Further, the solution of (3.1) is assumed to have the form

$$u = A(\vec{x}) e^{ik_0 \mathfrak{g}(\vec{x})} \quad (3.2)$$

where  $k_0 = \omega/c$  with  $c$  being phase velocity. Both  $A$  and  $\mathfrak{g}$  are independent of the frequency. Direct substitution of (3.2) into (3.1) gives

$$\begin{aligned} -ik_0^2 u \left[ (\nabla \mathfrak{g})^2 - \frac{k^2}{k_0^2} \right] + 2ik_0 u \left[ \frac{1}{2} \nabla^2 \mathfrak{g} + (\nabla \ln A) \cdot \nabla \mathfrak{g} \right] \\ + e^{ik_0 \mathfrak{g}} \nabla^2 A = 0 \end{aligned} \quad (3.3)$$

Dividing (3.3) through by  $k_0^2 u$  and assuming that the resulting last term on the left-hand side, namely :  $\nabla^2 A/k_0^2 A$ , remains small as  $k_0$  becomes infinite, we then find that it is sufficient to satisfy (3.3) by requiring

$$(\nabla s)^2 = \frac{k^2}{k_0^2} \quad (3.4)$$

and

$$(\nabla \ln A) \cdot (\nabla s) + \frac{1}{2} \nabla^2 s = 0 \quad (3.5)$$

(3.4) is the well-known eikonal equation, and its solution  $s = \text{constant}$  gives the wavefront of the propagating discontinuity. By virtue of (3.4), one can show that (3.5) leads to an expression describing the behavior of  $A$  along the orthogonal trajectory to the family of surfaces  $s = \text{constant}$ , or along a ray. With (3.4) and (3.5), most of the results in geometrical optics can be derived. For several decades, Sommerfeld and Runge's formulation of the ray theory had received much attention. Unfortunately, a number of ad hoc assumptions involved make their derivations not completely satisfactory. First, the derivation from the scalar wave equation is not sufficiently general. Secondly, the solution (3.2) represents a very restricted class of field. That  $A$  is assumed to be frequency-independent is only fulfilled for plane waves in a homogeneous medium. Thirdly, the  $s$  and the  $A$ , which constitute the solution to (3.1) through (3.2), are obtained from (3.4) and (3.3) at the limit when  $k_0$  is infinite. This is not quite proper because the solution (3.2) contains the factor  $e^{ik_0 s}$  which has no limit as  $k_0$  becomes infinite.

A desirable derivation should not only be free from the above objections but also be able to offer insight into the connection between the wave theory and the geometrical ray by demonstrating the gradual

transition from one to the other.

### 3.1.2. Asymptotic Ray Theory

Recently, a class of more general ray theories have been extensively developed primarily by J. B. Keller and his colleagues at Courant Institute. A number of papers (in particular, Karal and Keller, 1959; Keller and Karal, 1960, 1963), have offered special interest to the elastic wave propagation in both homogeneous and inhomogeneous media. Following the discussion of Karal and Keller (1959), we may write the equation of motion

$$\begin{aligned} \rho \frac{\partial^2 \vec{U}}{\partial t^2} = & (\lambda + \mu) \nabla (\nabla \cdot \vec{U}) + \mu \nabla^2 \vec{U} + \nabla \lambda (\nabla \cdot \vec{U}) \\ & + \nabla \mu \times (\nabla \times \vec{U}) + 2(\nabla \mu \cdot \nabla) \vec{U} \end{aligned} \quad (3.6)$$

We now seek a time harmonic solution of the form

$$\vec{U} = \vec{A} e^{i\omega(\mathfrak{s} - t)} \quad (3.7)$$

where  $\vec{A}$  and  $\mathfrak{s}$  are functions of  $\vec{x}$ . Substituting (3.7) into (3.6) and cancelling the exponential factor, we obtain

$$\begin{aligned} & -(i\omega)^2 \rho \vec{A} + (\lambda + \mu) (i\omega \nabla \mathfrak{s} + \nabla) (\nabla \cdot \vec{A} + i\omega \vec{A} \cdot \nabla \mathfrak{s}) \\ & + \mu [\nabla^2 \vec{A} + 2i\omega (\nabla \mathfrak{s} \cdot \nabla) \vec{A} + (i\omega)^2 \vec{A} (\nabla \mathfrak{s})^2 + i\omega \vec{A} \nabla^2 \mathfrak{s}] \\ & + \nabla \lambda [i\omega (\vec{A} \cdot \nabla \mathfrak{s}) + (\nabla \cdot \vec{A})] + (\nabla \lambda) \times [i\omega (\nabla \mathfrak{s} \times \vec{A}) + (\nabla \times \vec{A})] \\ & + 2[\nabla \mu \cdot \nabla + i\omega (\nabla \mu \cdot \nabla \mathfrak{s})] \vec{A} = 0 \end{aligned} \quad (3.8)$$

In obtaining (3.8), the following vector identities are used

$$\nabla \times \vec{U} = (\nabla \times \vec{A} + i\omega \nabla \mathcal{S} \times \vec{A}) e^{i\omega(\mathcal{S} - t)}$$

$$\nabla \cdot \vec{U} = (\nabla \cdot \vec{A} + i\omega \vec{A} \cdot \nabla \mathcal{S}) e^{i\omega(\mathcal{S} - t)}$$

We now assume that  $\mathcal{S}$  is independent of frequency. To establish the connection between the geometrical ray theory and the more general wave theory, we assume that  $\vec{A}$  possesses an expansion as inverse powers of frequency

$$\vec{A} = \sum_{n=0}^{\infty} \vec{A}_n (i\omega)^{-n} \quad (3.9)$$

The vectors  $\vec{A}_n$  to be determined are functions of  $\vec{x}$  only. Series expansion of the type (3.9) is suitable for high frequencies. However, experience has shown that it is still useful at frequencies so low that the wavelength is comparable to other dimensions of the problem. Putting (3.9) into (3.8), we obtain

$$\begin{aligned} & \sum_{n=0}^{\infty} (i\omega)^{-n} [ -(i\omega)^2 \rho \vec{A}_n + (\lambda + \mu)(i\omega \nabla \mathcal{S} + \nabla)(\nabla \cdot \vec{A}_n + i\omega \vec{A}_n \cdot \nabla \mathcal{S}) \\ & + \mu \{ \nabla^2 \vec{A}_n + 2i\omega (\nabla \mathcal{S} \cdot \nabla) \vec{A}_n + (i\omega)^2 \vec{A}_n (\nabla \mathcal{S})^2 + i\omega \vec{A}_n \nabla^2 \mathcal{S} \} \\ & + \nabla \lambda \{ i\omega (\vec{A}_n \cdot \nabla \mathcal{S}) + (\nabla \cdot \vec{A}_n) \} + (\nabla \lambda) \times \{ i\omega (\nabla \mathcal{S} \times \vec{A}_n) + \nabla \times \vec{A}_n \} \\ & + 2 \{ (\nabla \mu \cdot \nabla) + i\omega (\nabla \mu \cdot \nabla \mathcal{S}) \} \vec{A}_n ] = 0 \end{aligned} \quad (3.10)$$

Since (3.10) does not just hold for a fixed frequency, the coefficient of each term in the power expansion must vanish. Therefore, we have for  $n = 0$

$$\vec{A}_0 + (\alpha^2 - \beta^2)\nabla\mathcal{S}(\vec{A}_0 \cdot \nabla\mathcal{S}) + \beta^2(\nabla\mathcal{S})^2\vec{A}_0 = 0 \quad (3.11)$$

Taking the dot product of (3.11) with  $\nabla\mathcal{S}$ , it yields

$$\left[ \frac{1}{\alpha^2} - (\nabla\mathcal{S})^2 \right] \vec{A}_0 \cdot \nabla\mathcal{S} = 0 \quad (3.12)$$

The cross product of  $\nabla\mathcal{S}$  with (3.11) gives

$$\left[ \frac{1}{\beta^2} - (\nabla\mathcal{S})^2 \right] \vec{A}_0 \times \nabla\mathcal{S} = 0 \quad (3.13)$$

Since neither  $\vec{A}_0$  nor  $\nabla\mathcal{S}$  is identically zero,  $\vec{A}_0 \cdot \nabla\mathcal{S}$  and  $\vec{A}_0 \times \nabla\mathcal{S}$  cannot be zero simultaneously. Likewise the two expressions inside the brackets in (3.12) and (3.13) cannot vanish at the same time. Therefore, (3.12) and (3.13) resolve into two sets of simultaneous equations

$$\left\{ \begin{array}{l} \vec{A}_0 \times \nabla\mathcal{S} = 0 \end{array} \right. \quad (3.14)$$

$$\left\{ \begin{array}{l} (\nabla\mathcal{S})^2 = \frac{1}{\alpha^2} \end{array} \right. \quad (3.15)$$

and

$$\left\{ \begin{array}{l} \vec{A}_0 \cdot \nabla\mathcal{S} = 0 \end{array} \right. \quad (3.16)$$

$$\left\{ \begin{array}{l} (\nabla\mathcal{S})^2 = \frac{1}{\beta^2} \end{array} \right. \quad (3.17)$$

The first set describes a wavefront propagating at the longitudinal wave velocity  $\alpha$ , having the displacement  $\vec{A}_0$  normal to the wavefront surface. The second set describing a wavefront propagating at the transverse wave velocity  $\beta$ , having the displacement  $\vec{A}_0$  tangential to the wavefront surface. When the medium is homogeneous, the wavefront from a point source forms a family of concentric spheres, and the rays are straight lines. In an inhomogeneous medium, the wavefront is no longer spherical, and the rays are curvilinear curves. These properties of rays and wavefronts will be discussed in more detail in the next section.

Now, again from (3.10) we have for  $n = 1$

$$\begin{aligned}
 & -\rho \vec{A}_1 + \mu (\nabla \mathcal{S})^2 + (\lambda + \mu) \nabla \mathcal{S} (\vec{A}_1 \cdot \nabla \mathcal{S}) \\
 & + (\lambda + \mu) \nabla (\vec{A}_0 \cdot \nabla \mathcal{S}) + (\lambda + \mu) \nabla \mathcal{S} (\nabla \cdot \vec{A}_0) \\
 & + 2\mu (\nabla \mathcal{S} \cdot \nabla) \vec{A}_0 + \mu \nabla^2 \mathcal{S} \vec{A}_0 + \nabla \lambda (\vec{A}_0 \cdot \nabla \mathcal{S}) \\
 & + 2(\nabla \mu \cdot \nabla \mathcal{S}) \vec{A}_0 + 2\mu \times (\nabla \mathcal{S} \times \vec{A}_0) = 0
 \end{aligned} \tag{3.18}$$

(3.14), (3.15), and (3.18) lead to an equation of  $\vec{A}_0$  for the longitudinal wave. On the other hand, (3.16), (3.17), and (3.18) lead to an equation of  $\vec{A}_0$  for the transverse wave.

We shall first treat the case of the longitudinal wave. The last term of (3.18) vanishes by virtue of (3.14), which also implies that

$$\vec{A}_0 = a_0 \nabla \mathcal{S} \tag{3.19}$$

where  $a_0$  is a scalar proportionality factor. Dotting the remaining equation (3.18) by  $\nabla \mathfrak{S}$ , it is easy to show by use of (3.15) and (3.19) that (3.18) reduces to the following simple form

$$2(\nabla \mathfrak{S} \cdot \nabla)a_0 + \frac{1}{\rho} a_0 \nabla \cdot (\rho \nabla \mathfrak{S}) = 0 \quad (3.20)$$

Since  $\mathfrak{S}$  is known from (3.15), therefore (3.20) is an equation for  $a_0$  which, in light of (3.19), yields  $\vec{A}_0$  in question. Now, since  $\nabla \mathfrak{S}$  is a vector normal to the wavefront or tangential to the ray, so  $\nabla \mathfrak{S} \cdot \nabla$  is simply an operator of directional differentiation along a ray. Again (3.15) implies

$$|\nabla \mathfrak{S}| = \frac{1}{a} \quad (3.21)$$

we may therefore write

$$(\nabla \mathfrak{S} \cdot \nabla)a_0 = \frac{1}{a} \frac{d}{ds} a_0$$

where  $s$  is the arclength along the ray. Introducing (3.22) into (3.20), the equation of  $a_0$  can be written in the form

$$\frac{da_0}{ds} + \frac{1}{2} \left[ \frac{1}{\rho} \frac{d\rho}{ds} + a \nabla^2 \mathfrak{S} \right] a_0 = 0 \quad (3.23)$$

This equation describes the amplitude behavior along the ray path.

An integration along the ray path between  $s_1$  and  $s_2$  gives

$$\frac{a_0(s_1)}{a_0(s_2)} = \exp \left[ -\frac{1}{2} \ln \left\{ \frac{\rho(s_2)}{\rho(s_1)} \right\} - \frac{1}{2} \int_{s_1}^{s_2} \left\{ a \nabla^2 g \right\} ds \right] \quad (3.24)$$

To compute the remaining integral, we consider a tube of rays terminating in both ends by  $\Sigma_1$  and  $\Sigma_2$  of the wavefronts

$$s = t_1 \quad \text{and} \quad s = t_2$$

$t_1$  and  $t_2$  being arbitrary constants. Let  $\Sigma_3$  be the cylindrical surface formed by the rays through the circumference of  $\Sigma_1$  and  $\Sigma_2$ . Hence  $\Sigma_1$ ,  $\Sigma_2$  and  $\Sigma_3$  enclose a domain  $V$  in which we apply the divergence theorem to the function  $\nabla^2 g$

$$\iiint_V \nabla^2 g \, dv = \iint_{\Sigma_1 + \Sigma_2 + \Sigma_3} \nabla g \cdot d\vec{\sigma}$$

where  $d\vec{\sigma}$  is the outward normal. Since  $\nabla g$  is tangential to the ray, we have, in light of (3.21)

$$\nabla g \cdot d\vec{\sigma} = - |\nabla g| \, d\sigma_1 = - \frac{d\sigma_1}{a(s_1)} \quad \text{on } \Sigma_1$$

$$\nabla g \cdot d\vec{\sigma} = |\nabla g| \, d\sigma_2 = \frac{d\sigma_2}{a(s_2)} \quad \text{on } \Sigma_2$$

$$\nabla g \cdot d\vec{\sigma} = 0 \quad \text{on } \Sigma_3$$

Therefore, we obtain

$$\iiint_V \nabla^2 \mathbf{g} \, dv = \iint_{\Sigma_2} \frac{d\sigma_2}{a(s_2)} - \iint_{\Sigma_1} \frac{d\sigma_1}{a(s_1)} \quad (3.26)$$

Next we choose an arbitrary wavefront which intersects the tube of rays to form a surface  $\Sigma$ . By expressing that

$$\begin{aligned} d\sigma_1 &= K_1 \, d\sigma \\ d\sigma_2 &= K_2 \, d\sigma \end{aligned} \quad (3.27)$$

where  $d\sigma$  are surface elements of  $\Sigma$ ;  $K_1$  and  $K_2$  are proportional constants measuring the expansion of an infinitesimally narrow tube of ray, we may then write (3.26) as

$$\begin{aligned} \iiint_V \nabla^2 \mathbf{g} \, dv &= \iint_{\Sigma} \left( \frac{K_2}{a(s_2)} - \frac{K_1}{a(s_1)} \right) d\sigma \\ &= \iint_{\Sigma} \int_{s_1}^{s_2} \frac{d}{ds} \left( \frac{K}{a} \right) ds \, d\sigma \end{aligned}$$

The volume element  $dv$  can be written as

$$dv = K \, d\sigma \, ds$$

Therefore, we have

$$\iiint_V \nabla^2 \mathbf{g} \, dv = \iiint_V \left[ \frac{1}{K} \frac{d}{ds} \left( \frac{K}{a} \right) \right] dv$$

Since  $V$  is arbitrary, we must have

$$\nabla^2 g = \frac{1}{K} \frac{d}{ds} \left( \frac{K}{a} \right) \quad (3.28)$$

Note that this result (3.28) is similar to the one obtained by Luneberg (1944) in the case of geometrical optics. Introducing (3.28) into (3.24) and noting that

$$\begin{aligned} \int_{s_1}^{s_2} (a \nabla^2 g) ds &= \int_{s_1}^{s_2} \frac{a}{K} \frac{d}{ds} \left( \frac{K}{a} \right) ds \\ &= \int_{s_1}^{s_2} \frac{d}{ds} \left[ \ln \left( \frac{K}{a} \right) \right] ds \\ &= \ln \left\{ \frac{K_2 a(s_1)}{K_1 a(s_2)} \right\} \end{aligned}$$

we obtain with the aid of (3.27)

$$\begin{aligned} \frac{a_o(s_2)}{a_o(s_1)} &= \exp \left[ -\frac{1}{2} \ln \left\{ \frac{a(s_1) \rho(s_2) d\sigma(s_2)}{a(s_2) \rho(s_1) d\sigma(s_1)} \right\} \right] \\ &= \left[ \frac{a(s_2) \rho(s_1) d\sigma(s_1)}{a(s_1) \rho(s_2) d\sigma(s_2)} \right]^{\frac{1}{2}} \quad (3.29) \end{aligned}$$

In view of (3.19), we finally arrive at the expression of geometrical spreading for the case of the longitudinal wave

$$\frac{|\vec{A}_o(s_2)|}{|\vec{A}_o(s_1)|} = \left[ \frac{a(s_1)\rho(s_1) d\sigma(s_1)}{a(s_2)\rho(s_2) d\sigma(s_2)} \right]^{\frac{1}{2}} \quad (3.30)$$

Here  $d\sigma(s_1)$  and  $d\sigma(s_2)$  denote cross-sectional area of a tube of rays at  $s_1$  and  $s_2$  respectively. More precisely,  $d\sigma(s_1)/d\sigma(s_2)$  is the limit of the area ratio as the tube shrinks to the ray. Likewise, the arguments of  $a$  and  $\rho$  indicate the respective points on the ray where the functions  $a$  and  $\rho$  take on values.

For the case of the transverse wave, a derivation similar to the one described above gives (Karal and Keller, 1959)

$$\vec{A}_o(s_2) = |\vec{A}_o(s_1)| \left[ \frac{\beta(s_1)\rho(s_1) d\sigma(s_1)}{\beta(s_2)\rho(s_2) d\sigma(s_2)} \right]^{\frac{1}{2}} .$$

$$\left[ \vec{p} \sin \{ \epsilon(s_1, s_2) + \epsilon_o(s_1) \} + \vec{b} \cos \{ \epsilon(s_1, s_2) + \epsilon_o(s_1) \} \right] \quad (3.31)$$

where  $\vec{p}$  is the unit normal, and  $\vec{b}$  is the unit binormal of the ray.  $\epsilon_o$  is an arbitrary initial phase,  $\epsilon$  is defined by an integral along the ray

$$\epsilon(s_1, s_2) = \int_{s_1}^{s_2} \frac{1}{T} ds \quad (3.32)$$

with  $T$  being the radius of torsion of the ray defined by (Hildebrand, 1957, p. 295)

$$\frac{1}{T} = - \frac{d\vec{b}}{ds} \cdot \vec{p} \quad (3.33)$$

When the rays are plane curves, as they are in a spherically symmetric medium,  $\vec{b}$  is a constant vector. Through (3.32) and (3.33) we find that  $\epsilon$  vanishes and thus  $\vec{A}_0(s_2)$  is parallel to  $\vec{A}_0(s_1)$ . This implies that in a spherically symmetric medium, the angle of polarization of transverse waves remains unchanged through propagation. In a more general medium, however, the unit vector

$$\vec{p} \sin(\epsilon + \epsilon_0) + \vec{b} \cos(\epsilon + \epsilon_0)$$

rotates about the ray as the transverse wave propagates.

By setting  $n$  equal to 2, 3, 4, ..., one gets essentially a recursive scheme in which equation for  $\vec{A}_n$  is obtainable in terms of all  $\vec{A}_m$ 's with  $m < n$ . Therefore the entire asymptotic series solution (3.7), or (3.9) can be obtained based on the solutions of (3.15) and (3.17), together with the given boundary and initial values. The general equations for  $\vec{A}_n$  and their formal solutions can be found in Karal and Keller (1959). The expansion (3.19) is not the most general one but offers an improvement over the classical ray theory at least in showing the connection with the more rigorous wave theory. Although results derived from (3.7) are for periodic waves, by Fourier integral theorem they can be applied to arbitrary waves.

### 3.2. Rays in a Spherically Symmetrical Medium

The assumption that the elastic properties of the earth are spherically symmetric with respect to its center seems to be good except possibly in the earth's crust, where the wave phenomenon will be considered in section 3.4. It will be shown in this section that

rays in a spherically symmetric medium are plane curves (3.38). Along a ray there exists a constant  $p$  known as ray parameter (3.39), which simply expresses Snell's law. Formulas are derived for the distance integral (3.42), the travel-time integral (3.45), and the geometrical spreading factors (3.49) and (3.50). These integrals, with integrands ordinarily given in terms of a numerical function, can be best evaluated on a computer. The numerical scheme of our computer program will be discussed in Appendix 3.

### 3.2.1. The Path and Transit Time of a Ray

The rays have been defined as the orthogonal trajectories to the wavefronts

$$g(\vec{r}) = t$$

Equations of the rays given by (3.15) and (3.17) have an equivalent vector form

$$\nabla g = \frac{1}{v(\vec{r})} \frac{d\vec{r}}{ds} \quad (3.32)$$

where  $v(\vec{r})$  stands for either  $\alpha$  or  $\beta$ ;  $\vec{r}$  is a position vector of a typical point on a ray, and  $s$  is the length of the ray measured from a fixed point on it. Differentiating (3.32) with respect to  $s$  we obtain

$$\begin{aligned}
 \frac{d}{ds} \left( \frac{1}{v} \frac{d\vec{r}}{ds} \right) &= \frac{d}{ds} (\nabla s) \\
 &= \left( \frac{d\vec{r}}{ds} \cdot \nabla \right) \nabla s \\
 &= (v \nabla s \cdot \nabla) \nabla s \\
 &= \frac{1}{2} v \nabla [(\nabla s)^2] \\
 &= \frac{1}{2} v \nabla \left( \frac{1}{v^2} \right)
 \end{aligned}$$

i. e.

$$\frac{d}{ds} \left( \frac{1}{v} \frac{d\vec{r}}{ds} \right) = \nabla \left( \frac{1}{v} \right) \tag{3.33}$$

In a homogeneous medium,  $v = \text{constant}$  and (3.33) reduces to

$$\frac{d^2 \vec{r}}{ds^2} = 0$$

which immediately gives the solution

$$\vec{r} = \vec{c}_1 s + \vec{c}_2 \tag{3.34}$$

which indicates that in a homogeneous medium rays are straight lines pointing to the direction of  $\vec{c}_1$  and passing through the point  $\vec{r} = \vec{c}_2$ .

Now, if the medium is spherically symmetric, i. e.,

$$v = v(r) \tag{3.35}$$

where  $r$  is the radial variable of the spherical coordinate system, by differentiating the vector function  $\vec{r} \times \left( \frac{1}{v} \frac{d\vec{r}}{ds} \right)$  along the ray,

we have

$$\frac{d}{ds} \left[ \vec{r} \times \frac{1}{v} \frac{d\vec{r}}{ds} \right] = \frac{d\vec{r}}{ds} \times \frac{1}{v} \frac{d\vec{r}}{ds} + \vec{r} \times \frac{d}{ds} \left( \frac{1}{v} \frac{d\vec{r}}{ds} \right) \quad (3.36)$$

Obviously the first term on the right-hand side of (3.36) vanishes.

By virtue of (3.33) and (3.35),

$$\frac{d}{ds} \left( \frac{1}{v} \frac{d\vec{r}}{ds} \right) = \nabla \left( \frac{1}{v} \right) = \vec{e}_r \frac{d}{dr} \left( \frac{1}{v} \right) \quad (3.37)$$

The second term on the right-hand side of (3.36) therefore also vanishes. Hence we conclude

$$\vec{r} \times \frac{1}{v} \frac{d\vec{r}}{ds} = \text{const.} \quad (3.38)$$

This is an important result which implies that rays in a spherically symmetric medium are plane curves and each curve lies within a plane passing through the origin of the coordinates. Moreover, since  $\frac{d\vec{r}}{ds}$  is just a unit vector tangential to the ray, (3.38) can be written as

$$\frac{r \sin \theta}{v} = \text{const.} = p \quad (3.39)$$

where  $\theta$  is the angle between the position vector and the tangent at the point  $\vec{r}$  on the ray. (See Fig. 3.1).  $p$  is the so-called ray parameter which is invariant along a ray. To obtain an explicit formula for the rays, we make use of the result from elementary differential calculus (e.g., Abraham Cohen, Differential Equations,

1933, p. 53) that the angle  $\theta$  for a plane curve is given by

$$\sin \theta = \frac{r}{\sqrt{r^2 + \left(\frac{dr}{d\theta}\right)^2}} \quad (3.40)$$

Introducing (3.39) into (3.38) we have

$$\frac{dr}{d\delta} = \frac{r}{p} \sqrt{\frac{r^2}{v^2} - p^2} \quad (3.41)$$

Integrating equation (3.41) along a ray from the point  $(r_0, \delta_0)$  to the point  $(r, \delta)$ , we obtain the integral representation of the ray in a spherically symmetric medium

$$\delta = \delta_0 + p \int_{r_0}^r \frac{dr}{r \sqrt{\frac{r^2}{v^2} - p^2}} \quad (3.42)$$

The travel time  $t$  of the wavefront along a ray from  $(r_0, \delta_0)$  to  $(r, \delta)$  can be computed by evaluating the integral

$$t = \int_{(r_0, \delta_0)}^{(r, \delta)} \frac{ds}{v}$$

Again we recall from the elementary differential calculus that in spherical coordinates

$$ds = \sqrt{(dr)^2 + r^2(d\delta)^2} \quad (3.43)$$

Eliminating  $d\delta$  between (3.41) and (3.43) we obtain

$$ds = \frac{r dr}{v \sqrt{\frac{r^2}{v^2} - p^2}} \quad (3.44)$$

With (3.44) we can directly write down the travel time integral

$$t = \int_{r_0}^r \frac{r dr}{v^2 \sqrt{\frac{r^2}{v^2} - p^2}} \quad (3.45)$$

Formulas (3.42) and (3.45) are of analytical as well as numerical importance. For a given velocity as a function of  $r$ , (3.42) and (3.45) together serve to predict the space and time relationship of the propagating wave front.

### 3.2.2. The Geometrical Spreading

In 3.1.2 we have obtained expressions predicting the amplitude behavior of the longitudinal wave (3.30) and of the transverse wave (3.31) along a ray in an inhomogeneous medium. Both expressions state the law of energy conservation by simply requiring the energy flow in any cross-section of a certain tube of rays to be constant. In order to render any practical usefulness, these expressions have to be written in terms of measurable quantities. Shown in Figure 3.2 is the geometry of a seismic ray.  $f$  is the focal point,  $P$  is the observation point. The ray takes off at an angle  $\theta$  making with the vertical through  $f$ , and emerges at an angle  $\theta_0$  making with the vertical through  $P$ .  $r_0$  is the radius of the spherical earth centered at  $O$ . Consider the tube of rays inside the solid angle

defined between  $\theta$  to  $\theta + \Delta\theta$  and  $\lambda$  to  $\lambda + \Delta\lambda$ . The tube of rays has a cross-sectional area  $\Delta\sigma(s_1)$  at a point  $s_1$  unit distance from  $f$ , and  $\Delta\sigma(s_2)$  at a point  $s_2$  or  $P$ . The tube of rays intersects the spherical earth's surface forming an area which is tentatively designated by  $\Sigma$ . Since rays in a spherically symmetric medium are plane curves (see 3.38),  $\Sigma$  subtends at  $O$  a solid angle defined between  $\lambda$  to  $\lambda + \Delta\lambda$  and  $\phi + \Delta\phi$ . With these remarks, we can calculate

$$\begin{aligned} \Delta\sigma(s_1) &= \int_{\theta}^{\theta+\Delta\theta} \int_{\phi}^{\phi+\Delta\phi} \sin \theta \, d\theta \, d\phi \\ &= [\cos \theta - \cos \theta \cos \Delta\theta + \sin \theta \sin \Delta\theta] \Delta\phi \end{aligned} \quad (3.46)$$

$$\begin{aligned} \Delta\sigma(s_2) &= \cos \theta_o \Sigma = \cos \theta_o \int_{\lambda}^{\lambda+\Delta\lambda} \int_{\phi}^{\phi+\Delta\phi} r_o^2 \sin \lambda \, d\lambda \, d\phi \\ &= r_o^2 \cos \theta_o [\cos \lambda - \cos \lambda \cos \Delta\lambda + \sin \lambda \sin \Delta\lambda] \Delta\phi \end{aligned} \quad (3.47)$$

Taking the limit as  $\Delta\theta$ ,  $\Delta\phi$  and  $\Delta\lambda$  approach zero, the tube shrinks to a ray and therefore we have

$$\begin{aligned} \lim_{\substack{\Delta\theta \rightarrow 0 \\ \Delta\phi \rightarrow 0 \\ \Delta\lambda \rightarrow 0}} \sqrt{\frac{\Delta\sigma(s_1)}{\Delta\sigma(s_2)}} &= \sqrt{\frac{d\sigma(s_1)}{d\sigma(s_2)}} = \sqrt{\frac{\sin \theta}{r_o^2 \cos \theta_o \sin \lambda} \frac{d\theta}{d\lambda}} \end{aligned} \quad (3.48)$$

Inserting (3.48) into (3.30) and (3.31), we finally obtain the factor of geometrical spreading  $G$  to be

$$G_P \equiv \frac{|\vec{A}_o(s_2)|}{|\vec{A}_o(s_1)|} = \sqrt{\frac{\alpha(s_1)\rho(s_1)}{\alpha(s_2)\rho(s_2)}} \sqrt{\frac{\sin \theta}{r_o^2 \cos \theta_o \sin \delta}} \frac{d\theta}{d\delta} \quad (3.49)$$

in the case of the longitudinal wave; and

$$G_S \equiv \frac{|\vec{A}_o(s_2)|}{|\vec{A}_o(s_1)|} = \sqrt{\frac{\beta(s_1)\rho(s_1)}{\beta(s_2)\rho(s_2)}} \sqrt{\frac{\sin \theta}{r_o^2 \cos \theta_o \sin \delta}} \frac{d\theta}{d\delta} \quad (3.50)$$

in the case of the transverse wave.

It must be noted that these formulas ((3.42), (3.45), (3.49), and (3.50)) are obtained on a more general and rigorous basis. In particular, (3.49) and (3.50) are different from corresponding formulas used in seismology (e.g., Bullen, 1963, p. 126; Jeffreys, 1962, p. 49). The derivations of Bullen and Jeffreys are not sound in their basic, unproven assumption that energy flow in a ray tube is solely proportional to the cross-sectional area of the ray tube. They have not properly accounted for the dependence of energy flow on the local velocity and density. Moreover, their methods of deriving the geometrical spreading factor do not approach the limit of a ray, but the limit of a conical shell instead.

### 3.3. Attenuation Along the Ray

As a result of the anelasticity of the earth, the amplitude of a propagating wave group attenuates with distance. The damping factor,  $AT(\omega)$ , is given by

$$AT(\omega) = \exp \left[ - \frac{\omega x}{2Qv} \right] \quad (3.51)$$

If the body-wave velocity  $v$  and the anelasticity  $Q$  vary in the medium, the distance  $x$  will then be replaced by an integral along the path  $s$  of propagation. Hence, (3.51) takes the following form

$$AT(\omega) = \exp [-\omega t^*] \quad (3.52)$$

where

$$t^* = \frac{1}{2} \int_s \frac{ds}{Qv} \quad (3.53)$$

$t^*$  is obtainable if  $Q$  and  $v$  are given. The function  $v(r)$  is well known from travel time studies. Our present knowledge concerning the earth's anelasticity  $Q$  comes mainly from the measurement of free oscillations and propagating surface waves. Anderson and Archambeau (1964) have been able to invert the attenuation measurements for a  $Q(r)$  function appropriate for shear-type motions. Relations were further established upon certain assumptions, enabling the result to be applicable to compressional waves. (Anderson, et al., 1965). The integral  $t^*$  has a dimension of time. In fact, it can be regarded as the imaginary part of the travel time, and the numerical value of which can be obtained by weighing the travel time integral by the function  $2Q$ . Through (3.45), we can write (3.53)

$$t^* = \frac{1}{2} \int_s \frac{ds}{Qv} = \int_{r_h}^{r_o} \frac{r dr}{2Qv^2 \sqrt{\frac{r^2}{v^2} - p^2}} \quad (3.54)$$

where the subscripts  $o$  and  $h$  refer to the base of the crust and the

source level. With given  $Q(r)$  and  $v(r)$ , the integral (3.54) can be evaluated numerically in several ways depending on the degree of approximation we seek.

Setting  $\eta = r/v$ , and using the transformation (Bullen, 1963)

$$\frac{dr}{r} = \frac{d\eta}{\eta} \left( \frac{1}{1 - \eta \frac{dv}{dr}} \right)$$

(3.54) becomes

$$t^* = \frac{1}{2} \int_{\eta_h}^{\eta_o} \frac{\eta}{Q \left( 1 - \eta \frac{dv}{dr} \right)} \frac{d\eta}{\sqrt{\eta^2 - p^2}} \quad (3.55)$$

If we use a Bullen A velocity model and a  $Q(H)$  model calculated by Anderson and Archambeau (1964), then the numerical evaluation leads to the approximation

$$Q \left( 1 - \eta \frac{dv}{dr} \right) \approx 2$$

This reduced the integral to an elementary one which yields

$$t^* \approx \frac{r_o}{v_o} \left| \frac{\sin(\theta - \theta_o)}{\sin \theta} \right| 10^{-3} \text{ sec.} \quad (3.56)$$

A better approximation can be obtained by recognizing the fact that  $\int F(\eta)(\eta^2 - p^2)^{-\frac{1}{2}} d\eta$  is an elementary integral if  $F(\eta)$  is a polynomial of  $\eta$ . Thus we can fit by least squares the corresponding part of the integrand to a polynomial of a certain degree (degree 4 or 5 is sufficient in actual cases)

$$F(\eta) \equiv \frac{\eta}{Q\left(1 - \eta \frac{dv}{dr}\right)} = \sum_{n=0}^N \bar{a}_n \eta^n \quad (3.57)$$

A simple algebra leads to

$$t^* = \frac{1}{2} \int_{\eta_h}^{\eta_o} \sum_{n=0}^N \bar{a}_n \eta^n \frac{d\eta}{\sqrt{\eta^2 - p^2}} = \frac{1}{2} \sum_{n=0}^N \bar{a}_n I_n \quad (3.58)$$

where

$$I_0 = \ln \left| \frac{1}{\sin \theta_s} + \frac{\tan \theta_s}{\tan \theta_o} \right| \pm \ln \left| \frac{1}{\sin \theta_o} + \frac{1}{\tan \theta_o} \right|$$

$$I_1 = \eta_o \cos \theta_o \left( \frac{\tan \theta_o}{\tan \theta_s} \pm 1 \right)$$

$$I_2 = \frac{1}{2} \left[ p^2 \left( I_0 + \frac{\cos \theta_s}{\sin^2 \theta_s} \right) \pm \eta_o^2 \cos \theta_o \right]$$

$$I_3 = \frac{1}{3} \left[ (p \cot \theta_s)^3 \pm (\eta_o \cos \theta_o)^3 \right] + p^2 I_1$$

$$I_4 = \frac{1}{4} \left[ 3p^2 I_2 + \left( p^4 \frac{\cos \theta_s}{\sin^4 \theta_s} \pm \eta_o^4 \cos \theta_o \right) \right]$$

$$I_5 = \frac{1}{5} \left[ (p \cot \theta_s)^5 \pm (\eta_o \cos \theta_o)^5 \right] + 2p^2 I_3 - p^4 I_1$$

and  $\theta_s = \pi - \theta$ . The upper signs are for  $\theta_s < \pi/2$  and the lower signs for  $\theta_s > \pi/2$ .

Both (3.56) and (3.58) have been programmed in Fortran for an IBM 7094. The output provides the factor of amplitude correction which is necessary for our equalization procedure to be presented

in Chapter 4.

A third approximation is by way of direct numerical integration of (3.54). This approximation consists of subdividing the interval of integration into small segments and approximating functions  $v$  and  $Q$  within each segment by constant or a linear function of  $r$ . This is essentially the same numerical procedure as that used for computing travel time; except that before summing up the travel time, contributions from each layer are weighed by the corresponding  $Q$  values. Details of this will be given in Appendix 3.

### 3.4. Reflection and Transmission Across Layered Boundaries

The validity of the ray theory depends on the condition that the variation of elastic constants is small relative to the wavelength. This condition is not satisfied in regions as the earth's crust and the mantle-core boundary where evidences show a layered structure with possible discontinuities. As a wavefront impinges on these layered boundaries, it causes reverberations which can only be studied by formulating the proper boundary value problem. If the points of reflection and transmission are removed from the source, and if the radii of curvature of these spherical layers are large as compared with the wavelength in concern, it will be sufficient to approximate our problem by the method used to study plane waves in plane parallel layers. With these remarks, we can make use of the results obtained by Thomson (1950) and Haskell (1953, 1960, 1962). Consider the problem of plane waves of angular frequency  $\omega$  and horizontal phase velocity  $c$  impinging upon the base of a semi-infinite medium made

up of  $n$  parallel, homogeneous, isotropic layers. Continuity of two displacement components and two stress components at each interface, plus vanishing of stress components at the free surface, furnish the necessary conditions to determine the response of the layered system in terms of surface displacements  $(u_o, v_o, w_o)$  and reflected wave amplitudes. Haskell has given a clear account on the derivation of the theory. We shall not repeat his derivation here, but shall write out his results on the coefficients of reflection  $\Gamma_t$  and transmission  $\Gamma_r$  with certain minor changes in normalization that will give convenience in our amplitude equalization procedure.

Incident P wave:

$$\begin{aligned}\Gamma_r^{PP} &= [(J_{11} + J_{21})(J_{32} - J_{42}) - (J_{12} + J_{22})(J_{31} - J_{41})] / D \\ \Gamma_r^{PS} &= 2(J_{32}J_{41} - J_{31}J_{42}) / D \\ \Gamma_t^{Pu_o} &= 2c(J_{32} - J_{42}) / D\alpha_n \\ \Gamma_t^{Pw_o} &= 2c(J_{41} - J_{31}) / D\alpha_n\end{aligned}\tag{3.55}$$

Incident SV wave:

$$\begin{aligned}\Gamma_r^{SVP} &= 2(J_{12}J_{21} - J_{11}J_{22}) / D \\ \Gamma_r^{SVSV} &= [(J_{12} - J_{22})(J_{31} + J_{41}) - (J_{11} - J_{21})(J_{32} + J_{42})] / D \\ \Gamma_t^{SVu_o} &= c(J_{12} - J_{22}) / D\beta_n \\ \Gamma_t^{SVw_o} &= c(J_{21} - J_{11}) / D\beta_n\end{aligned}\tag{3.56}$$

Incident SH wave:

$$\Gamma_r^{\text{SHSH}} = \frac{\mu_n^r \beta_n A_{11} - A_{21}}{\mu_n^r \beta_n A_{11} + A_{21}} \quad (3.57)$$

$$\Gamma_t^{\text{SHv}_0} = \frac{2\mu_n^r \beta_n}{\mu_n^r \beta_n A_{11} + A_{21}}$$

We define

$$r_{\beta_n} \equiv \left[ \left( \frac{c}{\beta} \right)^2 - 1 \right]^{\frac{1}{2}}$$

$$D \equiv (J_{11} - J_{21})(J_{32} - J_{42}) - (J_{12} - J_{22})(J_{31} - J_{41})$$

$$J \equiv (J_{ij}) \equiv E_n^{-1} \prod_{m=1}^{n-1} a_m$$

$E_n^{-1}$  and  $a_m$  are matrices given on p. 21 of Haskell (1953); and

$$(A_{ij}) \equiv \prod_{m=1}^{n-1} a_m$$

Here  $a_m$  is given by equation 3 of Haskell (1960).

Each  $\Gamma$  is a frequency dependent complex function that can be regarded as the transfer function for a linear filtering process applied to the incident wave by the layered system. As required by the law of energy conservation, the following relations hold

$$\begin{aligned} |\Gamma_r^{PP}|^2 + |\Gamma_r^{PSV}|^2 &= 1 \\ |\Gamma_r^{SVSV}|^2 + |\Gamma_r^{SVP}|^2 &= 1 \\ |\Gamma_r^{SHSH}| &= 1 \end{aligned} \tag{3.58}$$

A subroutine for (3.55), (3.56), and (3.57) has been programmed in Fortran complex arithmetics. The computed reflection and transmission coefficients can be dumped directly into the main equalization program to be discussed in Chapter 4. In the numerical work, (3.58) is found to be useful as it offers a quick check on the accuracy of the results. Extension of the above subroutine to one which includes fluid layers can be done without major modifications (Wu and Hannon, 1966).

### 3.5. Diffraction by the Core of the Earth

Since we shall only look at the diffracted wave field in some finite time interval, it is sufficient to assume that the fluid core is embedded in an infinite, homogeneous, elastic medium. This diffraction problem has for many decades held the interest of seismologists as well as applied mathematicians. It is interesting to note that more than a century ago, the exact solutions were obtained in a monumental work by Clebsch (1863). But the solutions in terms of infinite series of spherical harmonics are so complex that Clebsch was unable to derive any useful information from them. It was only after the introduction of Watson's transformation (Watson, 1918) the above infinite series has been made tractable. Since then

many authors have worked on the problem, and have obtained results offering various applications. The method has become rather standard. We shall describe it briefly in the following.

As is shown in Figure 3.3, a fluid sphere of radius  $r_c$ , P-wave velocity  $\alpha'$ , and density  $\rho'$  is embedded in an infinite homogeneous elastic medium of P-wave velocity  $\alpha$ , S-wave velocity  $\beta$ , and density  $\rho$ . At the source point  $Q$ , it emits a dilatational displacement potential

$$\Xi = \frac{e^{i\omega(t - \frac{R}{\alpha})}}{i\omega R/\alpha} \quad (3.59)$$

where  $R^2 = r_h^2 + r_o^2 - 2r_h r_o \cos \delta$ . Clearly, the displacement can be calculated by

$$\vec{U} = \nabla \Xi \quad (3.60)$$

Since boundary conditions will be matched at  $r = r_c$ ,  $\Xi$  must be expanded as spherical harmonics with respect to the center of the fluid sphere. This is done by means of the addition theorem derived by Clebsch (1863). When the boundary conditions are satisfied, the resulting series takes the form

$$\Xi = \sum_{n=0}^{\infty} f(n) P_n(\cos \delta) \quad (3.61)$$

where  $f(n)$  denotes some product of spherical Bessel functions, and  $P_n$  is the Legendre function.

Applying Watson's method, the above sum is transformed

into the integral

$$\mathbb{H} = \frac{1}{2i} \int_{\ell} \frac{f(\nu - \frac{1}{2})}{\cos \nu \pi} P_{\nu - \frac{1}{2}} [\cos (\pi - \delta)] d\nu \quad (3.62)$$

taken along the contour  $\ell$  indicated in Figure 3.4. It can be shown that the integrand is an odd function of  $\nu$  which permits the extension of the contour toward the entire negative real axis, as indicated by  $\ell'$ . Therefore, the solution becomes

$$\mathbb{H} = \frac{1}{2} i e^{-i\omega t} \int_{-\infty}^{\infty} \frac{f(\nu)}{\sin \nu \pi} P_{\nu} [\cos (\pi - \delta)] d\nu \quad (3.63)$$

At this point, on substituting for  $f(\nu)$  and  $P_{\nu}$  the integral representation of the Hankel and the Legendre functions, followed by taking the saddle-point approximation, results can be obtained (Van der Pol and Bremmer, 1937; Bremmer, 1949) which are easily interpretable in terms of geometrical ray theory, but are useful only outside the shadow area.

On the other hand, by deforming the contour and closing it up in the upper half-plane, a residue series is obtained which often converges more rapidly than (3.61). A detailed analysis on the poles for this residue series was performed by Nagase (1954a, b, c). For the case of a spherical cavity ( $\alpha' = 0$ ,  $\rho' = 0$ ) he was able to group the poles into three kinds, each giving solutions respectively to the Rayleigh waves, the diffracted P waves, and the diffracted S waves (Nagase, 1956). The diffracted P-wave solution is

$$\begin{aligned}
 \text{III} = & \sum_j \frac{9k_a}{q_j^4} e^{\frac{i\pi}{4}} \left( J_{2/3}(\sigma_j) - J_{-2/3}(\sigma_j) \right)^{-2} (k_a R_{QB} k_a R_{AP})^{-1} \left( \frac{2}{\pi} k_a r_c \right)^{\frac{1}{2}} \\
 & \times \left( \frac{\sin \delta_1 \sin \delta_2}{\sin \delta} \right)^{\frac{1}{2}} \left\{ 1 + \left( \frac{17}{60} + \frac{1}{4} \cot^2 \delta_1 + \frac{1}{4} \cot^2 \delta_2 \right. \right. \\
 & + 32m^6 (1-m^2)(2m^2-1)^{-4} q_j^2 \left. \right\} \exp \left[ -ik_a r_c \delta \left\{ 1 + \frac{1}{2} q_j^2 \right. \right. \\
 & - \frac{4m^3}{3\sigma_j} (1-m^2)^{\frac{1}{2}} (2m^2-1)^{-2} q_j^3 + \frac{1}{120} q_j^4 - \left( \frac{1}{6} - \frac{2m^2+1}{2m^2-1} \right. \\
 & \left. \left. - \frac{16}{3} m^6 (1-m^2)(2m^2-1)^{-4} \left( \frac{4m^3}{3\sigma_j} \right) (1-m^2)^{\frac{1}{2}} (2m^2-1)^{-2} q_j^5 \right\} \right. \\
 & \left. - ik_a R_{QB} - ik_a R_{AP} + ik_a r_c (\cot \delta_1 + \cot \delta_2) \right] \\
 & \times \left( -\frac{1}{8} q_j^4 + \frac{2m^3}{3\sigma_j} (1-m^2)^{\frac{1}{2}} (2m^2-1)^{-2} q_j^5 \right) \left[ 1 + O \left\{ \frac{1}{k_a r_c} \right\} \right] \quad (3.64)
 \end{aligned}$$

where

$$m = \frac{\beta}{\alpha}$$

$R_{QB}$  = distance from Q to B

$R_{AP}$  = distance from A to P

$\sigma_j$  =  $j^{\text{th}}$  root of  $H_{-1/3}^{(2)}(\sigma e^{\pi i}) = 0$

$$q_j = \left( \frac{3\sigma_j}{k_a r} \right)^{1/3} e^{\frac{5\pi i}{6}}$$

Nagase (1956) has shown with numerical examples that the above solution converges fairly rapidly if  $\delta$  is not too small (e.g.,

larger than  $15^\circ$ ). The rate of damping of the diffracted field is proportional to  $\exp \left[ -\sqrt{3/4} (3\sigma_j)^{2/3} (\omega r_c/a)^{1/3} \delta_0 \right]$ .

In the case that  $\delta_0$  is small, which is of particular interest in the study of shadow zone boundary, the above solution is inadequate. It is then necessary to apply the saddle-point method to the residue series by first introducing into it the integral representations of the Hankel and the Legendre functions. This brings about a better convergent series at the expense of that the solution becomes a high-frequency approximation. The method is found to be (Scholte, 1956)

$$\bar{M} = \frac{1}{2}(\pi i) \frac{e^{ik_a(R_{QB} + R_{AP} + r_c \delta_0)}}{(\sin \delta \sin \delta_1 \sin \delta_2)^{1/2}} \frac{(k_a r_c)^{5/6}}{k_a^2 r_h r_o} \sum_j \delta_j^{-1/2} e^{i\delta_j \delta_0 (k_a r_c)^{1/3}} \quad (3.65)$$

where the complex quantity  $\delta_j$  is the  $j^{\text{th}}$  solution of

$$(2\delta)^{1/2} \tan \left\{ \frac{\pi}{4} + \frac{i}{3} (2\delta)^{3/2} \right\} = - (k_a r_c)^{1/3} \frac{\left( \frac{a^2}{a'^2} - 1 \right)^{1/2} \left( 2 - \frac{a^2}{\beta^2} \right)^2}{4 \left( \frac{a^2}{a'^2} - 1 \right)^{1/2} \left( \frac{a^2}{\beta^2} - 1 \right)^{1/2} + \frac{\rho'}{\rho} \frac{a^4}{\beta^4}} \quad (3.66)$$

Using Bullen's model A (i. e.  $\frac{\rho'}{\rho} = 1.865$ ,  $\frac{a}{a'} = 1.68$ ,  $\frac{a}{\beta} = 1.81$ ), (3.66) reduces to

$$(2\delta)^{1/2} \tan \left\{ \frac{\pi}{4} + \frac{i}{3} (2\delta)^{3/2} \right\} - 1.182 \left( \frac{\omega}{2\pi} \right)^{1/3} = 0 \quad (3.67)$$

In two limiting cases, these roots are

$$\delta_j = \frac{1}{2} \left[ 3(j + \frac{3}{4})\pi \right]^{2/3} e^{\frac{\pi i}{3}} \quad \text{for } \omega \rightarrow \infty$$

and

$$\delta_j = \frac{1}{2} \left[ 3(j + \frac{1}{2})\pi \right]^{2/3} e^{\frac{\pi i}{3}} \quad \text{for } \omega \rightarrow 0$$

Scholte has calculated the roots of (3.67) and concluded that the first term in (3.65) provides a sufficient approximation particularly for short-period waves.

## Chapter 4

### METHOD OF BODY-WAVE EQUALIZATION

#### 4.1. The Earth as a Linear System

In Chapter 3 we have discussed body-wave propagation. We have avoided the formidable task of formulating the complete boundary value problem for an inhomogeneous sphere. Instead, based on certain assumptions the body-wave propagation is interpreted on a local basis. In other words, the path of a body wave is divided into several segments and within each segment solution is obtained to approximate locally the physical process. By combining these solutions we have obtained the interpretation of body-wave propagation over its entire path. This treatment has a strong formal resemblance to that of a linear system (Teng and Ben-Menahem, 1965). The analogy is illustrated in Figure 4.1 where a teleseismic body-wave signal from a source  $S(\omega)$  is passed through a series of linear filters before it reaches the tip of the recording pen. Each filter corresponds to a portion of the transmitting medium and is characterized by a complex transfer function  $H(\omega)$  which operates on the input spectrum and modifies its phase and amplitude as it passes through. The final output of this filter series is  $F(\omega)$ , which is measurable at the surface. It is therefore possible to write an observed body-wave spectrum as the product of the source function with a number of appropriate transfer functions. The spectrum of  $P_c S$ , for instance, can be written as

$$F_{P_c S}(\omega) = S(\omega) H_{MC}^P(\omega) H_{CM}^{PS}(\omega) H_{MC}^S(\omega) H_{CR}(\omega) H_{INS}(\omega) \quad (4.1)$$

where each transfer function stands for a segment of the wave path with

- $H_{MC}^P(\omega)$  Propagation of a P wave from source to core-mantle boundary.
- $H_{CM}^{PS}(\omega)$  Reflection off the layered core-mantle boundary, P wave has converted to S wave.
- $H_{MC}^S(\omega)$  Propagation of an S wave from core-mantle boundary to the base of the crust.
- $H_{CR}(\omega)$  Transmission across the layered crust giving rise to surface displacement.
- $H_{INS}(\omega)$  Transmission through the instrument.

Writing these complex functions in terms of amplitude and phase spectrums, we have

$$S(\omega) = A_o(\omega) e^{i\Phi_o(\omega)} \quad (4.2)$$

$$F(\omega) = A(\omega) e^{i\Phi(\omega)} \quad (4.3)$$

and similarly

$$H_{MC}(\omega) = A_{MC}(\omega) e^{i\Phi_{MC}(\omega)}$$

$$H_{CM}(\omega) = A_{CM}(\omega) e^{i\Phi_{CM}(\omega)}$$

$$H_{DF}(\omega) = A_{DF}(\omega) e^{i\Phi_{DF}(\omega)} \quad (4.4)$$

$$H_{CR}(\omega) = A_{CR}(\omega)e^{i\Phi_{CR}(\omega)}$$

$$H_{INS}(\omega) = A_{INS}(\omega)e^{i\Phi_{INS}(\omega)}$$

For a given body-wave phase, one must select a correct combination of transfer functions from (4.4) such that every segment of the wave path is appropriately accounted for. Let  $H(\omega)$  be one of these combinations,

$$H(\omega) = \prod_j H_j(\omega) = \prod_j A_j(\omega) e^{i\sum_j \Phi_j(\omega)} \quad (4.5)$$

where  $j$  denotes any appropriate subscript in (4.4). It follows that

$$A(\omega) = A_o(\omega) \prod_j A_j(\omega) \quad (4.6)$$

$$\Phi(\omega) = \Phi_o(\omega) + \sum_j \Phi_j(\omega) \quad (4.7)$$

and inversely that

$$A_o(\omega) = A(\omega) / \prod_j A_j(\omega) \quad (4.8)$$

$$\Phi_o(\omega) = \Phi(\omega) - \sum_j \Phi_j(\omega) \quad (4.9)$$

(4.6) and (4.7) are used to predict a body-wave signal when source function and medium transfer function are known. On the other hand, (4.8) and (4.9) are used to retrieve the source information from observed body-wave signals through a known medium. The procedure, which makes use of the above relations to equalize body-wave field at

one point to another, shall be collectively called the method of body wave equalization.

#### 4.2. Computation of the Transfer Functions

Now, we shall give explicit expressions for the amplitude functions  $A_j(\omega)$  and phase functions  $\Phi_j(\omega)$ .

The transfer function  $H_{INS}(\omega)$  for the instrument can be obtained by Fourier-transforming the calibration trace on each seismogram (Espinosa et al., 1962). Figure 4.2.a shows one of the calculated examples for a World-Wide Standardized Long-Period Seismograph. The result is good in the longer periods, but the numerical error builds up in the short-period part due to the multiplication of the transformed amplitude by  $\omega^3$ , an operation pertaining to a step-type calibration input. An alternative method for obtaining  $H_{INS}(\omega)$  can be deduced from the theory of seismograph (e.g., Benioff, 1932). For a critically damped instrument, it can be shown that

$$A_{INS}(\omega) = \frac{M\omega^3}{(\omega_o^2 + \omega^2)(\omega_g^2 + \omega^2)} \quad (4.10)$$

$$\Phi_{INS}(\omega) = \frac{1}{\pi} \left( \tan^{-1} \frac{\omega_o}{\omega} + \tan^{-1} \frac{\omega_g}{\omega} \right) - \frac{1}{4} \quad (4.11)$$

where  $\omega_o = 2\pi/T_o$ ,  $\omega_g = 2\pi/T_g$ .  $T_o$  and  $T_g$  are periods of pendulum and galvanometer, respectively, of the instrument.  $M$  is a normalization constant appropriate to the peak magnification of each

individual record. Assuming the condition of critical damping, we derive the instrumental transfer function from (4.10) and (4.11).

A typical numerical result for a World-Wide Standardized Long-Period Seismograph having instrumental characteristics  $T_0 = 30$  sec. and  $T_g = 100$  sec. is shown in Figure 4.2.b.

The transfer function  $H_{CR}(\omega)$  and  $H_{CM}(\omega)$  for layered boundaries are calculated by using the Thomson-Haskell matrix formulation discussed in section 3.4. For a given body-wave phase, one has to select the correct combination of the complex functions  $\Gamma_r$ 's and  $\Gamma_t$ 's, the product of them giving the desired transfer function  $H_{CR}(\omega)$  or  $H_{CM}(\omega)$ . In practice, a computer subroutine, with inputs of layered structure and phase velocity, generates the amplitude and the phase functions which are directly applied to the equalization procedures outlined from (4.6) to (4.9).

The transfer function  $H_{DF}(\omega)$  accounts for the diffracted path. When the diffracted path is long,  $H_{DF}(\omega)$  can be calculated from (3.64), the first term of which gives a good approximation for  $\Delta_0 > 30^\circ$ . On the other hand, (3.65) must be used when the diffracted path is short. Note that (3.64) is the solution for a spherical cavity, and (3.65) is a high-frequency approximation. Therefore, a better estimate of the function  $H_{DF}(\omega)$  requires a more completely developed diffraction theory.

Thirdly, the transfer function  $H_{MC}(\omega)$  is for the region where ray approximation is assumed to hold. Its amplitude part  $A_{MC}(\omega)$  can be expressed as a product of two physically distinct factors:

$$A_{MC}(\omega) = G \times AT(\omega) \quad (4.12)$$

$G$  is a factor due to geometrical spreading which is given by (3.30) or (3.49) in the case of P waves, and by (3.31) or (3.50) in the case of S waves.  $AT(\omega)$  is the attenuation function defined and discussed in section 3.3, where two simple approximations (3.56) and (3.58) are given. Computer programs written for both approximations are used in studies to be presented in Chapter 5 and Chapter 6. An improved numerical scheme which carries the computation to a much higher degree of accuracy is presented in Appendix 3. Programs employing this scheme is used in a study on body-wave attenuation to be given in Chapter 7.

On the other hand, the phase function  $\Phi_{MC}(\omega)$  can be expressed by

$$\Phi_{MC}(\omega) = \frac{\omega}{2\pi} \left( \frac{\Delta}{c} - t_0 \right) + [n(\omega) - 1] \quad (4.13)$$

where  $\Delta = r_0 \Delta$  is the epicentral distance,  $c$  is the phase velocity,  $t_0$  is the difference between the time of origin and the first arrival of the signal. The mode number function  $n(\omega)$  for the propagating body wave is that introduced and measured by Brune (1964). In obtaining  $\Delta$ ,  $c$  and  $t_0$ , the results in (3.42) and (3.45) have to be used.

PART II  
APPLICATIONS

Chapter 5

MECHANISM OF DEEP EARTHQUAKES FROM SPECTRUMS OF  
ISOLATED BODY-WAVE SIGNALS -- THE BANDA SEA  
EARTHQUAKE OF MARCH 21, 1964

5.1. Introduction

It has long been recognized by seismologists that one of the purest pieces of information diagnostic of a seismic source is carried by the first few oscillations of the P waves. Especially in the case of a deep earthquake, the whole P wave signal is usually well isolated from the later arrivals, so that no significant contamination with the latter is likely to occur. In view of the success achieved by the first-motion theory, there is good reason to believe that, when the entire P wave signal is entered into the analysis, the information extracted therefrom will not only furnish us with a fault-plane solution, but will also give some insight into the physical processes occurring in the source region.

To achieve this purpose, we find an immediate application of the theory developed in the previous two chapters. According to the method described therein, the equalization of observed body-wave spectrums to the source region is accomplished by performing the following corrections: (1) compensation for the instrumental response, (2) removal of the distortions due to a layered crust, and (3) compensation for the loss from attenuation and geometrical spreading.

In the present study we shall be concerned primarily with the

application of the theory to a deep shock and then proceed to study its source function in space and time and its energy release.

## 5.2. Data

A deep-focus earthquake in the Banda Sea region (epicenter 6.4 S, 127.9 E) that occurred on March 21, 1964 (origin time 03 42 19.6 UT), was chosen for the present study. Its focal depth determined from 15 pP - P, and 11 sP - P measurements was 350 km  $\pm$  20 km, which agrees closely with the value 367 km given by USCGS. From the P waves in Guam and surface waves in Pasadena, the Richter magnitude of the earthquake was computed to be 6-1/4 to 6-3/4. Records were obtained mainly from USCGS Standardized Seismograph Network. Each station consists of three matched components of short-period as well as long-period instruments. Our primary interest was the long-period records; the short-period records were used only for measuring the phase arrival times and for checking the P wave polarity against the long-period records. Figure 5.1 shows the response curve of long-period instruments which have a pendulum period  $T_o = 30$  sec. and a galvanometer period  $T_g = 100$  sec. with their peak magnification at about 25 sec. We note from the response curve that these long-period sensing devices ought to furnish reliable information on earth motion in the period range 10 to 100 sec. The peak magnification of the long-period instruments varies from 750 to 3000. The instrumental response is routinely calibrated every day. The stations whose records were entered into spectral analysis are shown in Figure 5.2 together

with their positions relative to the epicenter. Records from two of these stations, MTJ and HON, were made available by the courtesy of Lamong Geological Observatory. Long-period instruments of these records have frequency characteristics similar to those of the USCGS network instruments. With smaller pendulum and galvanometer periods ( $T_o = 15$  sec.,  $T_g = 75$  sec.), their response curves shift slightly toward the short-period end with their peak response still at 14 sec. Table 5.1 lists all the stations and the necessary information extracted from their records before they were Fourier analyzed. The take-off angle  $\theta$  and the incidence angle  $\theta_o$  as defined in Figure 5.3, were calculated on the basis of a Jeffreys model. Notice that  $\theta_o$  is defined at the base of the crust. This is done for the convenience of later calculation of the crustal response. The determination of P wave first motion is unambiguous, since agreement has been obtained for all six components.

On most of the records used for spectral analysis the P waveforms are clear with a high signal-to-noise ratio and a well-defined zero motion line, both of which are important for a good spectral measurement. In a few cases (MUN, MTJ, NHA, SEO, WEL), the recorded P waves ride on an easily identifiable instrumental noise, which has a period of a few minutes and can be removed without much difficulty. However, P waves from MTJ and HON are heavily masked by microseismic noises, and it was not possible to remove the noise even by numerical filtering. The S waves in general are contaminated to some extent by the preceding or the following phases.

Only a few stations are located in some particular epicentral distance range so that this contamination becomes very small. At a few stations, the instruments are oriented in such a way that completely separate SV and SH motions are recorded.

### 5.3. Data Analysis, P Waves

#### 5.3.1. Choice of the Time Window and its Effect on the Resulting Spectrum

The presence of interfaces in a bounded elastic medium such as the earth makes it difficult, if not impossible, to isolate a complete wave signal. In the simplest case of the P wave, its rather rapidly damping oscillatory signal tail would unavoidably interfere with the later arrivals. To ensure the exclusion of these later phases, the time window (a rectangle of unit height) must not be too long; however, a window of insufficient length would leave out the converted waves and multiple reverberations derived from the original P-wave-front which impinges at the layered crust. It was pointed out by Ben-Menahem et al. (1965) that 45 sec. would be a suitable window length for an earthquake of focal depth greater than 300 km. The truncation of the signal tail, though generally small, does introduce into the resulting spectrum a dc as well as very low frequency components. These errors cannot be avoided; the presence of noise and later phases makes the recovery of the true signal tail impossible. The sharp termination of a signal introduces another type of error. This affects the resulting spectrum not only in the short-period part but also in the part of our primary concern. Tapering the signal by a

Gaussian or cosine taper is a common technique (Kasahara, 1957; Tukey, 1959) for eliminating the sharpness of the termination. We found, however, that tapering the signal tail by hand was sufficient, because the amplitude of the signal near the point of truncation usually was very small. The signal was digitized at a rate of one point per second and spectral analysis was performed by using the modified trapezoid numerical integration routine. No filtering of the P pulses was necessary. Short period noise between 4 and 8 sec., mainly of microseismic origin, were present in a few records, but their presence can hardly alter the amplitude spectrum in the period range of interest. Therefore, denoting  $f(t)$  as the time signal, we define a complex function  $F(\omega)$  as

$$F(\omega) = \int_{-\infty}^{\infty} f(t)e^{-i\omega t} dt \quad (5.1)$$

The amplitude spectrum  $A(\omega)$  and the phase spectrum  $\Phi(\omega)$  are defined as

$$A(\omega) = |F(\omega)| \quad (5.2)$$

$$\Phi(\omega) = \tan^{-1} \frac{\text{Im } F(\omega)}{\text{Re } F(\omega)} \quad (5.3)$$

The resulting spectrums of periods longer than 100 sec. are believed to be considerably affected by the finiteness of the time window and will not be used in the following analysis.

### 5.3.2. Equalization of Spectrums

Since only direct P-wave spectrums are considered in the present source study, our body-wave equalization problem is simplified to one as shown in Figure 5.5. (4.8) therefore reduces to

$$A_o(\omega) = \frac{A(\omega)}{A_{INS}(\omega) A_{CR}(\omega) A_{CM}(\omega)} \quad (5.4)$$

We computed  $A_{INS}(\omega)$  according to (4.10) for the appropriate instrument. To obtain  $A_{CR}(\omega)$ , the body-wave phase velocity was obtained by differentiating the travel-time curve. Crustal structures were assumed to be the same for all stations. This appears justifiable for wave period longer than 10 sec. A comparison is made in Figure 5.5 of the functions  $A_{CR}(\omega)$  calculated from two utterly different crustal structures. The difference between the two curves, about 5%, is not important as far as the present accuracy of the wave spectrum measurements is concerned. The numerical values of  $A_{CR}(\omega)$  for model P-GG (Gutenberg Pacific 6EGH crust) are presented in Figure 5.6 for different phase velocities.

$G$  was computed by (3.49) with the help of Ritsema's tables (1958), and  $AT(\omega)$  was computed by (3.52) and (3.56). The resulting  $A_{MC}(\omega)$  for a set of rays is shown in Figure 5.7. It is found that for long-period P waves the effect of attenuation is not very pronounced and the function  $A_{MC}(\omega)$  is primarily governed by the factor of geometrical spreading. This factor, in turn, depends strongly on the function  $d\theta/d\lambda$ . Therefore, it appears that a direct measurement of  $d\theta/d\lambda$  would be crucial in further body-wave amplitude studies.

All the above numerical calculations were programmed for a digital computer in such a way that the inputs were the digitized time signals together with all the pertinent information, such as the epicentral distance, phase velocity, and crustal structure. The computer generated wave spectrums and transfer functions, performed the operations indicated by (5.4), and typed out and plotted the resulting  $A_0(\omega)$ .

In Figure 5.8 we have summarized the results of the above operations. The azimuthal distribution of stations is indicated at the top. Stations in the first and fourth quadrants have their results displayed in the right half of the figure; those in the second and third quadrants are displayed in the left half. Several features of interest are seen in this figure. In the first place, great similarity exists among the P-wave signals. If these signals are normalized and passed through a low-pass filter with cutoff at, say, 10 sec., they would all look the same. This indicates that the waveform of long-period body waves does not vary appreciably with various paths and crustal structures. It also indicates that for an earthquake of magnitude smaller than 7, long-period body waves do not serve as an efficient tool with which to estimate the source dimensions. From the amplitudes of the P waves, we can approximately locate the nodal line which passes on one side through station AAE where no P wave was recorded and the S wave was strong and clear. On the other side, a similar situation occurs at station AFI (not shown in this figure) whose azimuth lies between those of stations PMG and CTA. Second,

the dc component is in general present in the normalized spectrums  $A(\omega)$ . Although there is sufficient evidence that seismic sources radiate dc energy, the fact that USCGS standardized long-period instruments do not respond to zero frequency makes it clear that the dc component in our spectrums is extraneous and has been introduced by unsatisfactory isolation of the complete wave signal or by an incorrect placing of the zero-motion line, or both. Errors from the above sources may also affect the long-period part of the spectrums; however, the effect decreases with period. As a consequence of the equalization procedure, the source spectrums  $A_0(\omega)$  approach infinity as  $\omega$  approaches zero, and they also suffer some distortions at the long-period end. Therefore, in deriving the following spectral radiation patterns, the part of the data with a period longer than 100 sec. was purposely discarded.

### 5.3.3. Spectral Radiation Patterns of P Waves

From the resulting source spectrums,  $A_0(\omega)$ , radiation patterns are immediately obtained by fixing the wave period and plotting the amplitudes as a function of azimuth (Figure 5.9). The remarkable similarity among these patterns indicates that the spatial and time parts of the source function are uncoupled, a result to be expected from a small source as seen through a long-period spectral window. The largest variation of an individual station comes from station MTJ (numbered 1 in Figure 5.9). This discrepancy is probably due to the fact, as mentioned before, that the P wave of station MTJ was recorded in a background of high microseismic noise as well as

long-period instrumental noise. Moreover, the instrument itself was slightly underdamped.

The body-wave radiation pattern is a three-dimensional configuration. On the focal sphere, each station corresponds to a point that can be specified by two coordinates ( $\theta, \phi$ ). The range of  $\theta$  for teleseismic rays is small (in our case  $120^\circ < \theta < 160^\circ$ ). Therefore, we have suppressed the coordinate  $\theta$  and plotted the patterns (which otherwise would have been a surface) in lines which are shown in Figure 5.9.

#### 5.3.4. Determination of Source Parameters

Formulas were given in section 2.4.2.c and were programmed on the computer to generate vertical and horizontal radiation patterns from a point source. A diagram of the source geometry was shown in Figure 2.1. To ensure the uniqueness of the resulting fit within the scope of a double-couple point source, we calculated patterns for all possible combinations of  $\delta$ ,  $\lambda$  and strike angles. On an IBM 7094 computer it took only 1 minute to compute 400 patterns each consisting of 21 stations. Symmetry conditions existing between  $\delta$  and  $\lambda$  have further reduced the required labor. We started with a  $5^\circ$  grid in the  $\delta$ - $\lambda$  plane and finally narrowed it down to  $1^\circ$ . The resulting fitted model was  $\lambda = 315^\circ$ ,  $\delta = 84^\circ$ , and strike azimuth =  $85^\circ$ . In Figure 5.10 we have compared the calculated result with an observed one. The essential features of the two are very well matched. It must be added that the calculated patterns are rather sensitive to the variation of source parameters. A change of  $5^\circ$  in any one of these

parameters would result in a distinct departure from the empirical results. With these source parameters, we have computed theoretical radiation patterns for different take-off angles. The results are presented in Figure 5.11. Our observations show that a particularly strong P wave is ordinarily associated with a very weak pP wave, and vice versa. This phenomenon is explained in Figure 5.11. Teleseismic P waves are radiated in the interval  $120^{\circ} < \theta < 160^{\circ}$ , and pP waves in the interval  $20^{\circ} < \theta < 55^{\circ}$ . Radiation patterns for these two different intervals are, indeed, complementary to each other.

#### 5.4. Auxiliary Studies

##### 5.4.1. Radiation Pattern of S Waves

The quality of S wave signal is, in general, not good enough to justify the effort of digital Fourier analysis. Therefore, we employed the simplified method of the stationary phase. The method consists of measuring the amplitude and the prominent period of a wave signal and considering the measurement as the relative amplitude spectrum appropriate to that particular period. The measurements were made on the Z component of the long-period records, which excluded the SH wave and gave rise to purely SV motions. The measured periods of the S wave ranged from 15 to 25 sec.; the measured amplitudes were accordingly equalized to the neighborhood of the source by the same procedure described for the P waves, except of course that a shear Q structure was used to compute the diminution and an SV incident wave was used to compute the crustal

transfer function. The equalized amplitudes are shown in the left half of Figure 5.12. The measurements of S wave amplitudes are not good enough to be adequately inverted for source parameters. Nevertheless, the data constitute discriminative evidence to test the double-couple assumption and the P wave results. In the right half of Figure 5.12 is the calculated SV radiation pattern from a double-couple point source, having the same source parameters as those derived from the P waves. General agreement between the observed and calculated radiation patterns is seen; both have a four-lobe structure (one of the lobes has only one sample point, corresponding to station 19), and both are elongated in the NW-SE direction.

#### 5.4.2. Results from First Motion

The data on which the first-motion solutions were based are listed in Table 5.1. Observations are plotted in Figure 5.13, using Hodgson's extended distances (Hodgson and Storey, 1953). Of a total of 34 P wave first motions, only one is inconsistent with the position of the solution circles. In view of the previous result from spectral radiation patterns, only one of the two choices of a fault-plane circle seems feasible -- that which yields the first-motion solution  $\delta \approx 83^\circ$ ,  $\lambda \approx 310^\circ$ , strike azimuth  $94^\circ$ . The angles of dip and strike are fairly well defined; however, owing to the scarcity of near-focus observations, we can obtain only a bound for the slip angle. It has to be larger than  $310^\circ$ . Nevertheless, this result shows a high degree of agreement with the solution derived from P wave spectrums. Only 25 observations of S waves are available. Some of the determinations

of the first motions are questionable. Scarcity and uncertainty of observations allow too much freedom in the choice of the solution, and we therefore use the S wave data only as a check on our double-couple assumption. Curves in the right half of Figure 5.13 are SV nodal lines (Ben-Menahem et al., 1965) appropriate for a double-couple source which has the same source parameters as those derived from P wave spectrums. For a single-couple source, however, these data admit no reasonable solution.

#### 5.5. Source Time Function and Energy Release

As we have seen in Figure 5.8, the equalized spectrums,  $A_0(\omega)$ , are remarkably similar. A better comparison is presented in the lower half of Figure 5.14, where the spectrums have been normalized to their values at 30 sec. The plots are superimposed. Spectrums of stations PMG, RAB, NHA, and SHI have been left out to avoid possible complication, since their locations were too close to a nodal line. No value is given for periods greater than 100 sec. The mean spectrum in the period range 10 to 100 sec. suggests a source time function of the form of a build-up step.

$$g(t) = C(1 - e^{-t/\tau})H(t) \quad (5.5)$$

with a corresponding amplitude spectrum

$$|S(\omega)| = \frac{C}{\omega(1 + \omega^2\tau^2)^{\frac{1}{2}}} \quad (5.6)$$

where  $\tau$  is a time constant. A reasonable fit to the mean spectrum

can be obtained if  $\tau$  is chosen in the interval  $0 < \tau < 3$  sec. A distinct departure from a fit will result if  $\tau > 10$  sec. The calculated spectrum for  $\tau = 3$  sec. is shown by circles in the lower half of Figure 5.14. The corresponding time function is shown in the upper half of the same figure. It is interesting to see the possible rapidity of the process occurring at the source. Similar results from Love and Rayleigh waves from the same shock in the period range 50 to 400 sec. also suggest a source of step-type time dependence. We must, however, emphasize that the above result is hardly more than a probable inference. A more definite and detailed structure of the source time function must await further knowledge of the source amplitude spectrum beyond the limited period range, as well as knowledge of the source phase spectrum.

By equating (2.50) to the resulting equalized P-wave spectrums and taking into account the radiation pattern, we find

$$L_0 ds = 7 \times 10^{-2} \text{ km}^3 \quad (5.7)$$

If we assume  $L_0 = 0.5$  m,  $ds$  equals  $140 \text{ km}^2$ , or an area of  $10 \text{ km} \times 14 \text{ km}$ , which is quite reasonable for an earthquake of magnitude  $6\text{-}1/2$  to  $6\text{-}3/4$ .\* Moreover, invoking our previous result (2.81), we find the energy release

---

\* Båth and Benioff (1958) obtained  $L_0 = 5$  m for the Kamchatka earthquake of November 4, 1952, which had a magnitude of  $8\text{-}1/2$ .

$$E = \frac{\lambda + 3\mu}{4\pi} [L_0 ds] \frac{L_0}{d} = 1.01 \times 10^{22} \text{ erg} \quad (5.8)$$

Notice that this is not the partial energy carried by P wave alone; it is the total energy released by the seismic source, provided that the finiteness of the earth does not significantly change the partition of energy among P, S, and the other waves. In the above computations,  $\lambda = 11.45 \times 10^{11}$  dynes/cm<sup>2</sup> and  $\mu = 8.25 \times 10^{11}$  dynes/cm<sup>2</sup> are used. The quantity inside the brackets of (5.8) is measurable from (5.7). The quantity  $L_0/d$  is equivalent to a shear strain. Tsuboi (1956) has estimated that the ultimate strain of the crustal material is of the order  $10^{-4}$ . Taking as before  $L_0 = 0.5$  m, and assuming that  $d = 1$  km, \* we have found  $L_0/d = 5 \times 10^{-4}$  for a depth of 367 km.

Variation of the quantity  $L_0/d$  by an order of magnitude seems unlikely. On the other hand, if energy can be obtained in some other independent way, (5.8) will furnish information concerning the source displacement and the fictitious fault width.

---

\*The width of the aftershock zone of Kamchatka earthquake of November 4, 1952, is about 100 km (Båth and Benioff, 1958).

MECHANISM OF DEEP EARTHQUAKES FROM SPECTRUMS OF  
ISOLATED BODY-WAVE SIGNALS -- THE BRAZIL  
EARTHQUAKE OF NOVEMBER 9, 1963

6.1. Introduction

In the study of the Banda Sea earthquake presented in Chapter 5, it was found that the equalized P-wave amplitudes from a source at a depth of 367 km fit the model of a shear fault instead of a normal fault. This finding stands in contrast to the suggestion by Benioff (1963) who, in comparing ultralong-period strain seismograms guided by Lamb's solution (1904) of a surface source and Pekeris' solution (1955) of a buried source, suggested that deep earthquakes were generated by a sudden volume contraction at the focus. The difference in interpretation of the source mechanism of deep earthquakes motivated the present study which seeks to check whether the source mechanisms are different for occurrences in different tectonic regions, or there exists a transition zone at some depth across which source mechanism varies from one type to another. The present study also serves to check the validity of the method of body-wave equalization. Since the method was developed with a few assumptions which are hard to prove on theoretical basis, its applicability in another earthquake would add to its empirical verification.

It would be desirable to study the same deep Peruvian earthquakes examined by Benioff (1963), but the World-Wide Standardized Seismograph Network, which are sources of our data, were not established then. Instead, we have selected for the present purpose

a Brazilian earthquake with the same depth ( $h = 600$  km) that occurred just one degree in distance from those deep Peruvian earthquakes. Moreover, the ultralong-period seismogram recorded at the same station Ñaña is available and shows almost identical waveform as those from the previous deep Peruvian earthquakes. Therefore it seems to be reasonable to assume that all these earthquakes belong to the same general source region, and were excited by similar focal mechanisms.

## 6.2. Data

The deep Brazil earthquake (epicenter  $9.0$  S,  $71.5$  W) occurred on November 9, 1963 (origin time 21 15 30.4 UT), has a magnitude of  $6\text{-}3/4$  to 7 as assessed by both stations at Pasadena and Berkeley. Its focal depth determined from 31 pP - P and 26 sP - P measurements was  $550 \pm 20$  km. Long-period records were obtained from USCGS World-Wide Standardized Seismograph Network. The frequency response of this network has been discussed in Chapter 5. A list of all the stations with relevant information is given in Table 6.1. Figure 6.1 shows geographic distribution of the recording stations. The stations whose records of P waves are used in the spectral analysis are connected with the source point by great-circle paths. This earthquake offers a good opportunity for seismic source studies because a great number of the recording stations are located in North America and Europe where crustal structures are better known than the other parts of the world. The body waves of this earthquake were so sharp and strong that many local recording stations were

knocked off-scale, and more stations, from beyond the shadow zone boundary up to the antipole, recorded large diffracted P waves and core phases. As a consequence, P waves on the z-component were incomplete in a few records, and the horizontal components had to be used instead, which requires the use of a horizontal crustal transmission coefficient to properly project the surface displacement to the base of the crust. P waves are digitized at the rate of one point per second. To isolate the P signal from the later phases, we take a 60-sec. time window starting at its onset. For the present deep earthquake, pP never enters into this window, but PcP does at a distance beyond  $60^{\circ}$ . In a few cases PcP is as large as 20% of the maximum P amplitude, and a cosine taper has to be applied to the signal in order to reduce the distortion of the resulting spectrums. At a distance beyond  $80^{\circ}$ , PcP and P are practically indistinguishable; essentially they form one wavefront. It is not as yet very clear where the shadow zone begins, which is a topic of much current interest. For a 550 km deep earthquake, the Jeffreys-Bullen table gives the shadow zone boundary at  $102^{\circ}$ . In the present study, a few stations located beyond  $102^{\circ}$  are included. Some interesting consequences of this inclusion will be presented later.

### 6.3 Transfer Functions

The methods of computing the transfer functions have been discussed in section 4.2, and further exemplified in section 5.3. Here we shall only present the computed results and discuss the models on which these computations are based.

World-wide crustal structures have been available only recently through the wide application of explosion seismology. A compiled result is given by Steinhart and Meyer (1961), in which P-wave crustal structures alone are tabulated. Direct measurement of S-wave crust is still impossible at present. Not many gravity data are collected on a tectonic scale, even less often are their interpretations carried down to the depth of the mohole. Consequently we shall derive the S-wave and density structures from the P-wave crust through some known empirical formulas. Nafe and Drake's velocity density curve (Figure 6.2a) is used to obtain the density structure of the crust; and the Poisson's ratio (Figure 6.2b) appropriate to a Gutenberg earth model is used from which S-wave velocity can be calculated by

$$\beta = \alpha \left[ \frac{1 - 2\sigma}{2(1 - \sigma)} \right]^{\frac{1}{2}}$$

The resulting crustal structures are given in Table 6.2. The profile number is taken from Steinhart and Meyer (1961) where original references can be found. In the last column of Table 6.2, the station code is given to indicate which profile is used to compute the corresponding crustal transfer function. Instead of differentiating the travel time curve, the phase velocity needed in the above calculation is implicitly given by (3.42). Through the direct numerical integration of the distance integral, this result is presented in Figure 6.3. Also shown in the same figure are the take-off angle,  $\theta(\lambda)$ , and its derivative,  $d\theta/d\lambda$ . The latter are used to obtain the geometrical

spreading factor (3.49). An improved numerical scheme (3.58) is used to compute the attenuation factor  $AT(\omega)$ . Again  $A_{INS}(\omega)$  is obtained through (4.10) for the World-Wide Network's long-period instruments. Since all the above-mentioned transfer functions are generated by computer subroutines specially prepared for this purpose, a straightforward division of the type (5.4) gives rise to the equalized source spectrums.

#### 6.4. Spectral Radiation Patterns and Source Parameters

The input P-wave signals and the output equalized spectrums, arranged according to the azimuth angles of their recording stations, are presented in Figure 6.4. The P waves were originally recorded by instruments of different magnifications and drum speed, but have been normalized to the same peak-to-peak amplitude and time scale, thus permitting a close comparison of the waveforms. High similarity among the P waves is again observed, and appears to be even more pronounced than that in the case of the Banda Sea earthquake discussed in the previous chapter. No clear change in waveforms can be recognized as the azimuth varies. When epicentral distances are larger than  $80^\circ$ , the apparent period of the P-wave signals becomes lengthened. This dispersive property, as a consequence of wave attenuation, will be used to deduce the Q-depth structure in the following chapter. There is a small but distinct arrival occurring about 10 sec. after the onset of almost every observed P wave. The same feature, although less pronounced, was also found in the case of the Banda Sea deep earthquake. Since the times between the onset

of P and the onset of this later arrival are roughly constant over all distances, it suggests that this later event may relate in some way to the stopping phase commonly observed in model experiments (Savage, 1965a and b; Savage and Hasegawa, 1965). Except for a few stations (e.g., SBA, BLA), the normalized spectrums  $A(\omega)$  have essentially the same general form. The dc component of the spectrums reduced to a very low level as compared to the results of the last chapter. On the one hand this may be attributed to the high signal-to-noise ratio of the observed P waveforms, on the other hand, this indicates a satisfactory isolation of the wave signals. Based on the equalized spectrums  $A_o(\omega)$ , radiation patterns were drawn for different wave periods, and they are presented in Figure 6.5. Notice the method of presentation in this figure. A circle is used to indicate the zero radiation, and the source displacements are plotted about it: outward for dilatations and inward for compressions.

Theoretical patterns were then calculated for various combinations of angles of strike, dip, and slip. The solution-seeking process was similar to that described in section 5.3.4. A total of more than 3000 calculated results were scanned. The promising fits were plotted to permit better comparison. The resulting fitted model (model A) had  $\lambda = 270^\circ$ ,  $\delta = 46^\circ$  and strike azimuth  $170^\circ$ . A second set of parameters (model B) also gave reasonably good fit to the empirical patterns with  $\lambda = 252^\circ$ ,  $\delta = 45^\circ$  and strike azimuth  $135^\circ$ . It is interesting to point out, as will be seen later, that model A and model B can be identified to constitute the set of orthogonal circles resulting from the fault-plane-solution method.

In Figure 6.6, we have plotted superimposed patterns:

model A and the empirical result on the left, model B and the empirical result in the middle, and model A and model B on the right. The far stations ( $\Delta > 93^\circ$ ) are marked by arrows. No solution was found which can simultaneously fit the data of both the far stations and the other stations. Either the fit to the far stations would predict much smaller amplitudes for the rest of the stations, or the fit to the rest of the stations would predict much larger amplitudes for the far stations. Since the Q structure at the lower mantle is not yet well-known, and the effect of diffraction by the core is not well understood, we therefore have put little weight on the far stations in the process of searching a model of a good fit.

Both model A and model B show a consistent result that the predicted amplitudes are much larger than those observed in the far stations. In our method of body wave equalization, this strongly suggests an insufficient compensation for the loss in a portion of the wave path. Since a ray reaching a farther station penetrates deeper into the mantle, the above observation leads directly to a hypothesis either that the Q of the lower mantle decreases toward the mantle-core boundary, or that the shadow of the earth's core begins as early as  $93^\circ$  for long-period waves. A more detailed investigation along this line will be given in the next chapter. Here we shall concentrate on exploring more the earthquake source. In Figure 6.7, we present the radiation patterns calculated for model A at different take-off angles in order to show its three-dimensional configuration. Shown here is only the lower half ( $90^\circ \leq \theta \leq 180^\circ$ ) of the radiation pattern, from which the upper half is obtainable by virtue of the

property that P-wave pattern possesses a center of symmetry.

We shall demonstrate a check on the resulting radiation pattern by first noting the following:

1) At large epicentral distances, the incident angle of pP wave at the point of free surface reflection is small ( $\theta_0 \leq 20^\circ$ ).

The calculated crustal transfer function for small incident angles for various crustal structures (Wu and Hannon, 1965) shows that within the long-period spectral window the reflected amplitude is  $|\Gamma_r| \approx 0.9$ , and the phase shift is a slowly varying function of frequency.

2) The take-off angles of P and pP waves recorded at a station of large epicentral distance satisfy approximately the relation  $\theta_P + \theta_{pP} \approx 180^\circ$ .

Our resulting radiation pattern, being practically symmetrical with respect to the plane  $\theta = 90^\circ$ , would therefore predict almost identical P and pP waves observed at a station of large epicentral distance for all azimuthal angles. This is verified by observations presented in Figure 6.8, where epicentral distance and azimuthal angle are shown at the left for each recording station. These waveforms are directly traced down from original seismograms. Except the phase reversal of the pP waves due to the surface reflection (Ingram and Hodgson, 1956), the waveforms and the amplitudes of the juxtaposing P and pP waves for each record are indeed remarkably similar.

### 6.5. Results from First Motion

The first-motion data are summarized in the last two columns of Table 6.1. A total of 107 observations were made on P waves, of which there are 68 direct P waves, 10 PKP waves, and 29 pP waves. They are plotted in Figure 6.9 by the use of appropriate tables of extended distances (Hodgson and Storey, 1953; Hodgson and Allen, 1954a,b). Phase reversal of pP waves on reflection at a free surface has also been taken into account (Ingram and Hodgson, 1956). The only ambiguity in the first-motion data occurs at BOG (No. 14), where the three-component records of the P event in concern do not yield consistent longitudinal wave motion, probably due to the proximity of the station to one of the nodal lines.

Despite the large number of first-motion observations, no definite pair of orthogonal circles can be drawn such as to yield a fault-plane solution with reasonable certainty. However, a few possible solutions are listed in Table 6.3, showing rough bounds of the parameters in concern. The corresponding fault-plane circles are shown in Figure 6.9.

The weakness of the fault-plane-solution in this particular case becomes clear in view of the results presented in the last section. We find in Figure 6.7 the resulting radiation pattern does not radiate compressional P motions inside the cone defined by  $\theta > 132^\circ$ . In other words, no nodal line would appear in epicentral distances  $\Delta > 44^\circ$ , which is nevertheless the region in which the majority of our P-wave data fall. Since the applicability of fault-

plane-solution method requires the distribution of the first-motion data around the nodal line, the lack of this distribution of our data explains our failure to obtain a fault-plane-solution with reasonable certainty. However, the method of body-wave-equalization, using amplitude information in addition to phase polarity, can generally produce a solution of the source when the fault-plane-solution method cannot.

The first-motion data of S waves are shown in Figure 6.10. They admit no solution for single-couple source model. Yet they are not inconsistent with the fault-plane solution of P waves for a double-couple source. To see this, we put  $\lambda = 270^\circ$ , and  $\delta = 45^\circ$  into the S-wave radiation pattern for a double couple and find that except at the immediate neighborhood of the epicenter, all S waves should have positive sign. In Figure 6.10, we find the S-wave data do not violate this condition within experimental error.

## 6.6 Source Mechanism

Based on the results of the previous sections, a displacement dislocation (or the equivalent double couple) appears to be an acceptable source model for the Brazil deep earthquake in concern. The single couple source model has been rejected on account of the distribution of S-wave first motions. The presence of both compressional and dilatational P-wave initial motions has ruled out the possibility of a volume-contraction source. Figure 6.11 presents the strain records of the Brazil deep earthquake and of the two preceding earthquakes studied by Benioff (1963), all written by the

same instrument at Ñaña. The geometrical relationships between epicenter and the Ñaña recording site are given in Table 6.4. First we notice that the waveforms of the three events are almost identical. Benioff's suggestion of a volume-contraction source for the Peruvian earthquakes is chiefly based on the similarity between the waveforms on the strain records and that calculated theoretically for a buried vertical point force. His explanation is supported by an indirect evidence that no compressional first motion was observed in the Peruvian earthquakes he studied. This indirect evidence should not be overemphasized. Referring to the theoretical radiation patterns (Figure 6.7) and the first-motion observations (Figure 6.9) of the Brazil shock, it is easily seen that the compressional P motions radiated from a  $45^{\circ}$  dip-slip fault would confine their distribution to a small region adjacent to the epicenter. It is therefore not unlikely that, due to a thin distribution of recording stations near the epicenter, only dilatational P-wave first motions were observed. Guided by this consideration, a search on the first motions recorded at near stations of these Peruvian earthquakes was conducted. The findings confirm the suspected existence of both the compressional and the dilatational P-wave first motions. Further, a review of the published results of the Fault-Plane Project by the Dominion Observatory shows that a double couple source can generally explain the observed P-wave first motion data from deep earthquakes. Therefore it is concluded that the mathematically equivalent dynamic displacement dislocation source is a tenable physical model adequate for all focal depths.

In the following, we shall calculate some physical quantities pertinent to the adopted source model. Figure 6.12 is a superimposed plot of the equalized source spectrums, all normalized to their values of 0.3 cps. to permit a statistical study on their mean properties. Assuming as before the source time function to be a build-up step (e.g., (5.5)), we compute the source spectrums for different time constant  $\tau$  and find that a reasonable fit can be obtained with  $\tau$  being about 15 sec. The time constant so obtained is merely a rough indication of the average rapidity and duration of the source excitation. The equalized amplitude of the Banda Sea deep shock is 1/3 of that of the Brazil deep shock and its  $\tau$  is about 3 to 5 sec., thus suggesting that  $\tau$  increases with the strength of a seismic source. In other words,  $\tau$  for a small earth tremor can be as short as a fraction of a second. Consequently the source duration is very short and the spectral contents of the observed pulse are mainly short periods. On the other hand, for a big earthquake  $\tau$  can be as long as a minute, producing long-period body waves. The latter was demonstrated by the Alaskan earthquake of March 28, 1964. Its P waves have their first oscillation one to two minutes long.

The source dimensions and energy release can be calculated by the use of the previous results (2.50) and (2.81). Assume that at the focal level

$$\alpha = 10.15 \text{ km/sec}$$

$$\beta = 5.61 \text{ km/sec}$$

$$\lambda = 16.02 \times 10^{11} \text{ dyne/cm}^2$$

$$\mu = 12.94 \times 10^{11} \text{ dyne/cm}^2$$

$$L_o/d = 10^{-3}$$

With the radiation pattern accounted for, the average equalized spectrum at  $T = 30$  sec. is 2.1 m-sec. By (2.50) we find

$$L_o ds = 0.68 \text{ km}^3$$

Then (2.81) gives

$$E = 2.56 \times 10^{23} \text{ ergs}$$

If  $L_o = 1.5 \text{ m}$ , then  $ds = 455 \text{ km}^2$ , or an area of  $15 \text{ km} \times 30 \text{ km}$ .

Chapter 7

ATTENUATION OF BODY WAVES AND THE Q STRUCTURE  
OF THE MANTLE

7.1. Introduction

The attenuation of seismic waves is a subject of much current interest. Its bearing on the constitution, equation of state, and temperature field of the earth's interior is important. Yet it is difficult to study because usually it needs to invoke the results of many not yet well-understood geophysical problems such as the source mechanism, wave scattering, and geometrical spreading of the wavefront, etc. The classical approach is to measure the absolute spatial decay rate of wave amplitudes in the time domain. Being subjected to the above complications, the interpretation of the results has usually been difficult.

Recently, techniques have been developed to avoid these complications. An analysis on the amplitude of surface waves successively passing a station would result in attenuation data free from the effects of source, instrument, local geology, and geometrical spreading. A theory has been advanced (Anderson and Archambeau, 1964; Anderson et al., 1965) permitting an inversion of the surface-wave attenuation data for a Q-depth function. Another approach is to study the spectral ratios of core phases (ScS and sScS) from deep-focus earthquakes recorded at near normal incidence (Anderson and Kovach, 1963; Steinhart et al., 1964; and Kovach and Anderson, 1964). The surface-wave method is most sensitive in the upper mantle,

while the core-phase method yields the average  $Q$  of the mantle.

Aimed to study the more detailed  $Q$ -structure in the deeper part of the mantle, the present method employs the notion of spectral ratios and applies it to a large number of P, S, and pP waves. This method assumes only that the relative spectrum at the source is isotropic and that the attenuation coefficient is a linear function of frequency. The logarithm of the spectral ratio of two body-wave phases, when instrumental and crustal effects are accounted for, will then be a linear function of frequency. Its slope, termed as differential attenuation can be written as  $\pi \left[ \int_j ds/Qv - \int_i ds/Qv \right]$ , where the intrinsic attenuation  $Q$  and the body-wave velocity  $v$  are functions of the radial variable and the integration is along the ray.

The differential attenuation is determined from the deep Brazil shock of November 9, 1963, between  $15^\circ$  and  $105^\circ$  and compared with theoretical curves calculated from surface-wave  $Q$  models. The results are consistent with the idea of a low  $Q$  upper mantle. The observed differential attenuation drops rapidly toward the body-wave shadow boundary, suggesting that  $Q$  decreases toward the core-mantle boundary.

The method, data analysis, and the implications of the findings of the present approach are detailed in the following sections.

## 7.2. Method of the Spectral Ratio

By the method of body-wave equalization presented in Chapter 4, an observed body-wave amplitude,  $A(\omega)$ , can be expressed as a product of the source function,  $A_0(\omega; \theta, \phi)$ , with a number of transfer functions

each for an appropriate portion of the transmitting medium. By (4.4) and (4.6), a teleseismic P wave can be written as

$$A(\omega) = A_o(\omega; \theta, \phi) A_{INS}(\omega) A_{CR}(\omega) A_{MC}(\omega) \quad (7.1)$$

For an earthquake of magnitude less than 7 and wave periods longer than a few seconds, there is evidence (Teng and Ben-Menahem, 1965; Chapters 5 and 6; Kasahara, 1964) indicating that the source function can be factored into a spatial part and a temporal part

$$A_o(\omega; \theta, \phi) = A_s(\theta, \phi) A_t(\omega) \quad (7.2)$$

Physically this implies that the same time function is radiated by the source regardless of direction.

If we take the ratio of two P-wave spectrums from an earthquake observed at stations  $i$  and  $j$ , the common factor  $A_t(\omega)$  drops out and it is easily shown by (3.51), (3.52), (3.53), and (4.12) that

$$\exp [R(f)] = c_1 \exp [f(t_j^* - t_i^*)] \quad (7.3)$$

where

$$R(f) \equiv \ln \left[ \frac{A_{CR_j}(\omega) A_{INS_j}(\omega) A_i(\omega)}{A_{CR_i}(\omega) A_{INS_i}(\omega) A_j(\omega)} \right] \quad (7.4)$$

$$c_1 \equiv \frac{G_i A_s(\theta_i, \phi_i)}{G_j A_s(\theta_j, \phi_j)} \quad (7.5)$$

$$t_j^* - t_i^* \equiv \pi \left[ \int_j \frac{ds}{Q_a a} - \int_i \frac{ds}{Q_a a} \right] \quad (7.6)$$

$$f = \frac{\omega}{2\pi}$$

On the left-hand side of (7.3),  $R(f)$  is a known numerical function;  $A_i(\omega)$  and  $A_j(\omega)$  are amplitude spectrums of the observed signals; the calculation of the crustal transfer function  $A_{CR}(\omega)$ , and the instrumental response,  $A_{INS}(\omega)$ , are detailed in sections 3.4 and 4.2, they are also known functions when crustal structure at the recording site, the phase velocity of the concerned signal, and the instrumental characteristics are given. It is convenient here to call  $R(f)$  the reduced spectral ratio.  $c_1$  is some unknown constant of frequency which, as will be seen, is not important in our analysis.

From (7.3), it follows that

$$R(f) = \ln c_1 + (t_j^* - t_i^*) f \quad (7.7)$$

This simple result shows that the reduced spectral ratio is a linear function of frequency. Its slope,  $\delta A = (t_j^* - t_i^*)$ , properly termed differential attenuation, contains all the information concerning the difference of wave attenuation along two different rays. The constant term,  $\ln c_1$  does not concern us in the present analysis and will be ignored from this point on. Clearly the determination of differential attenuation from empirical data of reduced spectral ratio requires no knowledge of the seismic source and the geometric spreading of the

wavefront.

In practice, one calculates the reduced spectral ratio according to (7.4) and fits the resulting numerical function by least squares to a straight line. The coefficient of the linear term of the resulting fit gives the differential attenuation which, in light of (7.6), has the dimension of time and may be regarded as the difference of the imaginary parts of the travel times between the two signals. The fitting process is meant to minimize statistically the experimental noises introduced by microseisms, digitization, and numerical Fourier-transformation of the signals.

For a number of observations made on an earthquake, the resulting differential attenuation calculated with respect to a referential observation gives an empirical function of epicentral distance. One therefore obtains a curve which is a concise summary of the energy dissipation mechanism of the earth's interior as experienced by body-wave signals.

To extract useful Q-information from the curve of differential attenuation, one makes use of the definition in (7.6). The integrals on the right-hand side can be computed numerically for given velocity and Q-structures. Detailed numerical scheme for this purpose is given in Appendix 3 and the corresponding computer program is written in Fortran for an IBM 7094. To date, the velocity structure is relatively well determined, but the Q-structure is not well known except in the upper mantle from the result of surface waves (Anderson and Archambeau, 1964; Anderson et al., 1965). Therefore, by adopt-

ing a velocity structure, one starts the computation of differential attenuation with the surface-wave  $Q$  model. By successively perturbing the input  $Q$  model in the direction where the computed results gradually approach the empirical values, information about the attenuation collected by body-waves is incorporated into an improved  $Q$  structure, particularly in the lower mantle.

### 7.3. Data Analysis -- Spectral Ratios of $P/P$ , $pP/P$ , $S/P$

$P$ ,  $pP$  and  $S$  waves used in the present analysis are from the same Brazil deep shock studied in Chapter 6. The method of spectral ratio requires no knowledge on the absolute amplitude of a wave signal, however, it imposes a more strict requirement on the accuracy of the recorded waveform. The outcome of such an analysis would be greatly obscured if one or more of the following features appear significantly in an analyzed signal: 1) recording instrument under-damped; 2) microseismic, instrumental, or man-made noises; 3) signals not properly separated from the neighboring events; 4) the crustal structure of the recording site unclear.

With precautions against those features, a total of 27  $P$  waves, 8  $pP$  waves and 8  $S$  waves were entered into the spectral ratio analysis. Relevant information about  $P$  waves have been presented in Table 6.1. The  $P$  waveforms have been presented in Figure 6.4, and the geographical distribution of the recording stations, in Figure 7.1. The  $pP$  waveforms have been shown in Figure 6.8, and  $S$  waveforms are shown in Figure 7.2. In Table 7.1, some relevant calculations on  $pP$  and  $S$  waves are given. It is seen from the back azimuth

angle that the S waves recorded on the NS component of the selected records are indeed SH waves. These signals were digitized at a rate of one point per second. A time window of 60 seconds was applied to pP waves the same way as it was applied to P waves in section 6.2. It is rather difficult to determine the duration of the S waves. Different window lengths (given in Table 7.1) were used so as to embrace the essential portion of the S energy. Amplitude spectrums of the signals were obtained by the conventional technique of numerical Fourier transformation. The reduced spectral ratios,  $R(f)$ , were calculated routinely according to (7.4) where crustal structures of the recording stations are given in Table 6.2. In the case of pP/P, an additional correction on free surface reflection is added to (7.4). Since we use instruments of identical frequency response, the ratio  $A_{INS_j}(\omega)/A_{INS_i}(\omega)$  is not a function of  $\omega$  and is therefore dropped out of the analysis. In the case of P/P, generally a base station (e.g., the jth station) was chosen, with respect to which the reduced spectral ratio of the ith station was calculated where i ranges over all stations. In cases of pP/P and S/P, reduced spectral ratios were formed within each station. The calculation of the spectral ratio was carried over the period range  $100 \leq T \leq 5$  sec. The purpose of extending the use of the spectral information to a shorter period is that short-period waves are more sensitive to the attenuation mechanism. Of course the use of wave signals from instruments of even shorter periods ( $T \leq 2$  sec.) can be dangerous, simply because the uncertainty of the crustal transfer

function at these short periods would generally be too big to permit any meaningful outcome. Even in the present period range between 5 and 10 seconds, the spectrums generally possess small minimums and maximums due to various reasons such as noises, signal truncations, and small uncertainty of the crustal structures, etc. Upon forming spectral ratios, these minimums and maximums magnify themselves in giving spikes in either direction. This is undesirable in our analysis not only because the resulting functions are difficult to interpret, but because the odd functional behavior is not genuine and is introduced by numerically taking the ratio of two empirical functions. Since the primary concern of the present attenuation study is to detect a gentle trend of decrease of spectral components toward the shorter-period end, it appears appropriate to avoid the above difficulty by passing a moving average through both the wave spectrums and the reduced spectral ratios before applying a least squares fitting. A moving average of window width 0.02 cps. was used. The resulting empirical data,  $R(f)$ , was fitted by least squares with a straight line and the differential attenuation,  $\delta A$ , was obtained according to (7.7). By (3.53) we have

$$\delta A_{P/P} = t_j^* - t_i^* \equiv \pi \left[ \int_j \frac{ds}{Q_a^a} - \int_i \frac{ds}{Q_a^a} \right] \quad (7.8)$$

Similarly, in cases of  $pP/P$  and  $S/P$ , we have

$$\delta A_{pP/P} = t_P^* - t_{pP}^* \equiv \pi \left[ \int_P \frac{ds}{Q_a^a} - \int_{pP} \frac{ds}{Q_a^a} \right] \quad (7.9)$$

$$\delta A_{S/P} = t_P^* - t_S^* \equiv \pi \left[ \int_P \frac{ds}{Q_a^\alpha} - \int_S \frac{ds}{Q_\beta^\beta} \right] \quad (7.10)$$

$\delta A_{P/P}$ , computed with respect to two stations SCP (No. 69) and KTG (No. 38), are presented in Figure 7.3. In the figure, the horizontal line  $\delta A = 0$  is drawn through station No. 69. In view of (7.8), a data point below this line indicates that the P wave observed at that station had suffered stronger attenuation than the P wave observed at station No. 69, and vice versa. Similar data of  $\delta A_{pP/P}$  and of  $\delta A_{S/P}$  are presented in Figure 7.4, in which a data point below the line  $\delta A = 0$  indicates that the pP (or S) wave had suffered stronger attenuation than the P wave observed at the same station. We shall discuss in the following sections the implications of the  $\delta A_{P/P}$  and the  $\delta A_{pP/P}$  data on the Q structure of the upper and lower mantle respectively.

the  $\delta A_{S/P}$  data show rather too large a scatter to permit meaningful interpretation. In Figure 7.4b, the line  $\delta A = 0$  corresponds to the case  $Q_\beta = \sqrt{3} Q_a$  if Poisson's relation is assumed throughout the mantle. Curve 1 corresponds to the case  $\bar{Q}_a = \bar{Q}_\beta = 600$  and curve 2 to the case  $\frac{4}{9} \bar{Q}_a = \bar{Q}_\beta = 600$ . Here a bar over Q symbolizes that a homogeneous Q mantle is assumed. The failure of  $\delta A_{S/P}$  data to comply with any of these cases indicates that a careful reexamination of the isolation of S energy from the seismogram is necessary, or that one of our basic assumptions that the source time function is the same for both P and S waves is doubtful.

#### 7.4. $\delta A_{pP/P}$ and the Average $Q_\alpha$ in the Upper Mantle

In Figure 7.4a, the distribution of  $\delta A_{pP/P}$  data below the line  $\delta A = 0$  indicates that a pP wave generally suffers greater attenuation than a direct P wave observed at the same station. As pP waves penetrate the upper mantle two more times than P waves do, it will be shown later that our data are consistent with the notion of a low  $Q$  upper mantle resulting from the studies on surface waves (Anderson and Archambeau, 1964; Anderson, et al., 1965) and on multiple ScS and sScS phases (Anderson and Kovach, 1964; Kovach and Anderson, 1964). We do not consider the  $\delta A_{pP/P}$  data good enough to permit a determination of a  $Q_\alpha$ -depth structure in the upper mantle, but the data at least offers enough insight by which an average  $Q_\alpha$  for the upper mantle can be deduced.

First we note from Figure 7.5 that at large epicentral distances, as most of our data are, the path of a P wave, fdb, and that of a pP wave, faf'd'b, follow closely to each other along most of the wave paths. Let  $f'$  be chosen so that P-wave travel times along the two paths, fdb and f'd'b, be the same. If the mantle does not depart greatly from homogeneity in terms of  $Q_\alpha$ , it appears reasonable to assume that P-wave attenuations along these two paths are also equal. Consequently, on breaking the second integral on the right-hand side of (7.9) into two parts, we find

$$\begin{aligned} \delta A_{pP/P} &= \pi \left[ \int_{fb} \frac{ds}{Q_a} - \int_{f'b} \frac{ds}{Q_a} - \int_{faf'} \frac{ds}{Q_a} \right] \\ &= -\pi \int_{faf'} \frac{ds}{Q_a} \end{aligned} \quad (7.11)$$

To seek an average  $Q_a$  between the free surface and the focal level, we assume  $Q_a$  to be constant along the path  $faf'$ . This leads to

$$\delta A_{pP/P} = -\frac{\pi}{\bar{Q}_a} \int_{faf'} \frac{ds}{a} \quad (7.12)$$

where  $\bar{Q}_a$  denotes the average  $Q_a$  along the path. Since the integral in (7.12) is exactly equal to the difference of travel times between  $pP$  and  $P$ , we finally obtain

$$\begin{aligned} \bar{Q}_a &= -\pi(t_{pP} - t_P) / \delta A_{pP/P} \\ &= -\pi(t_{pP} - t_P) / (t_{pP}^* - t_P^*) \end{aligned} \quad (7.13)$$

(7.13) therefore provides a method by which the average  $Q$  above the focal level can be estimated by use of a single seismogram. Travel times  $t_{pP} - t_P$  were measured off the seismograms, using the data in Figure 7.4a we have computed the values of  $\bar{Q}_a$  which are presented in Table 7.2. Here each value of  $\bar{Q}_a$  is resulted from an independent experiment, an equally weighted average over all stations gives  $\bar{Q}_a = 105$ . More properly, this  $\bar{Q}_a$  gives the average  $Q_a$  for the upper 430 km of the mantle. Since it is easy to find (Figure 7.5)

for  $f = 550$  km deep, and under the condition on travel times  $t_{f'b} = t_{fb}$  that  $f'$  is equivalent to a depth of 310 km. Furthermore, the possibility of the existence of a low- $Q$  zone near the core-mantle boundary would result in a greater attenuation of the  $P$  wave along the path  $fb$  than along the path  $f'b$ . The assumption of their equality tends only to increase the value of the resulting  $\bar{Q}_\alpha$ . In other words, we have obtained an upper bound.

There is no directly measured  $Q_\alpha$  values in the upper mantle with which our result can compare. However, from the studies of the core phases,  $Q_\beta$  in the upper 600 km of the mantle was found to be 160 as a maximum by Steinhart et al. (1964), and 200 by Kovach and Anderson (1964). From free oscillation and surface wave data, Anderson et al. (1965) gave a  $Q_\beta$  structure which has an average of about 164 for the upper 430 km.

The major uncertainty of our analysis seems to come from the crustal reflection coefficient applied to each  $pP$  signal. We regard the above analysis more of the nature of a feasibility study than providing us with definite  $Q_\alpha$  structure. The result is far from final, yet the method appears to yield consistent information. A more extensive data analysis is needed before a better conclusion can be drawn.

#### 7.5. $\delta A_{P/P}$ and $Q_\alpha$ in the Lower Mantle

Several features of special interest emerge from the resulting  $\delta A_{P/P}$  data (Figure 7.3). A depression seems to exist between  $30$  and  $50^\circ$ . This, as will be seen, can be explained by the presence of a low- $Q$  layer and a low-velocity layer in the upper mantle. More

strikingly, we find a rapid decrease of  $\delta A_{P/P}$  beyond a distance of about  $85^\circ$ . Note that P waves from a 550 km deep shock arriving at a distance of  $85^\circ$  have their deepest point at a distance of about 3643 km from the earth's center, or about 170 km above the commonly held core-mantle boundary (Jeffrey, 1962, p. 98). Therefore, the observed rapid decrease of  $\delta A_{P/P}$  is displayed by the P waves which may have already sensed the presence of the earth's core. In the derivation of the  $\delta A_{P/P}$  data, we did not account for this possible diffraction effect. Without clarification, this certainly would make the interpretation of the resulting data untenable. To clarify this point, we shall digress to a brief discussion on the diffraction effect by the earth's core. Chiefly we intend to set forth an argument to show that the diffraction effect before the geometrical shadow boundary would at worst make our resulting Q values an upper bound.

From the results of Nagase (3.64) and of Scholte (3.65), it is seen that, for field points occurring before the geometrical shadow boundary ( $\delta_0 < 0$ ), the amplitude increases exponentially as  $|\delta|$  increases. This indicates the gradual exposure to direct radiation. Amplitudes of shorter-period waves rise even faster than those of longer-period ones, and for  $\omega$  approaching  $\infty$  as a limit, the amplitude rises immediately, giving rise to a well-defined line for the geometrical shadow boundary. A similar but more rigorous result from a detailed analysis by Nussenzveig (1965) shows that, for wavelength not too small as compared with the radius of the diffracting sphere, the transition from the lit zone to the shadow zone is rather

gradual. By defining the shadow boundary by the condition that the wave amplitude reduces to its half value, Nussenzveig was able to deduce a relation giving the effective radius,  $r_{\text{eff}}$ , of the diffracting sphere to the actual radius

$$r_{\text{eff}} = r_c + 1.36 \left( \frac{v}{\omega r_c} \right)^{2/3} r_c \quad (7.14)$$

for a plane wave of frequency  $\omega$  and velocity  $v$ . (7.14) is valid inside the Fresnel region defined by

$$|\delta_0| \ll \left( \frac{\omega r_c}{v} \right)^{-1/3}$$

$$\left( \frac{\omega r_c}{v} \right)^{-1/3} \leq r \cos \delta \leq \left( \frac{\omega r_c}{v} \right)^{1/3}$$

Clearly, this result predicts that longer waves would sense a bigger core. Consequently, the so-defined shadow boundary occurs in successively shorter distances as the wave periods become progressively longer. This is shown schematically in Figure 7.6, which is drawn to approximate the real earth case with  $r_c = 0.548 r_0 = 3473$  km,  $v = 13.6$  km/sec. Each curve essentially gives a Fresnel diffraction pattern. Let the geometrical shadow boundary be at  $\delta_g = 102^\circ$ , the effective shadow boundaries are found for 3-second, 10-second, and 100-second waves, to be at  $98^\circ$ ,  $93.5^\circ$ , and  $77^\circ$  respectively. Therefore, a signal observed before  $\delta_g$  in the Fresnel region would suffer a greater loss from diffraction in long-period components than in

short-period components. This is contrary to the wave attenuation process due to the earth's anelasticity, where short-period waves always attenuate faster. Consequently, it is plausible that the rapid decrease of the  $\delta A_{P/P}$  data observed beyond  $85^\circ$  is principally a manifestation of the earth's anelasticity; and the effect of core diffraction, particularly in the lower mantle, would at worst make an upper bound of the measured  $Q$  values.

Returning from the above digression, we shall now examine what properties the  $Q_\alpha$ -depth structure must have in order to explain the observed differential attenuation data. A subroutine described in Appendix 3 was conveniently adopted for this purpose. By feeding into the computer program a  $Q$  structure and a velocity structure, differential attenuation (7.8) was computed for all epicentral distances and the result was compared to the observed values. Since the velocity structure is much better known than the  $Q$  structure, we have adopted the CIT 11 C velocity model and perturbed the  $Q$ -model, using as a starting point models described by Anderson et al. (1965). After a number of trials, a model was evolved which seems to explain the observations. The results are presented in Figure 7.7. The crosses and circles are observed values copied from Figure 7.3. Curve 1 is computed for the  $Q_\alpha$  MM8 model, curve 2 is for the  $Q_\beta$  MM8 model, curve 3 is for a trial model, and curve 4 is for the present  $Q_\alpha$  model. Their corresponding numerical values are presented in Figure 7.8.

The major feature of the present  $Q_\alpha$  model is that it has in the upper mantle a low- $Q$  region which extends to a depth of about

1000 km below the earth's surface. More importantly, the  $Q_a$ , followed by a high-Q lower mantle, decreases rapidly toward the core-mantle boundary. The implication of this low-Q region near the core-mantle boundary is evident. In fact, it was recognized long ago and has been supported by increasing evidences from recent systematic observations (Tuve et al., 1964; Sacks, 1965)\* that amplitudes of short-period body waves decrease sharply beyond  $90^\circ$ , or 5 to  $10^\circ$  before the commonly held shadow boundary. Our findings in section 6.4 and Figure 6.6 also show that a high-Q region in the lower mantle, particularly near its base, cannot account for the loss of amplitudes for the far stations. All these appear to be interpretable by a low-Q region at the bottom 200 km of the mantle. Some support of this interpretation can be drawn from a recent model experiment performed on low-melting point alloy (Mizutani and Kanamori, 1964). By varying the temperature,  $Q_a$  was measured from solid phase to liquid phase and it was found that  $Q_a$  dropped one order of magnitude upon melting. Although on passing from the solid mantle to the liquid outer core in the real earth case, the change of pressure and the heterogeneity of chemical constitution etc. may complicate the physical picture, the principal dependence of  $Q$  on the physical phase may still hold. Better understanding of this lower-mantle low-Q region awaits more data in addition to the differential attenuation solely based on P/P spectral ratios.

---

\* Although the authors of these papers tried to explain their observation by core diffraction.

REFERENCES

- Anderson, D., and C. B. Archambeau, The anelasticity of the earth, J. Geophys. Res., 69, 2071 - 2084, 1964.
- Anderson, D. L., A. Ben-Menahem, and C. B. Archambeau, Attenuation of seismic energy in the upper mantle, J. Geophys. Res., 70, 1441-1448, 1965.
- Anderson, D. L., and R. L. Kovach, Attenuation in the mantle and rigidity of the core from multiply reflected core phases, Proc. Nat. Acad. Sci. U. S., 51, 168-172, 1964.
- Archambeau, C. B., Elastodynamic source theory, Ph.D. Thesis, California Institute of Technology, 1964.
- Banaugh, R. P., Application of integral representations of displacement potentials in elastodynamics, Northrop Ventura Report No. 2953, 1964.
- Båth, M., and H. Benioff, The aftershock sequence of the Kamchatka earthquake of November 4, 1952, Bull. Seismol. Soc. Am., 55, 203-235, 1965.
- Benioff, H., A new vertical seismograph, Bull. Seismol. Soc. Am., 22, 155-169, 1932.
- Benioff, H., Source wave forms of three earthquakes, Bull. Seismol. Soc. Am., 53, 893-903, 1963.
- Ben-Menahem, A., Mode ray duality, Bull. Seismol. Soc. Am., 54, 1315-1321, 1964.
- Ben-Menahem, A., S. W. Smith, and T. L. Teng, A procedure for source studies from spectrums of long-period seismic body waves, Bull. Seismol. Soc. Am., 55, 203-235, 1965.
- Bremmer, H., Terrestrial Radio Waves, Elsevier Publishing Co., Amsterdam, New York, 1949.
- Brune, J. N., Travel times, body waves and normal modes of the earth, Bull. Seismol. Soc. Am., 54, 2099-2128, 1964.
- Bullen, K. E., An Introduction to the Theory of Seismology, Cambridge University Press, 1963.
- Burridge, R., and L. Knopoff, Body force equivalents for seismic dislocations, Bull. Seismol. Soc. Am., 54, 1875-1888, 1964.

- Clebsch, A., Über die Reflection an einer Kugelfläche, J. für Math., 61, 195-262, 1863.
- Cohen, A., Differential Equations, 1933.
- de Hoop, A. T., Representation theorems for the displacement in an elastic solid and their applications to elastodynamic diffraction theory, Ph.D. Thesis, Delft, 1958.
- Espinosa, A. F., G. H. Sutton, and H. J. Miller, S.J., A transient technique for seismograph calibration, Bull. Seismol. Soc. Am., 52, 767-779, 1962.
- Gilbert, F., and G. J. F. MacDonald, Free Oscillations of the earth, 1. Torsional oscillations, J. Geophys. Res., 65, 675-693, 1960.
- Haskell, N. A., The dispersion of surface waves on multi-layered media, Bull. Seismol. Soc. Am., 43, 17-34, 1953.
- Haskell, N. A., Crustal reflection of plane SH waves, J. Geophys. Res., 65, 4147-4150, 1960.
- Haskell, N. A., Crustal reflection of plane P and SV waves, J. Geophys. Res., 67, 4751-4767, 1962.
- Haskell, N. A., Total energy and energy spectral density of elastic wave radiation from propagating faults, Bull. Seismol. Soc. Am., 54, 1811-1841, 1964.
- Hodgson, J. H. and J. F. J. Allen, Tables of extended distances for PKP and PcP, Publ. Dom. Obs. Ottawa, 16, No. 10, 329-348, 1954a.
- Hodgson, J. H. and J. F. J. Allen, Tables of extended distances for PP and pP, Publ. Dom. Obs. Ottawa, 16, No. 11, 351-362, 1954b.
- Hodgson, J. H., and R. S. Storey, Tables extending Byerly's fault-plane techniques to earthquakes of any focal depth, Bull. Seismol. Soc. Am., 43, 49-61, 1953.
- Ingram, R. E. and J. H. Hodgson, Phase change PP and pP on reflection at a free surface, Bull. Seismol. Soc. Am., 46, 203-213, 1956.
- Jeffreys, H., The Earth, 4th ed., Cambridge University Press, 1962.
- Karal, F. C. Jr., and J. B. Keller, Elastic wave propagation in homogeneous and inhomogeneous media, J. Acoust. Soc. Am., 31, 694-705, 1959.

- Kasahara, K., The nature of seismic origins as inferred from seismological and geodetic observations, 1, Bull. Earthquake Res. Inst., Tokyo Univ., 35, 473-532, 1957.
- Keilis-Borok, V. I., The theory of waves due to displacements, Akad. Nauk SSSR Izv. ser. Geofiz., No. 4, 440-448, 1957.
- Keller, J. B. and F. C. Karal Jr., Surface wave excitation and propagation, J. Appl. Phys., 31, 1039-1046, 1960.
- Keller, J. B. and F. C. Karal Jr., Geometric theory of elastic surface-wave excitation and propagation, J. Acoust. Soc. Am., 36, 32-40, 1964.
- Knopoff, L., Diffraction of elastic waves, J. Acoust. Soc. Am., 28, 217-229, 1956.
- Knopoff, L., and F. Gilbert, First motion from seismic sources, Bull. Seismol. Soc. Am., 50, 117-134, 1960.
- Kovach, R. L. and D. L. Anderson, Attenuation of shear waves in the upper and lower mantle, Bull. Seismol. Soc. Am., 54, 1855-1864, 1964.
- Love, A. E. H., A Treatise on the Mathematical Theory of Elasticity, Dover, 1944.
- Luneburg, R. K., The Mathematical Theory of Optics, Lecture Notes, Brown University, 1944.
- Macelwane, G. B. and F. W. Sokon, Theoretical Seismology, Parts I and II, New York: Wiley, 1932 and 1936.
- Maruyama, T., On the force equivalents of dynamical elastic dislocations with reference to the earth mechanism, Bull. Earthquake Res. Inst., Tokyo Univ., 41, 467-486, 1963.
- Maruyama, T., Statistical elastic dislocations in an infinite and semi-infinite medium, Bull. Earthquake Res. Inst., Tokyo Univ., 42, 289-368, 1964.
- Mizutani, H., and H. Kanamori, Variation of elastic wave velocities and attenuative property near the melting temperature, J. Phys. of the Earth, 12, 43-49, 1964.
- Morse, P. M., and H. Feshbach, Methods of Theoretical Physics, McGraw-Hill Book Company, New York, 1953.
- Nagase, M., Diffraction of elastic waves by a spherical surface, J. Phys. Soc. Japan, 11, 279-301, 1956.

- Nussenzveig, H. M., High-frequency scattering by an impenetrable sphere, Annals of Physics, 34, 23-95, 1965.
- Sato, Y., T. Usami, M. Landisman and M. Ewing, Basic study on the oscillation of a sphere, Part V: Propagation of torsional disturbances on a radially heterogeneous sphere, Geophys. J. Roy. Astro. Soc., 8, No. 1, 44-63, 1963.
- Savage, J. C., and H. S. Hasagawa, A two dimensional model study of directivity function, Bull. Seismol. Soc. Am., 55, 22-45, 1965.
- Savage, J. C., The stopping phase on seismograms, Bull. Seismol. Soc. Am., 55, 47-58, 1965.
- Savage, J. C., The effect of rupture velocity upon seismic first motions, Bull. Seismol. Soc. Am., 55, 263-275, 1965.
- Savarensky, E. F., and D. P. Kirnos, Elements of Seismology and Seismometry, Moscow, 1955.
- Scholte, J. G. J., On seismic waves in a spherical earth, Kon. Ned. Meteo. Inst. Publication No. 6S, 1956.
- Steinhart, et al., Carnegie Institution of Washington Yearbook, 62, 286-288, 1964.
- Steketee, J. A., Some geophysical applications of the elasticity theory of dislocation, Can. J. Physics, 36, 1168-1198, 1958.
- Sommerfeld, A. and J. Runge, Anwendung der vektorrechnung auf die grundlagen der geometrischen optik, Ann. Phys., 35, 277-298, 1911.
- Teng, T. L., and A. Ben-Menahem, Mechanism of deep earthquakes from spectrums of isolated body-wave signals: 1 the Banda Sea earthquake of March 21, 1964, J. Geophys. Res., 70, 5157-5170, 1965.
- Thomson, W. T., Transmission of elastic waves through a stratified solid medium, J. App. Phys., 21, 89, 1950.
- Tsuboi, C., Earthquake energy, earthquake volume, aftershock area, and strength of the earth's crust, J. Phys. Earth, 4, 63-66, 1956.
- Tukey, J. W., Equalization and pulse shaping techniques applied to the determination of initial sense of Rayleigh waves, The Need for Fundamental Research in Seismology, Report of the Panel on Seismic Improvement, U.S. Department of State, pp. 60-129, 1959.

- van der Pol, B., and H. Bremmer, The diffraction of electromagnetic waves from an electrical point source round a finitely conducting sphere, with applications to radio telegraphy and the theory of rainbow, Phil. Mag., 24, 825-864, 1937.
- Vvedenskaya, A. V., The determination of displacement field by means of dislocation theory, Akad. Nauk SSSR Izv. ser. Geofiz., No. 3, p. 227, 1956.
- Watson, G. N., The diffraction of electric waves by the earth, Proc. Roy. Soc. (London), 95, 83-99, 1918.
- Wu, F. T., and W. J. Hannon, PP and the crustal structure, Bull. Seismol. Soc. Am., (to be published).

TABLE CAPTIONS

- Table 2.1 - Horizontal Radiation Patterns for the Far Field of Body Waves.
- Table 2.2 - Vertical Radiation Patterns for the Far Field of Body Waves.
- Table 5.1 - Data List and Pertinent Information Concerning the Banda Sea Deep Shock.
- Table 6.1 - Data List and Pertinent Information Concerning the Brazil Deep Shock.
- Table 6.2 - Crustal Structures.
- Table 6.3 - Some Possible Fault-Plane Solutions.
- Table 6.4 - The Space-Time Relationships of the Three Deep Shocks.
- Table 7.1 - Data List of pP and S Waves.
- Table 7.2 - Average  $Q_{\alpha}$  of the Upper Mantle.

Table 2.1

HORIZONTAL RADIATION PATTERNS FOR THE FAR FIELD  
OF BODY WAVES

$$A_s(\phi) = a_0 + a_1 \sin \phi + a_2 \cos \phi + a_3 \sin 2\phi + a_4 \cos 2\phi$$

P Waves

Shear Fault

Tensile Fault

$$a_0 \quad \frac{1}{4} \sin \lambda \sin 2\delta (1 - 3 \cos^2 \theta)$$

$$S_0 + \frac{1}{2} (\cos^2 \delta \cos^2 \theta + \sin^2 \delta \sin^2 \theta)$$

$$a_1 \quad -\frac{1}{2} \sin \lambda \cos 2\delta \sin 2\theta$$

$$-\frac{1}{2} \sin 2\delta \sin 2\theta$$

$$a_2 \quad -\frac{1}{2} \cos \lambda \cos \delta \cos 2\theta$$

0

$$a_3 \quad \frac{1}{2} \cos \lambda \sin \delta \sin^2 \theta$$

0

$$a_4 \quad -\frac{1}{4} \sin \lambda \sin 2\delta \sin^2 \theta$$

$$-\frac{1}{2} \sin^2 \delta \sin^2 \theta$$

Table 2.1 (Continued)

SV Waves

	<u>Shear Fault</u>	<u>Tensile Fault</u>
$a_0$	$\frac{3}{8} (b+1) \sin 2\delta \sin \lambda \sin 2\theta$	$\frac{1}{4} \sin 2\theta (1 - 3 \cos^2 \delta)$
$a_1$	$\sin \lambda [ \sin^2 \theta (b \cos^2 \delta - \sin^2 \delta) - \cos^2 \theta (\cos^2 \delta - b \sin^2 \delta) ]$	$-\frac{1}{2} \cos 2\theta \sin 2\delta$
$a_2$	$-(\cos^2 \theta - b \sin^2 \theta) \cos \delta \cos \lambda$	0
$a_3$	$\frac{1}{4} (b+1) \sin \delta \cos \lambda \sin 2\theta$	0
$a_4$	$-\frac{1}{8} (b+1) \sin 2\delta \sin \lambda \sin 2\theta$	$-\frac{1}{4} \sin 2\theta \sin^2 \delta$

Table 2.1 (Concluded)

SH Waves

	<u>Shear Fault</u>	<u>Tensile Fault</u>
$a_0$	$\frac{1}{2}(b-1)\sin\delta\cos\lambda\sin\theta$	0
$a_1$	$\cos\delta\cos\lambda\cos\theta$	0
$a_2$	$(b\sin^2\delta - \cos^2\delta)\sin\lambda\cos\theta$	$-\frac{1}{2}\sin 2\delta\cos\theta$
$a_3$	$\frac{1}{4}(b+1)\sin 2\delta\sin\lambda\sin\theta$	$\frac{1}{2}\sin^2\delta\sin\theta$
$a_4$	$\frac{1}{2}(b+1)\sin\delta\cos\lambda\sin\theta$	0

Table 2.2

VERTICAL RADIATION PATTERNS FOR THE FAR FIELD  
OF BODY WAVES

$$A_s(\theta) = c_0 + c_1 \sin \theta + c_2 \cos \theta + c_3 \sin 2\theta + c_4 \cos 2\theta$$

$$\Omega_1 = \cos \phi \cos \lambda + \sin \phi \sin \lambda \cos \delta$$

$$\Omega_2 = \cos \phi \cos \lambda \cos \delta + \sin \phi \sin \lambda \cos 2\delta$$

P Waves

Shear Fault

Tensile Fault

$$c_0 \quad \frac{1}{2} \sin \phi \sin \delta \Omega_1 \\ - \frac{1}{4} \sin \lambda \sin 2\delta$$

$$S_0 + \frac{1}{2} - \frac{1}{2} \sin^2 \delta \cos^2 \phi$$

$$c_1 \quad 0$$

$$0$$

$$c_2 \quad 0$$

$$0$$

$$c_3 \quad -\frac{1}{2} \Omega_2$$

$$-\frac{1}{2} \sin 2\delta \sin \theta$$

$$c_4 \quad -\frac{1}{4} \sin \lambda \sin 2\delta \\ - \frac{1}{2} \sin \phi \sin \delta \Omega_1$$

$$\frac{1}{2} - \frac{1}{2} \sin^2 \delta (1 + \sin^2 \phi)$$

Table 2.2 (Continued)

SV Waves

	<u>Shear Fault</u>	<u>Tensile Fault</u>
$c_0$	$\frac{1}{2} (b - 1) [\cos \delta \cos \lambda \cos \phi + \sin \lambda \sin \phi]$	0
$c_1$	0	0
$c_2$	0	0
$c_3$	$\frac{1}{4} (b + 1) [\sin 2\delta \sin \lambda + 2 \sin \delta \sin \phi \Omega_1]$	$\frac{1}{4} [(1 - 3 \cos^2 \delta) - \sin^2 \delta \cos 2\theta]$
$c_4$	$-\frac{1}{2} (b + 1) \Omega_2$	$-\frac{1}{2} \sin \theta \sin 2\delta$

Table 2.2 (Concluded)

SH Waves

	<u>Shear Fault</u>	<u>Tensile Fault</u>
$c_0$	0	0
$c_1$	$\frac{1}{4} (b+1) \sin 2\delta \sin \lambda \sin 2\phi$ $+ (b \cos^2 \phi - \sin^2 \phi) \sin \delta \sin \lambda$	$-\frac{1}{2} \sin^2 \delta \sin 2\theta$
$c_2$	$\cos \delta \cos \lambda \sin \phi$ $- (\cos^2 \delta - b \sin^2 \delta) \sin \lambda \cos \phi$	$\frac{1}{2} \sin 2\delta \cos \theta$
$c_3$	0	0
$c_4$	0	0

Table 5.1  
DATA LIST AND PERTINENT INFORMATION CONCERNING THE BANDA SEA DEEP SHOCK

Station No.	Code	$\lambda$ , deg.	Azimuth, deg.	Back Azimuth, deg.	$\theta_h^*$	$\theta_o^*$	P First Motions	SV First Motions
1	AAE†	90.14	279.0	96.4	155.5	18.5	+	-
2	ADE†	30.13	162.1	338.2	131.5	37.5	-	-
3	AFI†	59.71	102.3	270.7	144.5	27.6	-	-?
4	ANP†	31.96	349.1	168.0	133.0	36.5	-	-?
5	BAG†	23.79	342.4	161.7	128.4	40.0	+	-
6	BUL†	96.48	248.9	99.2	157.5	17.4	-	+
7	COL†	93.33	25.2	262.1	157.2	17.8	+	-
8	CTA†	22.42	129.1	304.9	127.0	40.8	-	+
9	GUA†	26.04	40.3	221.3	129.9	38.3	-	-
10	HKC†	31.53	335.2	153.2	132.4	36.9	-	-?
11	HON†	77.56	66.6	258.1	152.4	22.3	-	-
12	HNR†	31.88	97.5	273.0	132.9	25.4	-	-
13	IST†	100.89	310.5	89.0			-	+
14	KEV†	99.74	339.7	82.0			-	-?
15	KIP†	77.60	66.5	257.9			-	-
16	MAN†	21.99	342.1	161.6	126.9	41.0	-	+
17	MAT†	43.79	12.0	194.9			-	+
18	MTJ†	43.91	14.3	197.6	137.4	33.5	-	+
19	MUN†	27.69	201.8	25.7	130.5	38.5	+	+
20	NHA†	26.21	314.8	133.8	129.9	38.8	-	-?
21	NUR†	102.06	330.5	81.6			-	-
22	PMG†	19.30	100.2	277.5	123.9	43.2	+	-
23	PRE†	95.93	243.3	100.0			+	-
24	RAB†	24.27	86.0	263.8	128.9	39.8	-	-
25	RIV†	34.77	144.8	316.5	134.2	35.5	+	-?
26	SEO†	43.75	358.9	178.7	137.8	33.8	-	-
27	SHI†	80.57	301.4	102.9	153.4	21.5	-	-

Table 5.1 (Concluded)

Station No.	Code	$\delta$ , deg.	Azimuth, deg.	Back Azimuth, deg.	$\theta_h^*$	$\theta_o^*$	P First Motions	SV First Motions
28	SHL†	47.27	313.7	127.3	138.9	32.5	-	-?
29	TAU†	40.20	157.8	329.2	135.5	34.5	-	-
30	WEL†	54.21	137.3	296.6	141.8	29.5	+	-?
31	BRS§	31.53	134.3	306.9			+	
32	CAN§	34.72	148.9	321.1			+	
33	KOU§	37.96	115.4	286.6			+	
34	LUG§	39.50	106.6	378.9			+	
35	NOU§	40.40	117.1	287.1			+	
36	PVC§	41.00	109.7	280.9			+	

\* For direct P wave.

† Records used in this study.

‡ P waves subjected to spectral analysis.

§ Only P wave first motion used (as reported in the bulletin of the station).

Table 6.1  
DATA LIST AND PERTINENT INFORMATION CONCERNING THE BRAZIL DEEP SHOCK

Station No.	Code	$\lambda$ , deg.	Azimuth, deg.	Back Azimuth, deg.	$\theta_h^*$ , deg.	$\left  \frac{d\theta_h}{d\lambda} \right ^*$	$c^*$ , km/sec	P First Motions	SV First Motions
1	AAM†	52.25	348.6	164.7	135	0.60	15.50	-, -	-?
2	AFI†	97.70	254.6	101.2	154.0	0.18	24.84	-, -	-?
3	ANP†	159.69	324.0	39.9				-†	
4	ANT†	14.65	176.1	355.8	102.5	3.15	11.20	+	
5	AQU†	92.25	47.6	260.0	153.2	0.20	24.10	-, -	
6	ARE†	7.42	179.9	359.9				-	
7	ATL†	43.93	344.5	161.6	130.5	0.56	14.33	-	
8	ATU†	99.57	53.0	266.1	154.1	0.13	24.86	-, -	+
9	BAG†	166.11	303.2	59.4				-†	
10	BHP†	19.56	335.6	155.6	112.5	1.65	11.83	-	
11	BKS†	66.44	318.1	123.4				-	
12	BLA†	46.72	350.2	167.9	131.7	0.60	14.6	-	-?
13	BNG§	90.74	85.7	261.1				+?	
14	BOG†	13.77	349.2	169.3	101.3	3.33	11.1	+?	?
15	BOZ†	64.95	330.5	136.0	142.5	0.55	17.8	-, -	+
16	BUL†	96.30	111.5	258.1	153.8	0.14	24.7	-, -	+?
17	CAR†	19.89	13.1	193.2	113.0	1.58	11.9	-	+?
18	CLS§	67.09	318.6	123.4				-	
19	CMC†	82.66	344.7	136.6	150.6	0.42	22.2	-, -	-?
20	CRT§	78.27	49.1	249.2				-	
21	COP†	93.95	34.4	260.0	153.5	0.12	24.4	-, -	+?
22	DAL†	48.09	331.1	145.5	130.25	0.61	14.8	-	
23	DUG†	62.74	325.9	132.8	141.0	0.56	17.35	-, -	+
24	DUS§	85.99	33.1	248.4				-	
25	FLO†	50.70	340.9	155.6	134.2	0.60	15.2	-, -	+
26	FUQ§	14.55	315.1	171.2				+	
27	GDH†	79.07	6.4	198.1	149.3	0.53	21.3	-, -	+

Table 6.1 (Continued)

Station No.	Code	$\delta$ , deg.	Azimuth, deg.	Back Azimuth, deg.	$\theta_h^*$ , deg.	$\left  \frac{d\theta_h}{d\delta} \right ^*$	$c^*$ , km/sec	P First Motions	SV First Motions
28	GEO†	47.93	354.1	172.6	130.25	0.61	14.76	-, -	+
29	GOL†	57.73	329.4	139.4	138.1	0.57	16.32	-, -	+
30	GRH§	91.79	124.0	258.1				-	+
31	GSC†	61.27	318.4	126.8				-	+
32	HKC†	165.69	338.3	23.3				-†	
33	HLW†	105.53	61.5	268.4	154.6	0.10	25.4	-, -	
34	IST†	103.74	50.0	270.0	154.5	0.11	25.3	-, -	
35	KEV†	101.34	20.6	274.9	154.3	0.12	25.15	-, -	
36	KIP†	90.03	291.6	99.6	150.28	0.18	23.8	-	+?
37	KON†	93.22	30.2	257.8	153.3	0.12	24.3	-, -	+?
38	KTG†	85.99	14.9	228.9	152.0	0.45	23.3	-, -	+
39	LAH†	141.14	49.8	297.8				-†	
40	LON†	71.28	326.0	126.6				-	+
41	LPA†	28.63	156.3	331.1	121.7	0.75	12.6	-	
42	LPB†	8.19	156.4	335.7				-	
43	LPS†	29.03	332.7	141.8	122.0	0.77	12.85	-	+
44	LUA§	83.47	98.1	261.9				-	
45	LWI§	99.81	93.9	260.5				-	
46	MAL†	77.50	49.3	248.8				-	
47	MAN†	166.46	295.8	66.8				-†	
48	MHC§	65.75	317.9	123.7				-	
49	MNN†	57.12	341.8	154.2				-	
50	MUN†	138.60	189.9	168.4				-†	
51	NAI†	107.86	94.3	260.2	154.8	0.07	25.5	-, -	
52	NNA†	6.03	240.1	61.0				+	
53	NOR†	94.02	6.9	234.0	153.5	0.12	24.4	-, -	+?
54	NUR†	100.80	30.1	270.9	154.2	0.13	25.1	-, -	
55	OGD†	49.90	356.9	176.0	133.5	0.62	15.1	-, -	+

Table 6.1 (Concluded)

Station No.	Code	$\Delta$ , deg.	Azimuth, deg.	Back Azimuth, deg.	$\theta_h^*$ , deg.	$\frac{d\theta_h}{d\Delta}^*$	c, km/sec	P First Motions	SV First Motions
56	OXF‡	46.49	339.5	155.2	131.5	0.60	14.6	-	+
57	PAL†	49.81	357.6	176.9				-	+
58	PAS†	61.62	316.7	125.2				-	+
59	PCU§	60.54	325.8	134.1				-	+
60	PDA†	63.20	39.6	232.6	141.2	0.56	17.4	-	+
61	PRE†	94.80	116.9	257.7	153.6	0.15	24.5	-, -	+?
62	PRI§	64.43	317.3	124.1				-	+
63	PTO†	76.23	43.8	244.9	147.5	0.42	20.3	-, -	+
64	QUE†	135.88	55.6	289.8				-†	
65	RCD†	60.13	334.1	143.2				-	
66	RDJ†	30.41	120.4	292.4				+	
67	RIV†	121.24	221.3	128.5				-†	
68	SBA†	93.29	179.7	181.3	153.4	0.22	24.3	-, -	
69	SCP†	49.91	353.7	171.8	133.5	0.62	15.1	-, -	+
70	SEO†	147.02	332.5	35.1				-†	
71	SHA†	46.22	340.9	156.9				-	
72	STR§	89.66	40.7	256.1				-	
73	STU†	90.62	40.8	257.1	152.9	0.17	23.85	-, -	+
74	TOL†	78.92	46.4	248.4	149.0	0.53	21.3	-, -	+
75	TRIT	93.06	44.4	260.4				-	
76	TRN†	21.95	27.5	207.6	116.0	1.25	12.1	+	
77	TUC†	55.61	319.5	130.7	137.0	0.56	15.9	-	+?
78	VAL†	80.09	33.4	241.5	149.5	0.50	21.6	-, -	+

\* For direct P wave.

† Records used in this study.

‡ P waves subjected to spectral analysis.

§ Only P-wave first motion used (as reported in the bulletin of the Station).

|| For pP wave.

†† For PKP wave

Table 6.2  
CRUSTAL STRUCTURES

<u>Profile No.</u>	<u>Thickness</u>	<u>Alpha</u>	<u>Beta</u>	<u>Density</u>	<u>Station</u>
1	6.00	3.60	2.08	2.46	COP, KEV, KON, NUR
	7.50	5.40	3.12	2.74	
	13.90	6.50	3.75	2.98	
	∞	8.20	4.56	3.44	
2	2.40	5.63	3.25	2.79	STU, AQU, TOL, PTO, VAL
	17.70	5.97	3.45	2.86	
	10.10	6.54	3.77	2.99	
	∞	8.15	4.54	3.43	
5	10.00	4.50	2.60	2.61	ATU, IST
	13.00	6.00	3.46	2.86	
	∞	8.10	4.51	3.41	
6	7.00	4.30	2.48	2.58	HLW
	17.00	5.60	3.23	2.78	
	24.00	6.50	3.67	2.98	
	∞	8.00	4.45	3.38	
22	1.30	5.40	3.12	2.75	PRE, BUL, NAI
	36.60	6.20	3.54	2.91	
	∞	8.21	4.57	3.44	
29	4.10	5.30	3.06	2.73	BOG, BHP, LPS, CAR, TRN
	21.20	6.20	3.58	2.91	
	26.40	6.70	3.78	3.03	
	∞	8.00	4.45	3.38	
31	6.00	5.50	3.18	2.76	ANT, LPA
	28.40	6.35	3.64	2.94	
	35.90	7.00	3.90	3.10	
	∞	8.00	4.45	3.38	
40	6.10	5.70	3.29	2.80	CMC, KTG, GDH, NOR
	10.60	6.60	3.82	3.00	
	32.20	7.30	4.12	3.18	
	∞	8.30	4.62	3.47	
47	2.78	3.60	2.08	2.46	BOZ
	12.93	6.08	3.51	2.88	
	24.61	6.88	3.92	3.07	
	∞	8.15	4.54	3.43	

Table 6.2 (Concluded)

<u>Profile No.</u>	<u>Thickness</u>	<u>Alpha</u>	<u>Beta</u>	<u>Density</u>	<u>Station</u>
56	1.44	4.58	2.65	2.62	AAM
	6.05	5.74	3.32	2.81	
	30.00	6.22	3.58	2.91	
	∞	8.17	4.55	3.43	
62	0.70	5.60	3.24	2.79	OGD, GEO, SCP
	4.30	6.28	3.63	2.93	
	5.00	6.42	3.71	2.95	
	5.00	6.54	3.78	2.98	
	5.00	6.68	3.86	3.01	
	5.00	6.82	3.94	3.04	
	5.00	6.94	4.00	3.07	
	2.50	7.00	4.03	3.10	
∞	8.10	4.51	3.41		
63	5.30	6.10	3.52	2.89	ATL, BLA
	8.42	6.33	3.64	2.94	
	31.58	6.73	3.80	3.03	
	∞	8.06	4.50	3.40	
64	2.03	4.64	2.66	2.63	OXF, FLO, DAL
	8.19	5.18	3.01	2.71	
	30.98	6.64	3.75	3.01	
	∞	8.16	4.55	3.43	
65	4.30	4.80	2.80	2.65	TUC
	11.70	6.10	3.52	2.89	
	22.10	7.36	4.15	3.20	
	8.80	7.34	4.14	3.19	
	∞	8.15	4.54	3.43	
66	5.90	5.20	3.02	2.71	DUG, GOL
	11.70	5.80	3.35	2.82	
	21.30	6.26	3.63	2.92	
	8.80	7.34	4.14	3.19	
	∞	8.18	4.55	3.44	
*	1.50	5.80	3.35	2.83	AFI, KIP
	22.50	6.15	3.55	2.90	
	∞	7.75	4.31	3.31	

Table 6.3

SOME POSSIBLE FAULT-PLANE SOLUTIONS

<u>Fault-Plane Circle</u>	<u>Strike</u>	<u>dip, <math>\delta</math></u>	<u>slip, <math>\lambda</math></u>
I <sub>a</sub>	$180 \pm 10^\circ$	$52 \pm 10^\circ$	$246^\circ - 270^\circ$
I <sub>b</sub>	$145 \pm 10^\circ$	$45 \pm 10^\circ$	$242^\circ - 270^\circ$
II <sub>a</sub>	$180 \pm 10^\circ$	$45 \pm 10^\circ$	$246^\circ - 270^\circ$
II <sub>b</sub>	$150 \pm 10^\circ$	$50 \pm 10^\circ$	$249^\circ - 270^\circ$

Table 6.4

## THE SPACE-TIME RELATIONSHIPS OF THE THREE DEEP SHOCKS

<u>Earthquake</u>	<u>Date</u>	<u>Time (UT)</u>	<u>Epicenter</u>	<u>Distance,</u> <u>deg.</u>	<u>* Azimuth,</u> <u>deg.</u>	<u>Back *</u> <u>Azimuth,</u> <u>deg.</u>
Brazil	Nov. 9, 1963	21 15 30.4	71.5°W, 9.0°S	6.03	61.0	240.0
Peruvian I	Aug. 19, 1961	05 09 49.5	70.8°W, 10.8°S	6.04	79.3	258.2
Peruvian II	Aug. 31, 1961	01 57 07.9	70.6°W, 10.3°S	6.35	75.3	254.1

\* With respect to the recording station Ñaña (11.99°S, 76.84°W).

Table 7.1  
DATA LIST OF pP AND S WAVES

Station No.	Code	Window length, sec.	Component	$\delta$ , deg.	Azimuth, deg.	Back Azimuth, deg.	c, km/sec
5	AQU*	60	z	92.25	47.6	260.0	23.7
8	ATU*	60	z	99.57	53.0	266.1	24.4
15	BOZ*	60	z	64.95	330.5	136.0	16.2
16	BUL*	60	z	96.3	111.5	258.1	23.9
21	COP*	60	z	93.95	34.4	260.0	23.7
37	KON*	60	z	93.22	30.2	257.8	23.7
54	NUR*	60	z	100.80	30.1	270.9	24.5
61	PRE*	60	z	94.80	116.9	257.7	23.8
8	ATU†	81	NS	99.57	53.0	266.1	14.01
21	COP†	87	NS	93.95	34.4	260.0	13.75
27	GDH‡	71	z	79.07	6.4	198.1	12.0
34	IST†	71	NS	103.74	50.0	270.0	14.26
35	KEV†	94	NS	101.34	20.6	274.9	14.18
54	NUR†	87	NS	100.80	30.1	270.9	14.15
73	STU†	81	NS	90.62	40.8	257.1	13.41
78	VAL‡	61	z	80.09	33.4	241.5	12.17

\* pP wave.

† SH wave.

‡ SV wave.

Table 7.2

AVERAGE  $Q_{\alpha}$  OF THE UPPER MANTLE

<u>Station No.</u>	<u>Code</u>	<u>pP - P, sec.</u>	<u><math>\delta A_{pP/P'}</math> sec.</u>	<u><math>\bar{Q}_{\alpha}</math> *</u>
5	AQU	130.8	- 6.0	63
8	ATU	131.4	- 3.2	119
15	BOZ	120.0	- 3.4	117
16	BUL	131.2	- 3.9	106
21	COP	131.1	- 3.6	110
37	KON	131.0	- 4.8	86
54	NUR	131.5	- 6.6	62
61	PRE	131.2	- 2.2	187

\* Average  $Q_{\alpha}$  between earth's surface and a depth of 430 km.

FIGURE CAPTIONS

- Figure 2.1 - Geometry of the source model and the relative position of station on the free surface.
- Figure 3.1 - A ray as a plane curve.
- Figure 3.2 - The geometry of a ray tube.
- Figure 3.3 - Diffraction of waves by a spherical body.
- Figure 3.4 - Deformation of Watson's contour.
- Figure 4.1 - A schematic diagram of body-wave propagation.
- Figure 4.2 - Instrumental response  
(a) calculated by Fourier transforming the calibration trace.  
(b) generated by theory of seismometer.
- Figure 5.1 - Frequency response of the long-period instrument of World-Wide Standardized Seismograph, showing various peak magnifications.
- Figure 5.2 - Geographic distribution of recording stations.
- Figure 5.3 - The geometry of a seismic ray.
- Figure 5.4 - A schematic diagram of P-wave propagation.
- Figure 5.5 - Comparison of amplitude responses for different crustal structures.
- Figure 5.6 - Crustal amplitude responses for different phase velocities, P - GG crust.
- Figure 5.7 - Inverse diminution as a function of frequency and epicentral distance.
- Figure 5.8 - A comparison of data and results  $f(t)$  is the vertical component of the P-wave signal,  $A(\omega)$  is the corresponding normalized spectrum, and  $A_0(\omega)$  is the equalizer spectrum which resulted from the operation indicated by (5.4). The radiation pattern at the top is for a 70-sec. period.

- Figure 5.9 - Empirical P-wave radiation patterns. The amplitude scale, in meter-seconds, is shown in the diagram for  $T = 20$  sec. Station numbers are shown in the diagram for  $T = 90$  sec. and corresponding to those given in Figure 5.8.
- Figure 5.10 - Observed and calculated P-wave radiation patterns.
- Figure 5.11 - Calculated P-wave radiation patterns for different take-off angles. The top of each diagram represents north.
- Figure 5.12 - Observed and calculated S-wave radiation patterns. Station numbers are those given in Table 5.1.
- Figure 5.13 - First-motion results from P and SV waves. Station numbers are those given in Table 5.1.
- Figure 5.14 - Lower: equalized source spectrums, all normalized to their values at 30 sec.  
Upper: the possible inferred source time function.
- Figure 6.1 - Geographic distribution of recording stations.
- Figure 6.2 - (a) Nafe and Drake's velocity density curve.  
(b) Poisson's ratio appropriate to a Gutenberg earth model.
- Figure 6.3 - Phase velocity  $c$ , take-off angle  $\theta$ , and  $d\theta/d\delta$  for a focal depth of 550 km.
- Figure 6.4 - A comparison of data and results.  $f(t)$  is the P-wave signal: those with asterisks are horizontal components, and those without are vertical components.  $A(\omega)$  is the corresponding normalized spectrum, and  $A_0(\omega)$  is the equalizer spectrum.
- Figure 6.5 - Empirical P-wave radiation patterns. The amplitude scale, in meter-seconds, is shown in diagram for  $T = 10$  sec. Station numbers are shown in the diagram for  $T = 83$  sec.
- Figure 6.6 - Left: Observed and calculated (Model A) P-wave radiation patterns.  
Middle: Observed and calculated (Model B) P-wave radiation patterns.  
Right: A comparison of Model A and Model B.  
Arrows denote far stations ( $\delta > 93^\circ$ ).

- Figure 6.7 - Calculated P-wave radiation patterns for different take-off angles. The top of each diagram represents north.
- Figure 6.8 - Teleseismic P and pP waves, showing their nearly equal amplitudes and similar wave forms as observed at the same station.
- Figure 6.9 - First-motion result from P waves.
- Figure 6.10 - First-motion result from S waves.
- Figure 6.11 - A comparison of the strain records of the Brazil deep earthquake and the two Peruvian deep earthquakes.
- Figure 6.12 - Equalized source spectrums, all normalized to their values at 0.3 cps.  $\tau$  is the time constant defined in (5.5).
- Figure 7.1 - Geographical distribution of the recording stations.
- Figure 7.2 - S waveforms used in the present analysis.
- Figure 7.3 - Differential attenuation,  $\delta A_{P/P}$ , data from P-wave spectral ratios.
- Figure 7.4 - Differential attenuation data.  
Left:  $\delta A_{pP/P}$  .  
Right:  $\delta A_{S/P}$  .
- Figure 7.5 - The ray paths of P and pP waves at far stations.
- Figure 7.6 - Schematic wave amplitudes near the geometrical shadow boundary.
- Figure 7.7 - A comparison of the differential attenuation data and the calculated values based on the Q models given in Figure 7.8.
- Figure 7.8 - A comparison of the resulting  $Q_a$  model with models by Anderson et al. (1964, 1965).

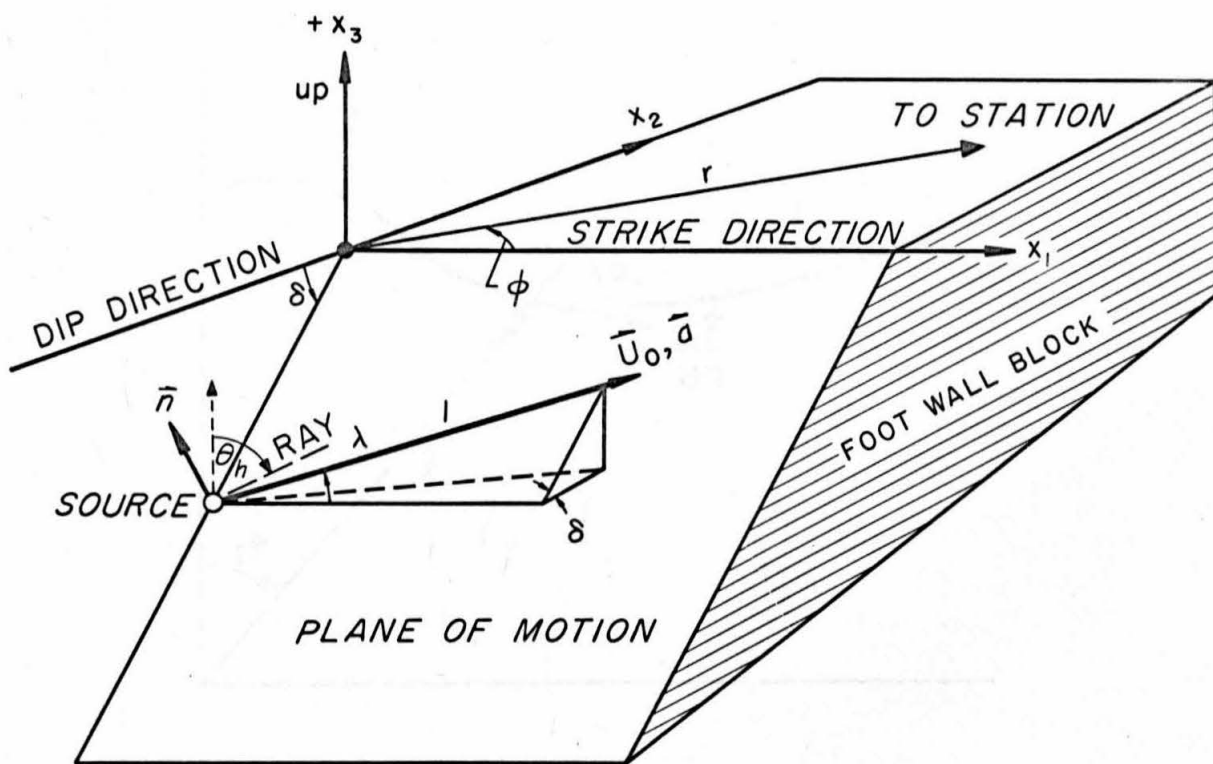


Fig. 2.1

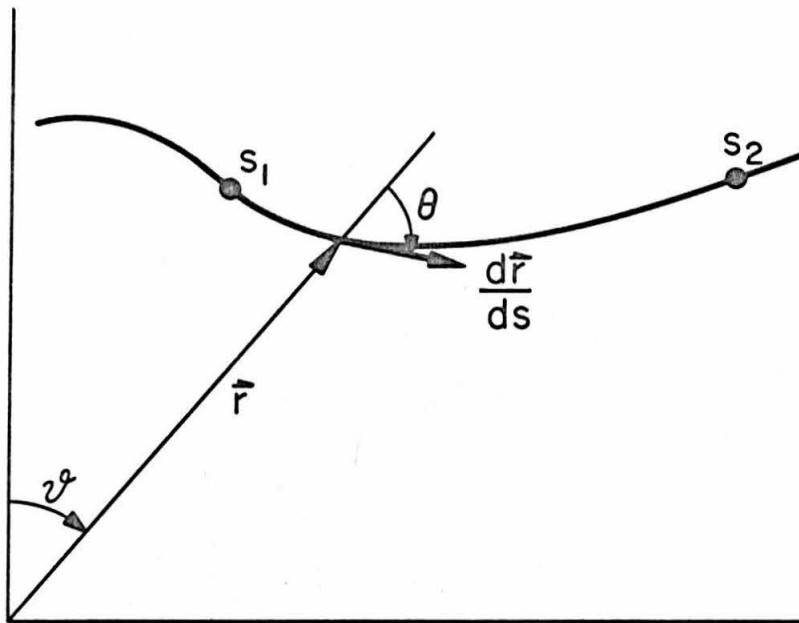


Fig. 3.1

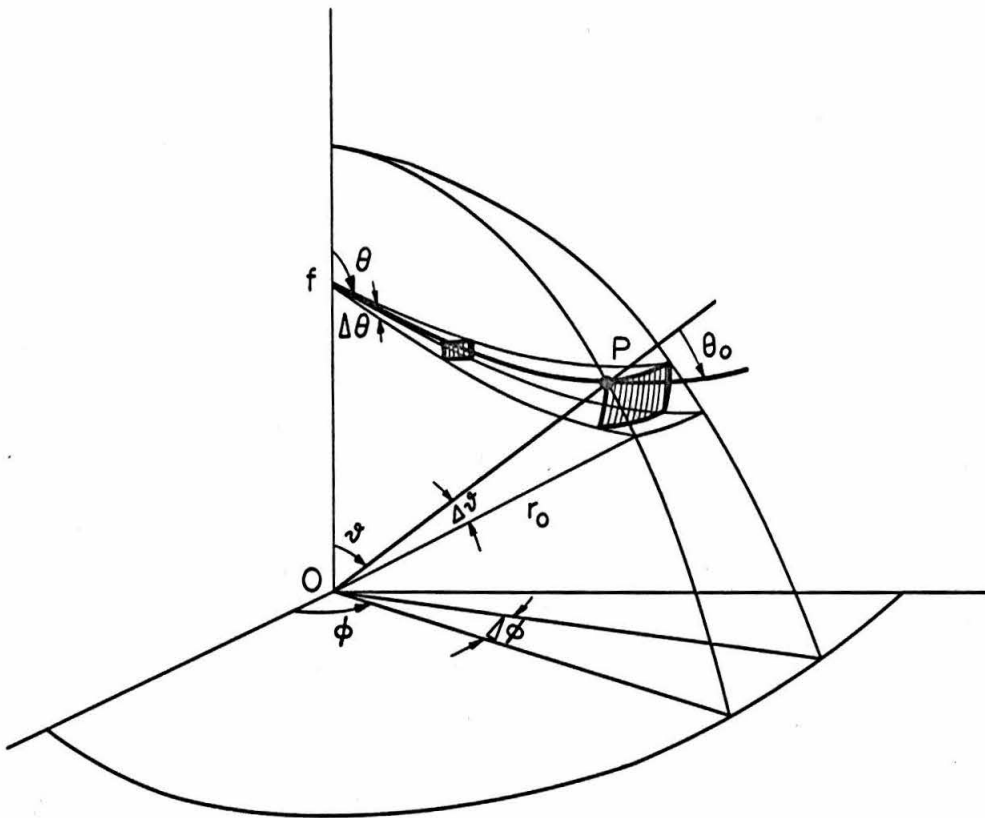


Fig. 3.2

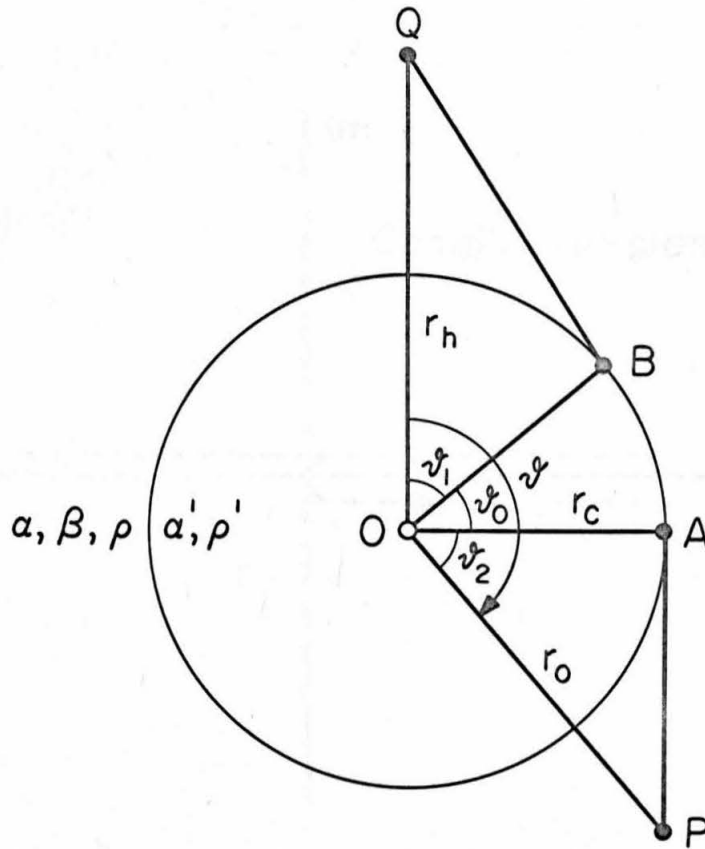


Fig. 3.3

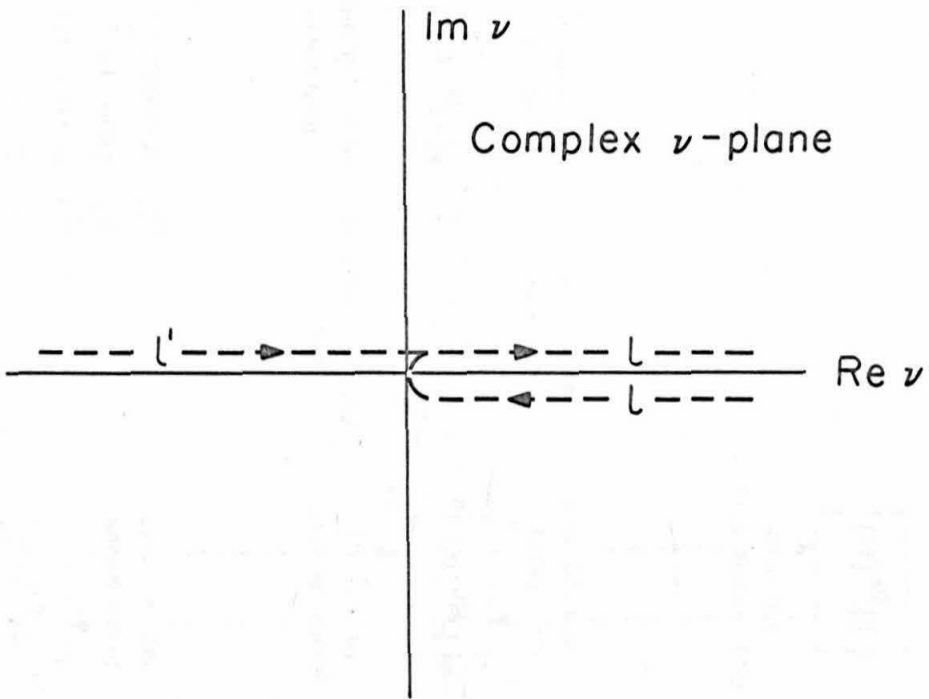


Fig. 3.4

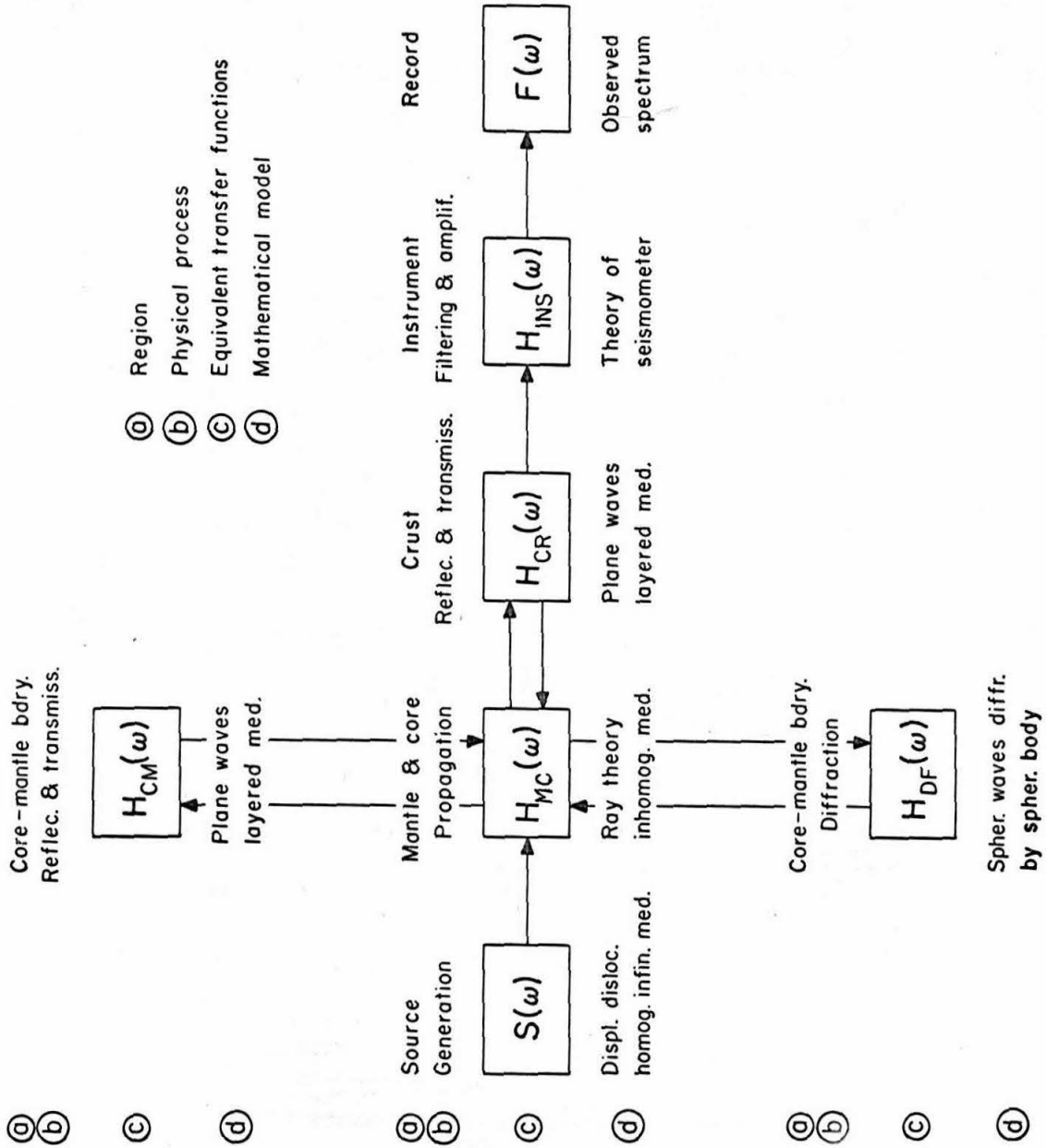


Fig. 4.1

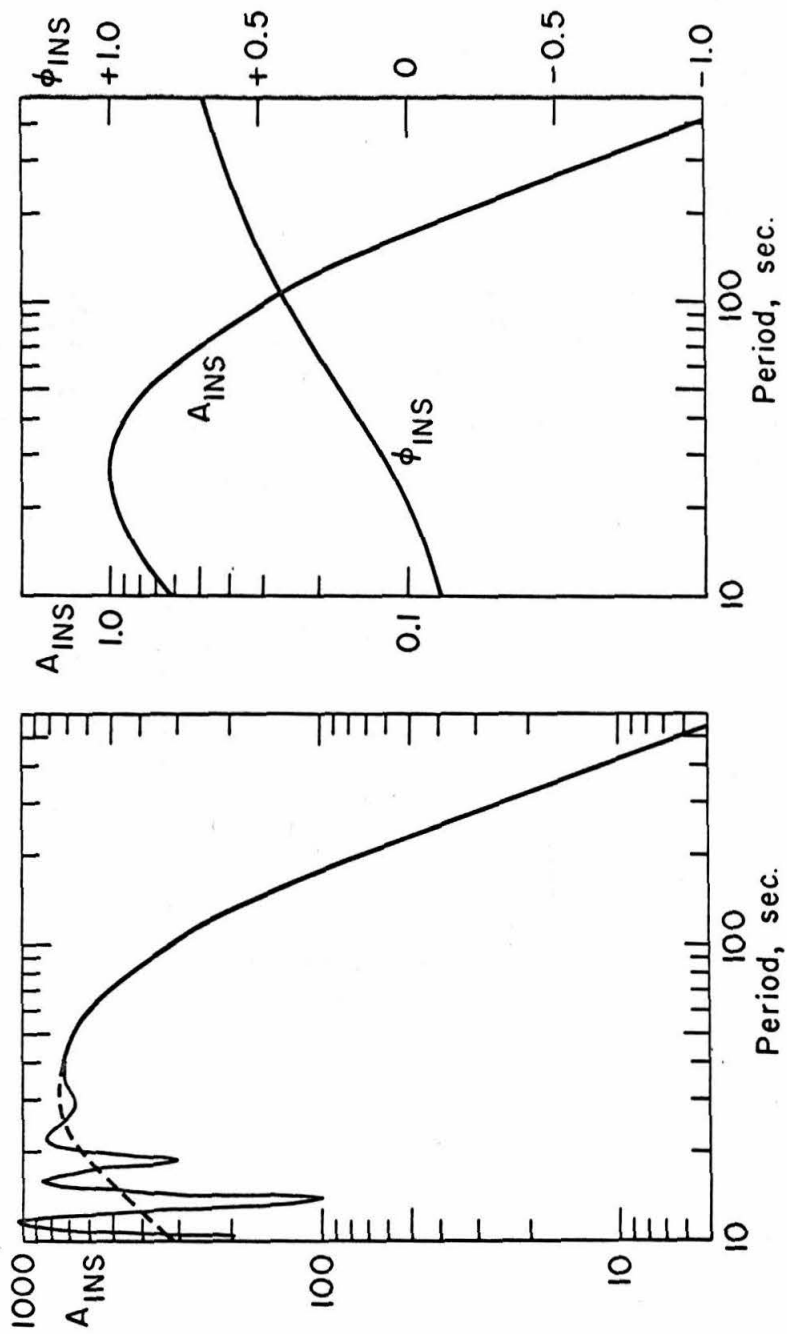


Fig. 4.2

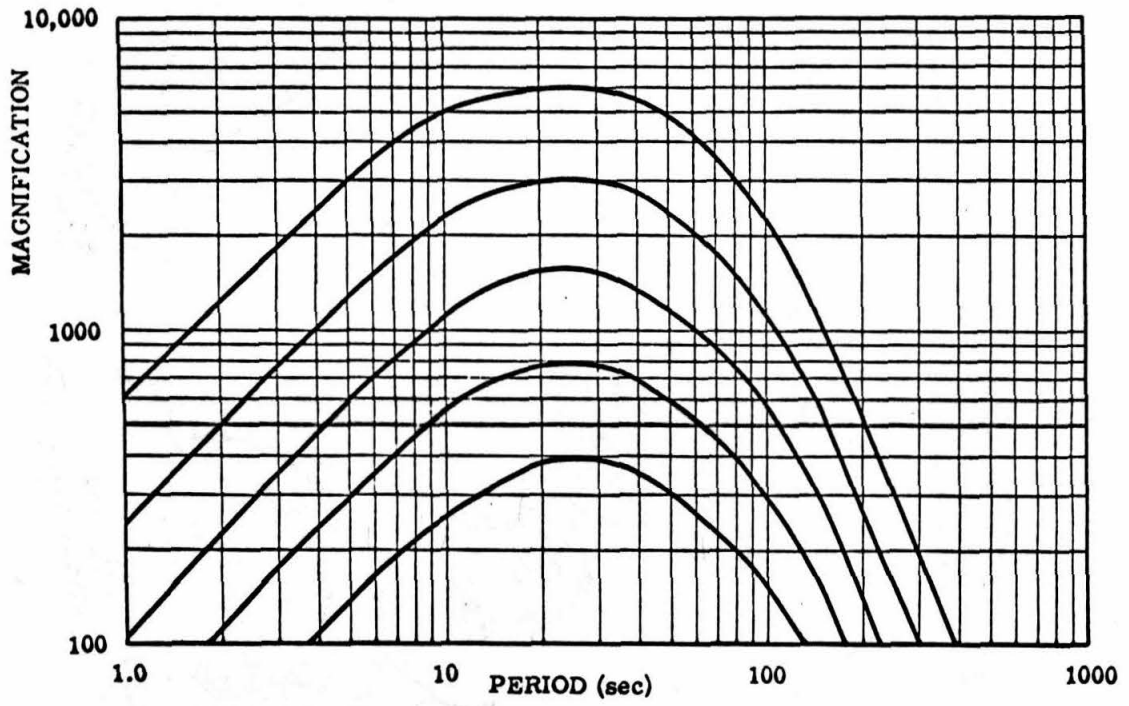


Fig. 5.1

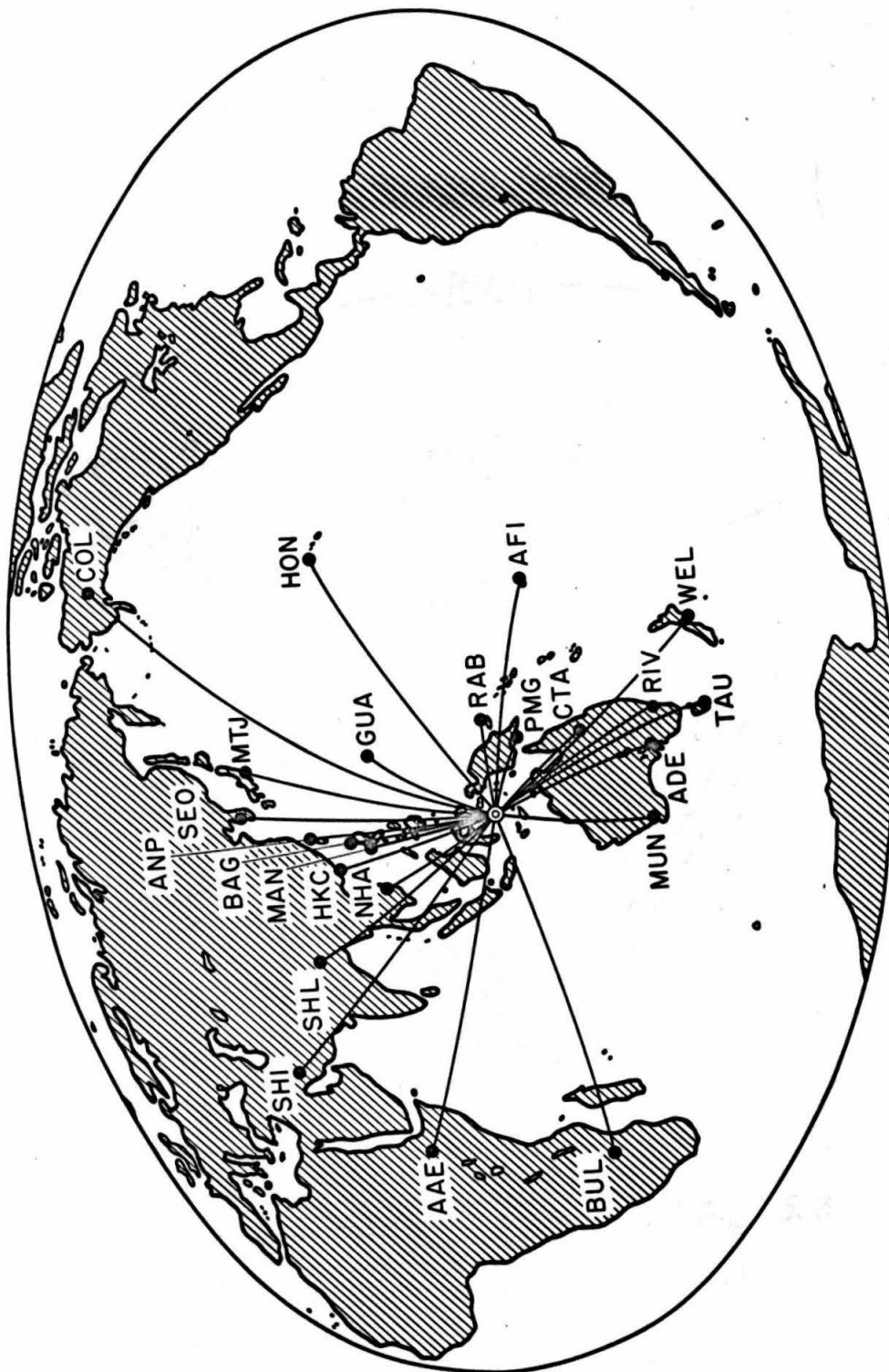


Fig. 5.2

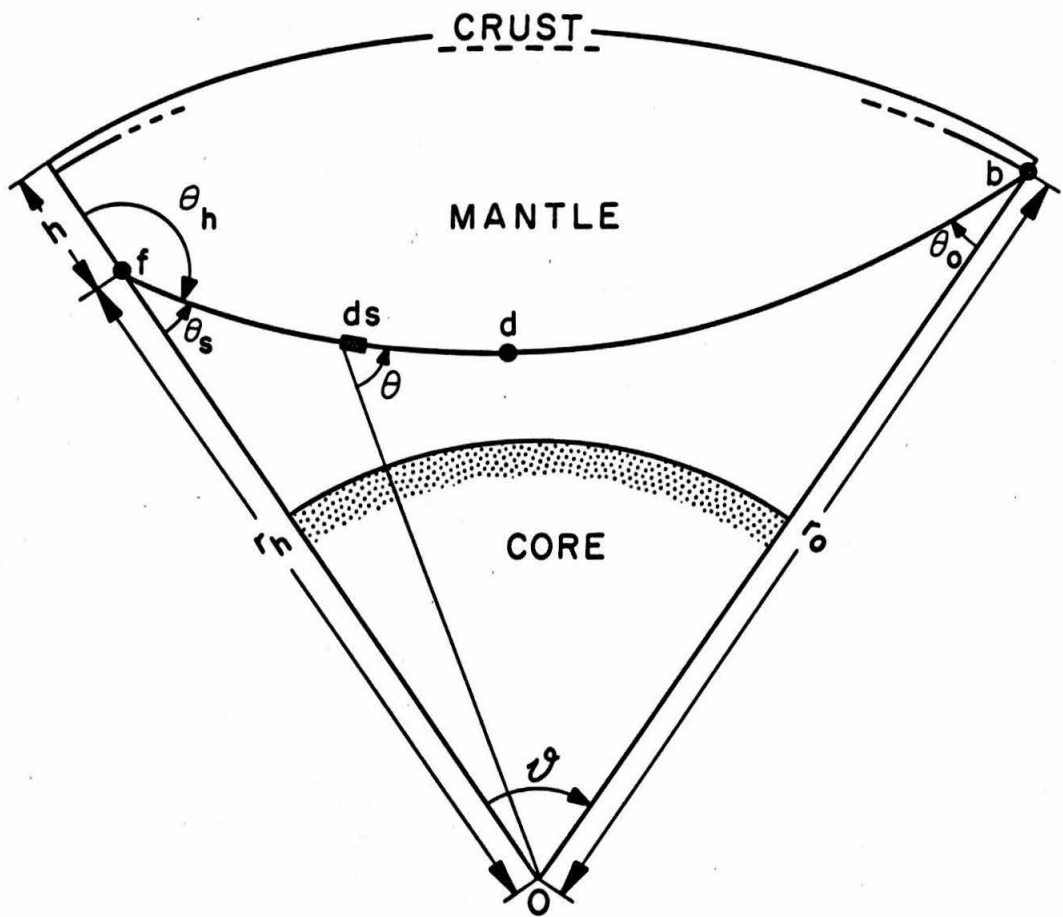


Fig. 5.3

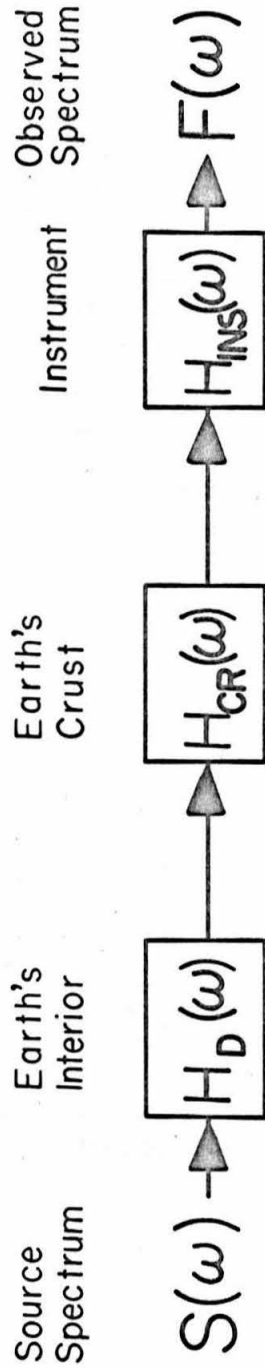


Fig. 5.4

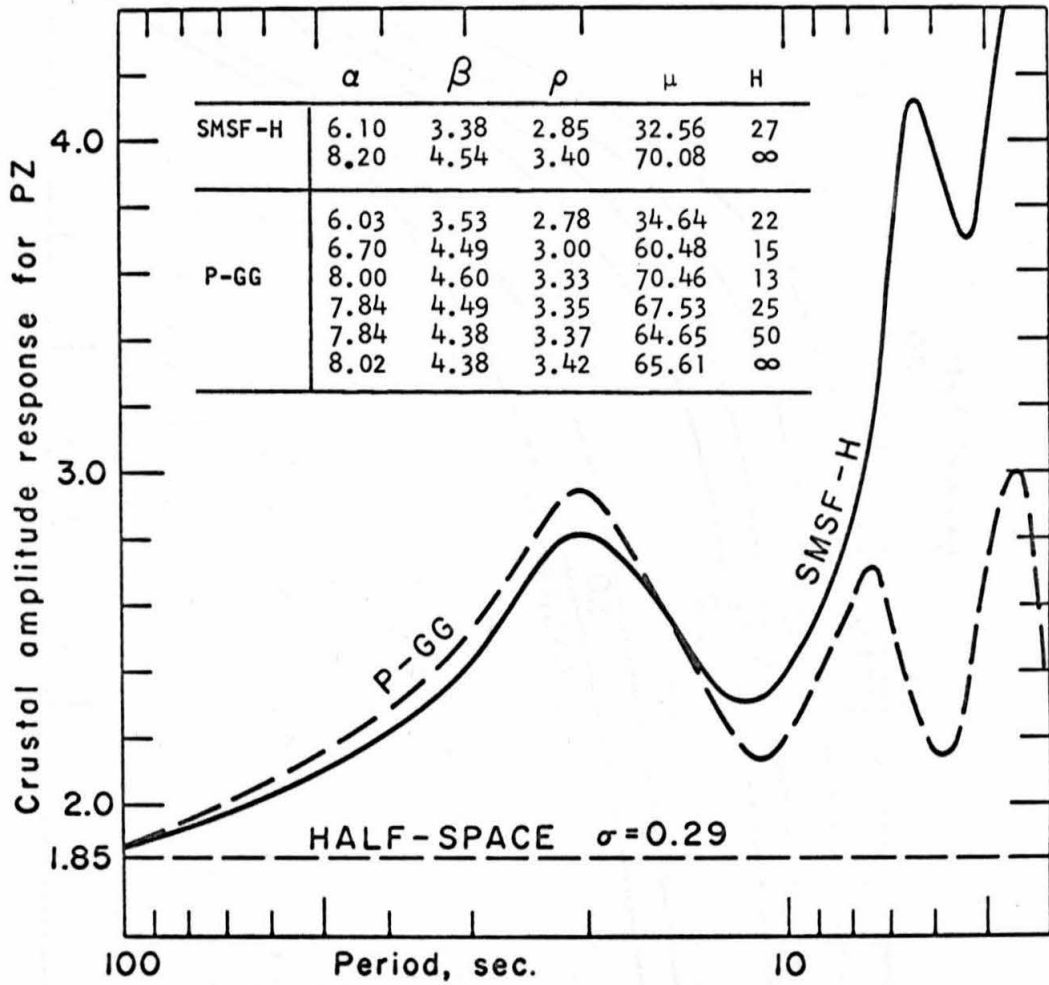


Fig. 5.5

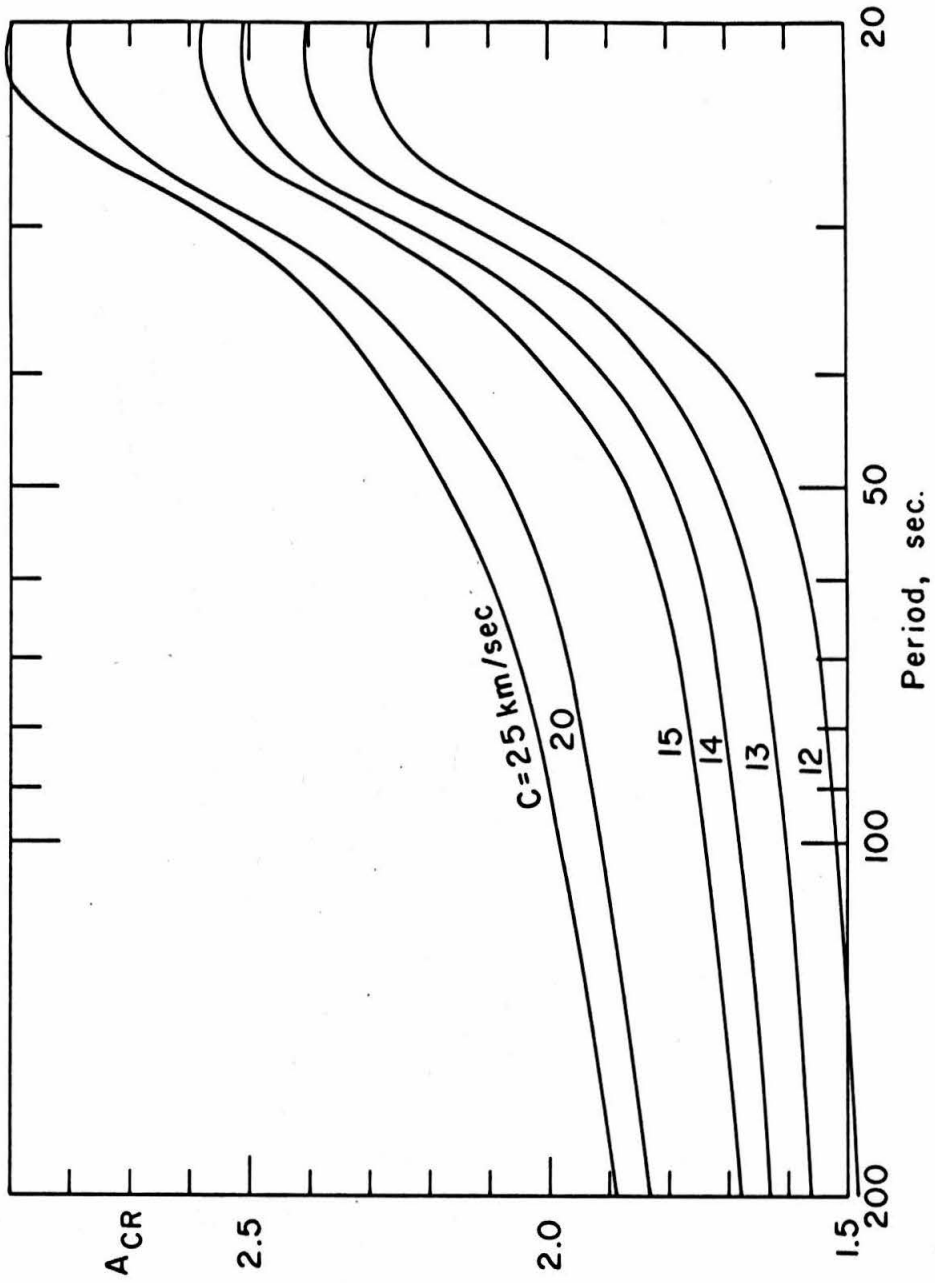


Fig. 5.6

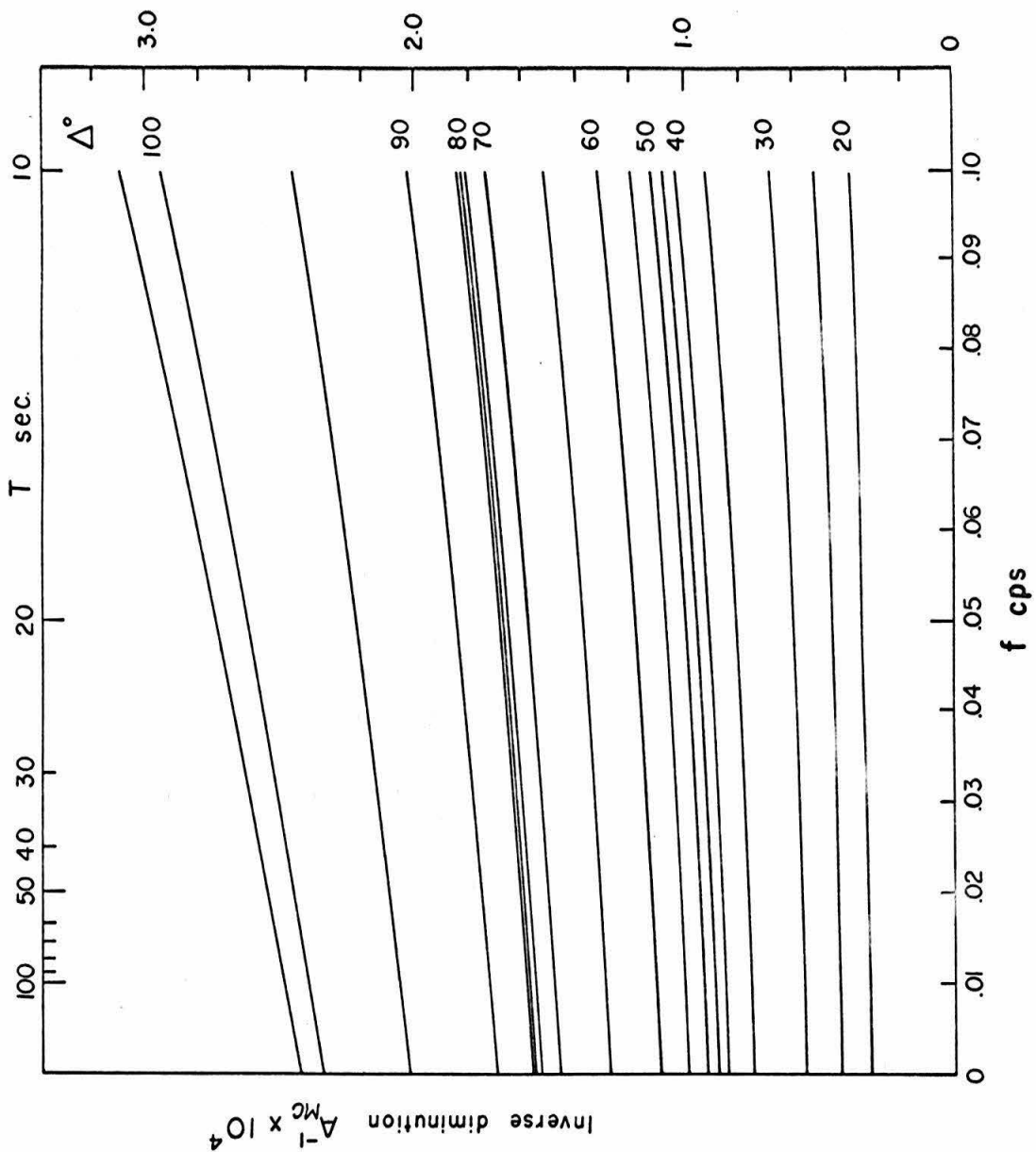


Fig. 5.7

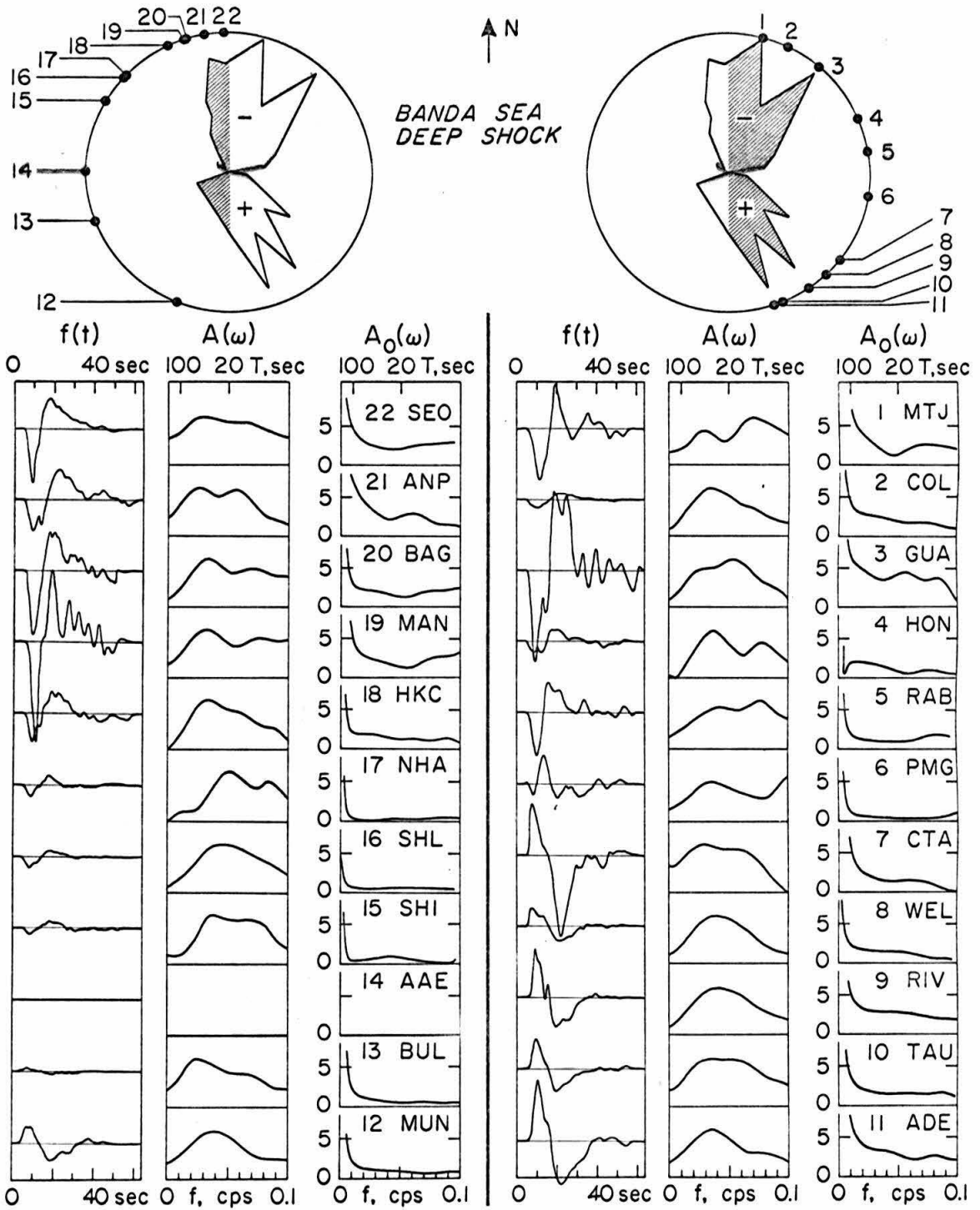


Fig. 5.8

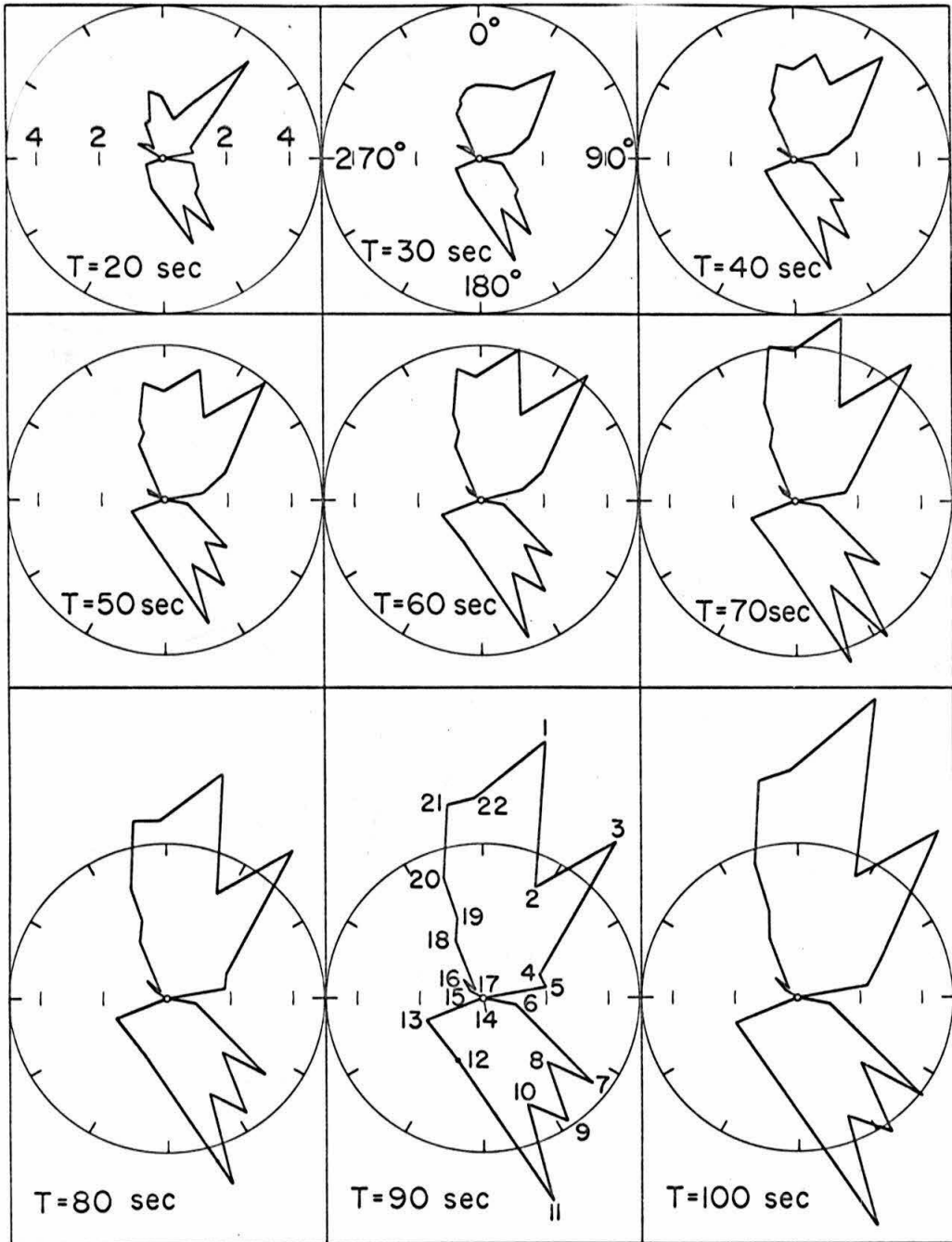


Fig. 5.9

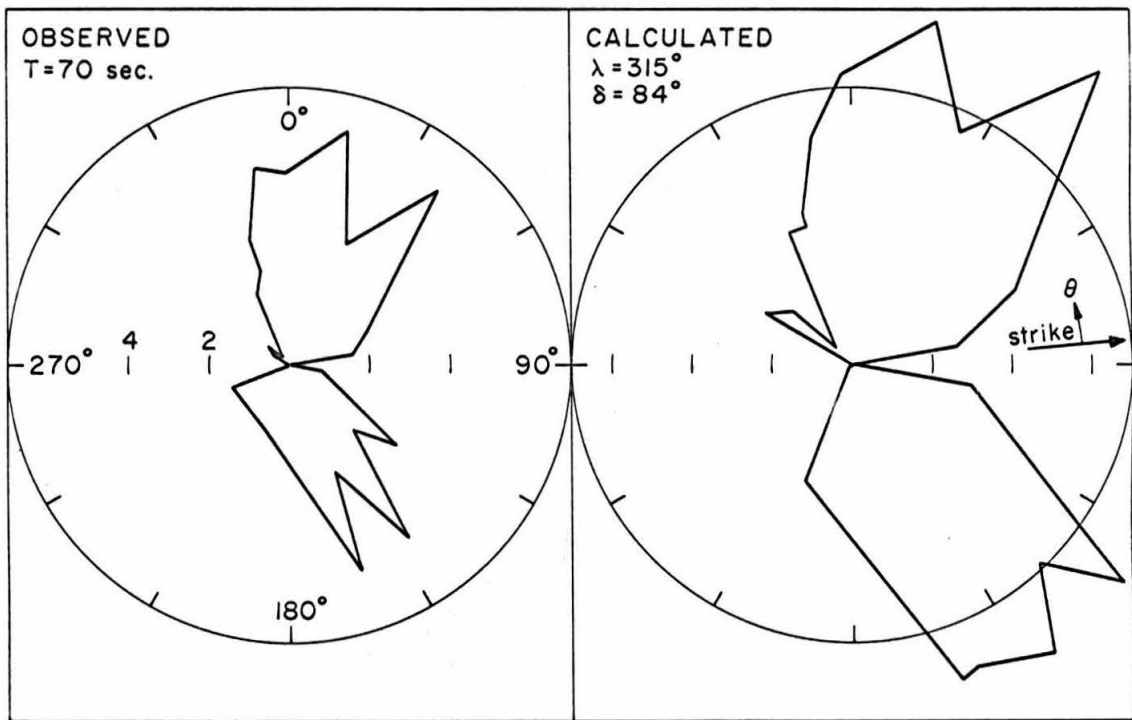


Fig. 5.10

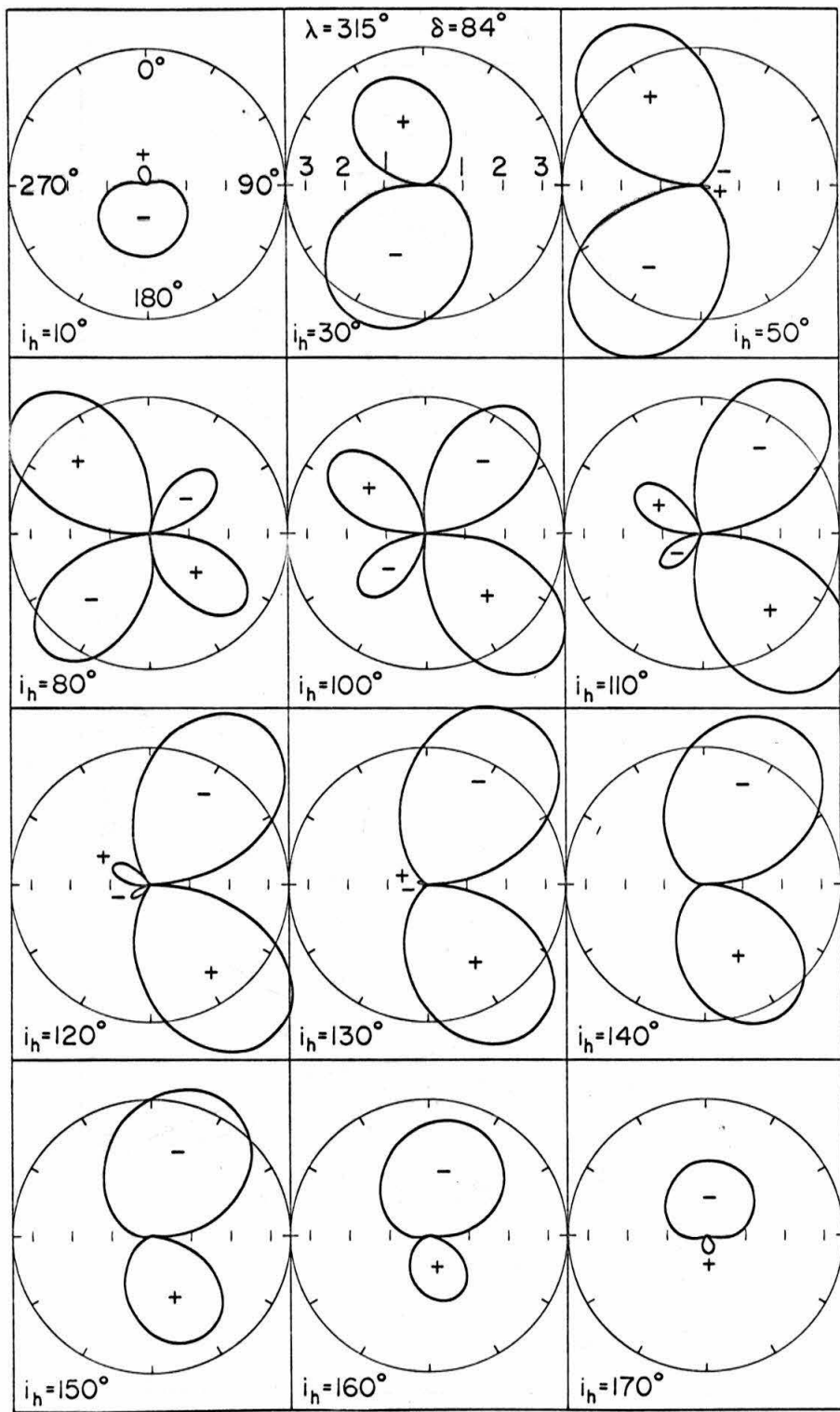


Fig. 5. 11

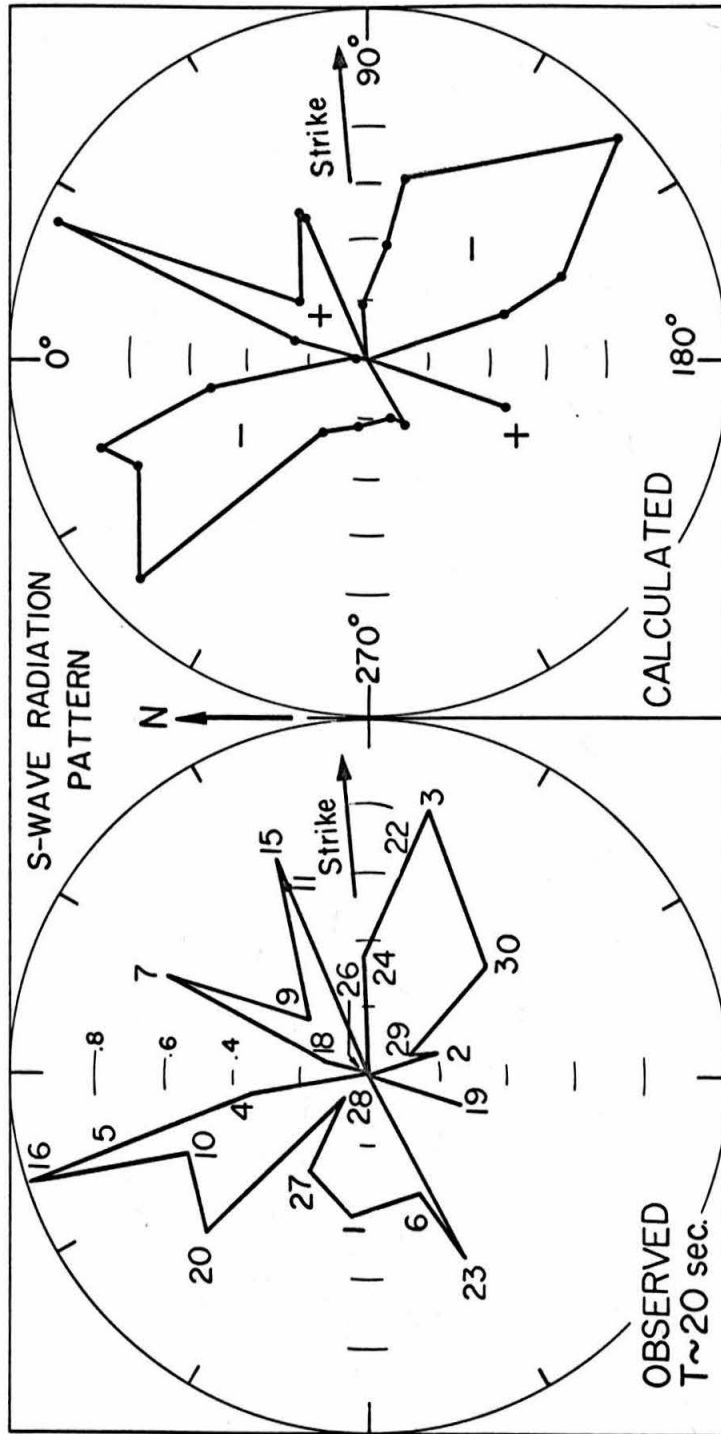


Fig. 5.12

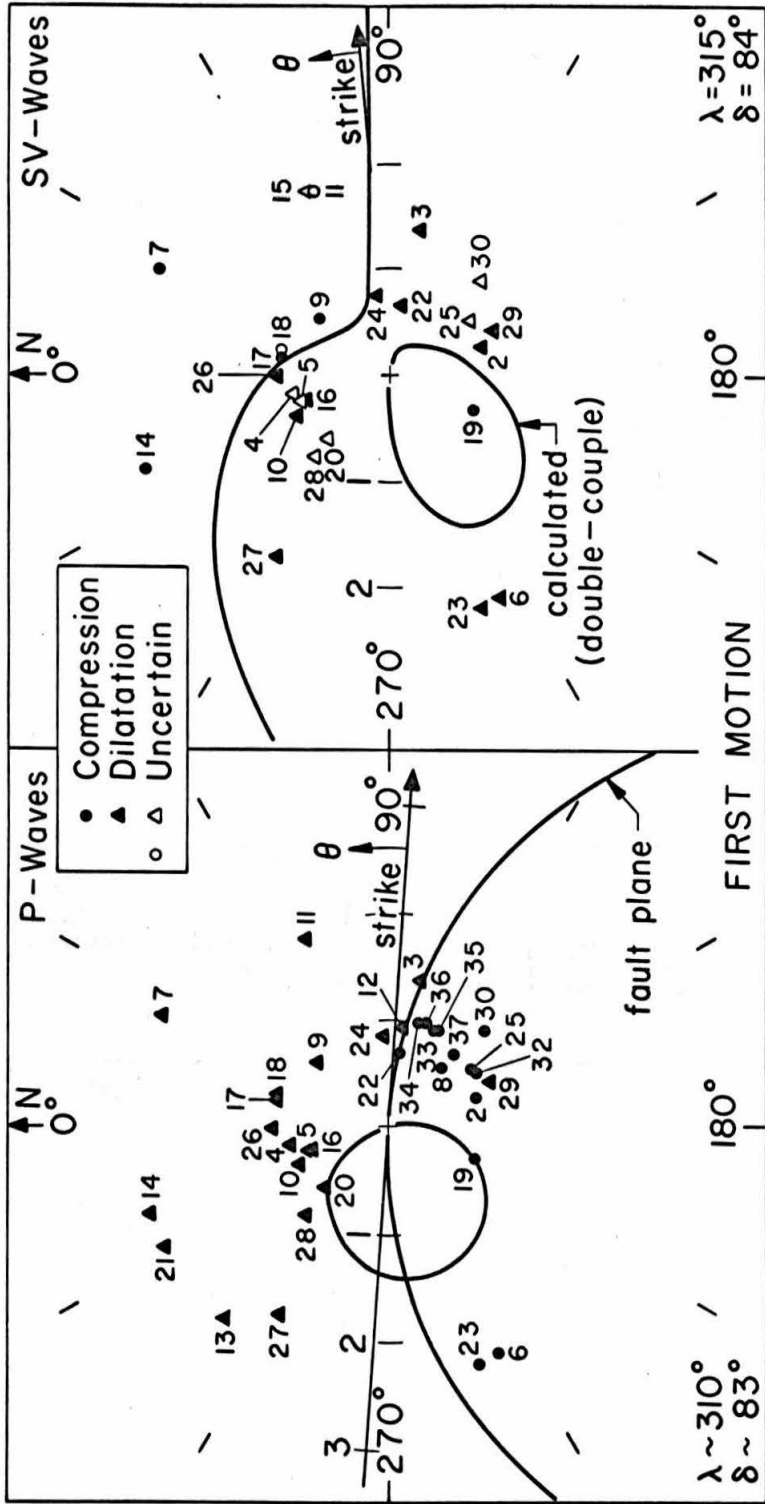


Fig. 5.13

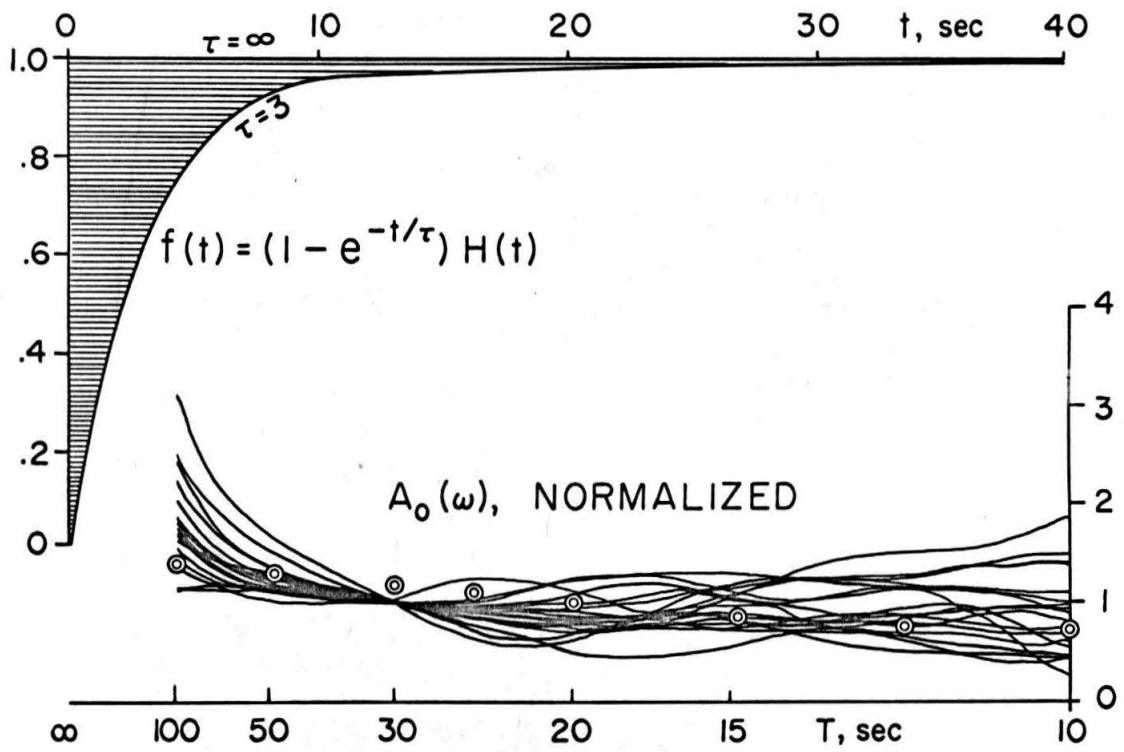


Fig. 5.14

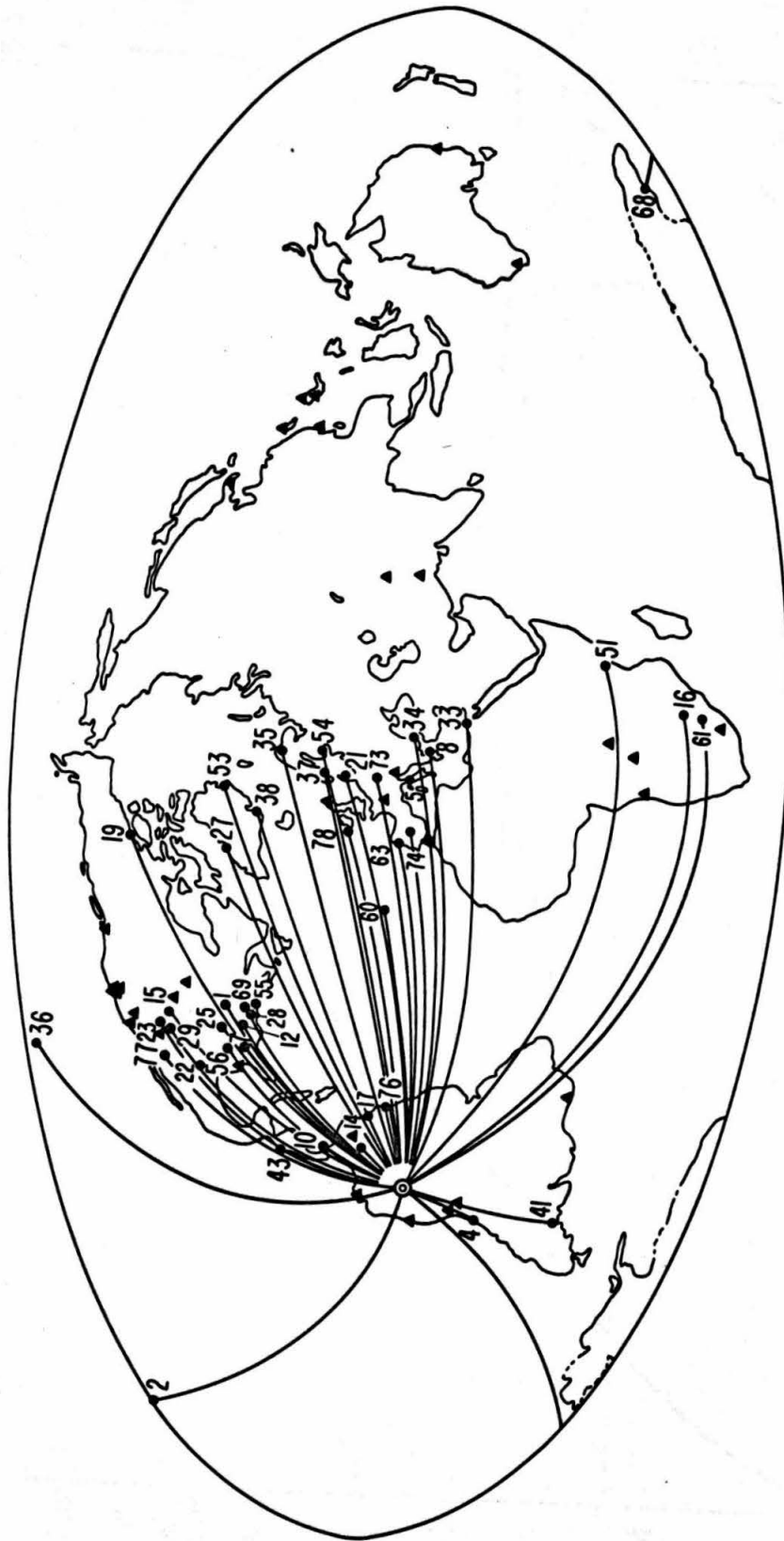


Fig. 6.1

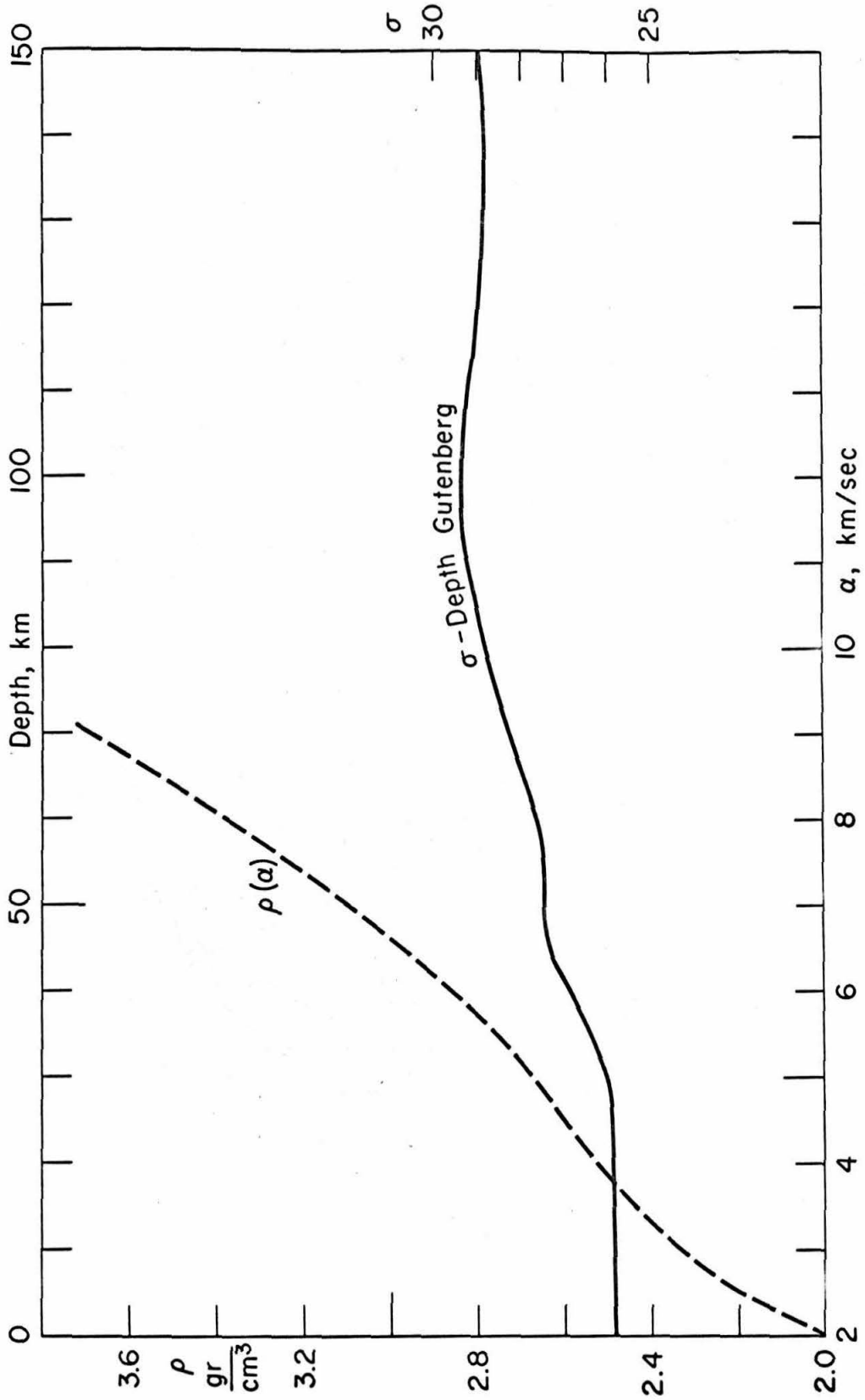


Fig. 6.2

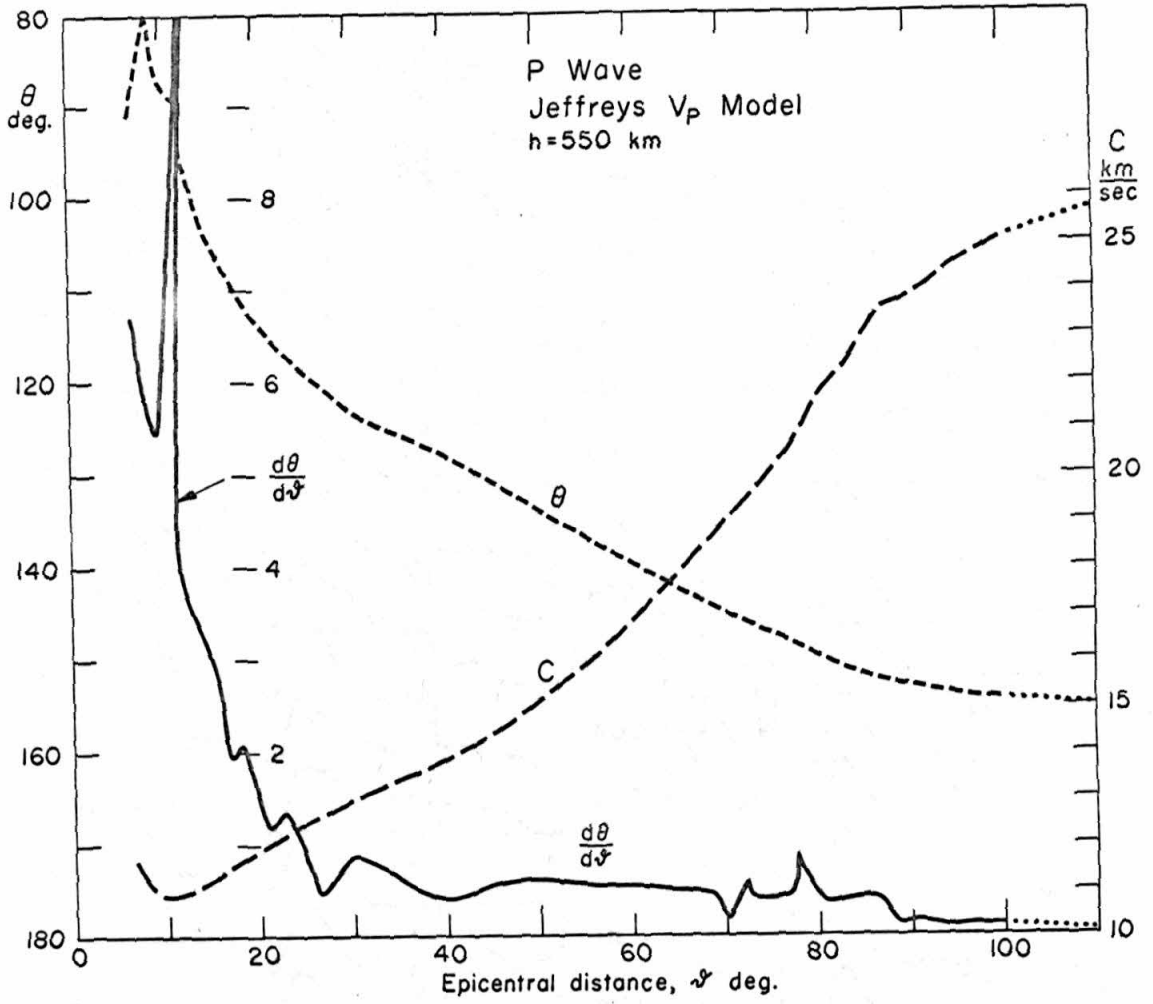


Fig. 6.3

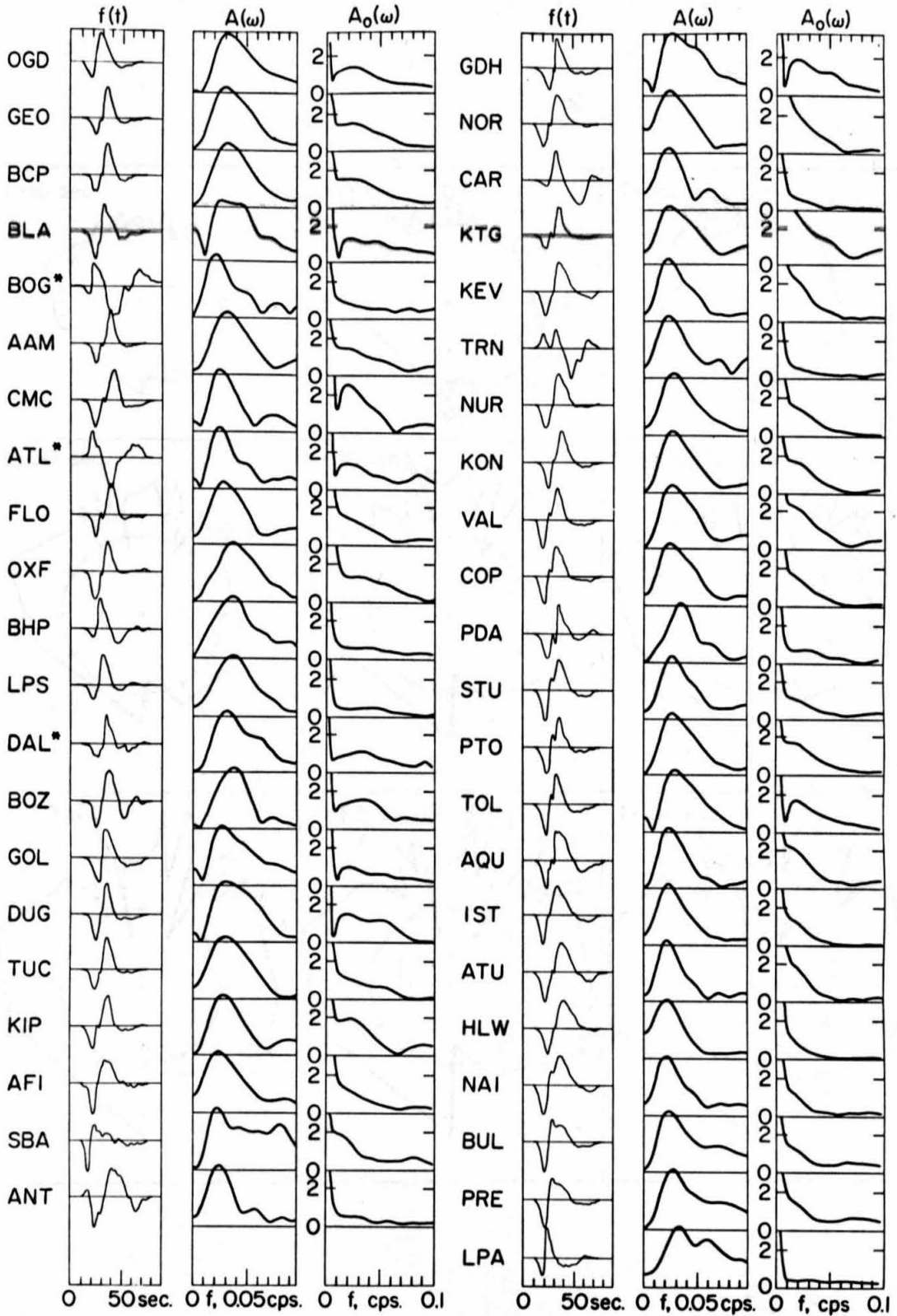


Fig. 6.4

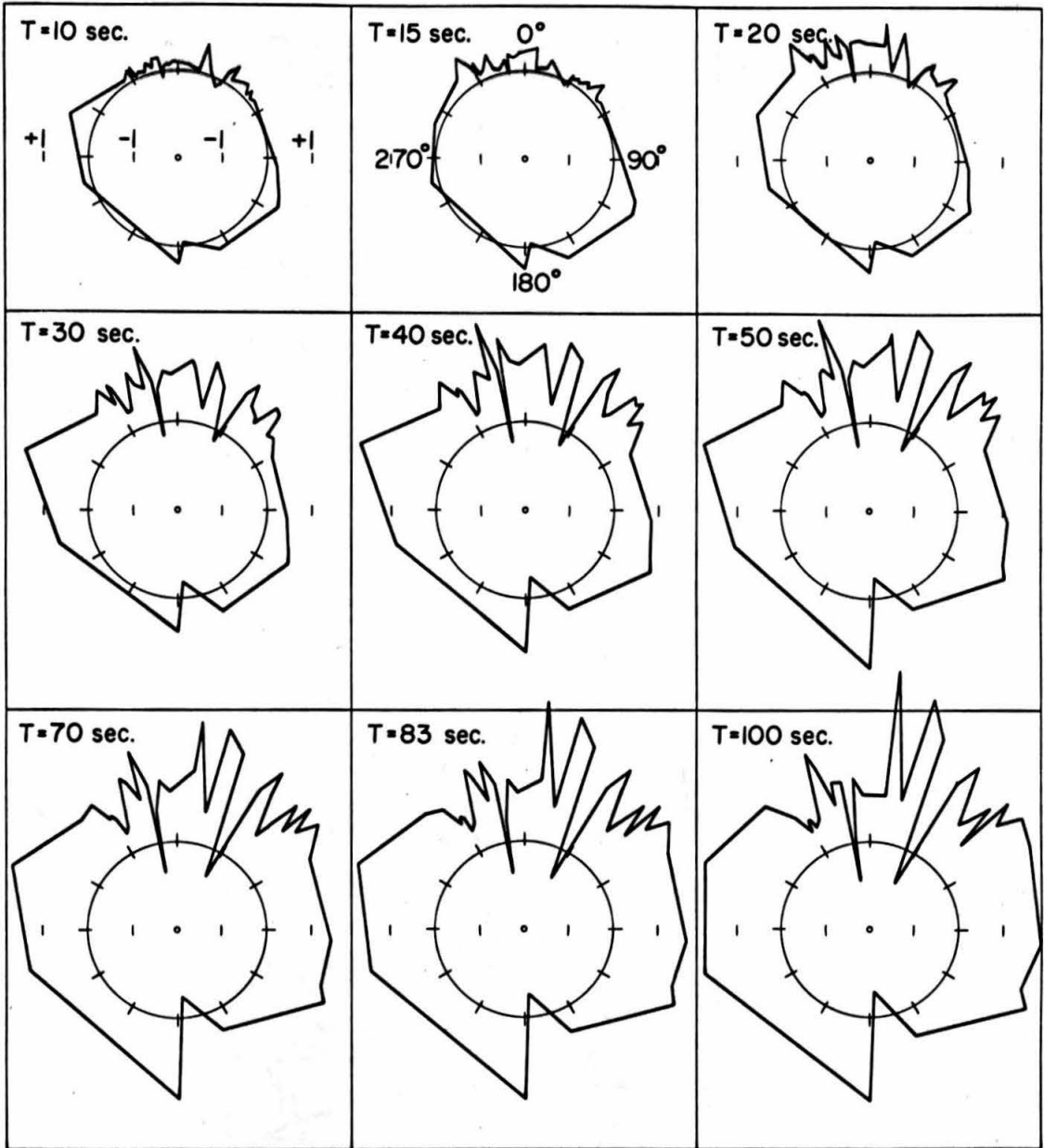


Fig. 6.5

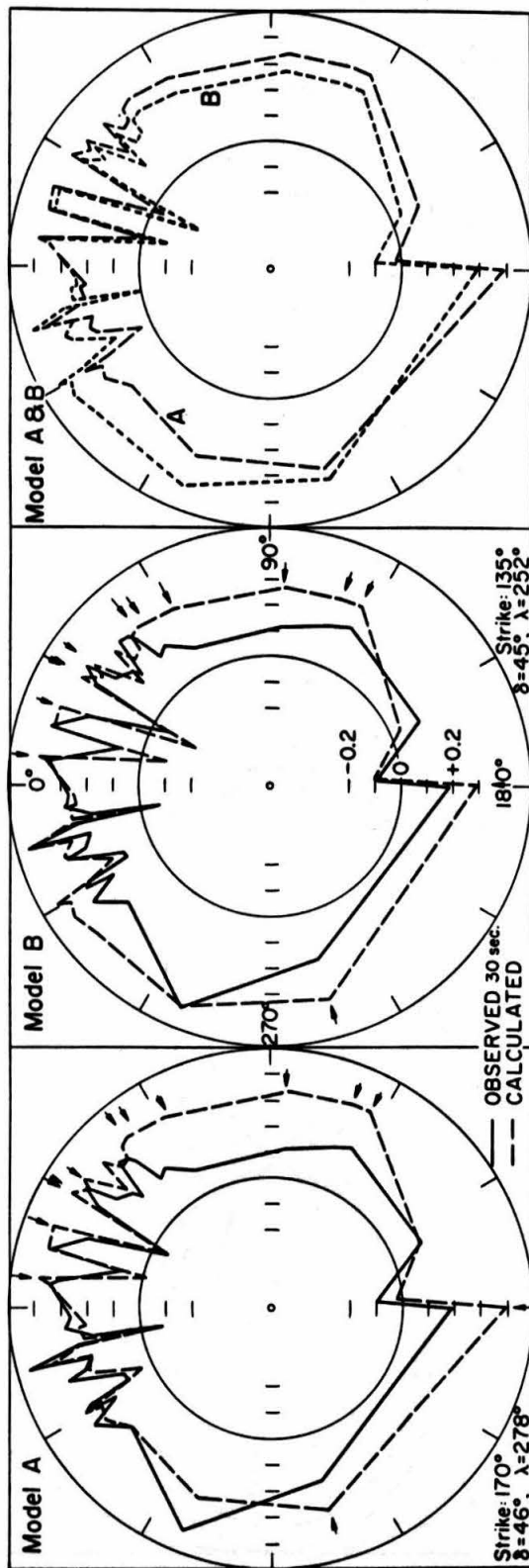


Fig. 6.6

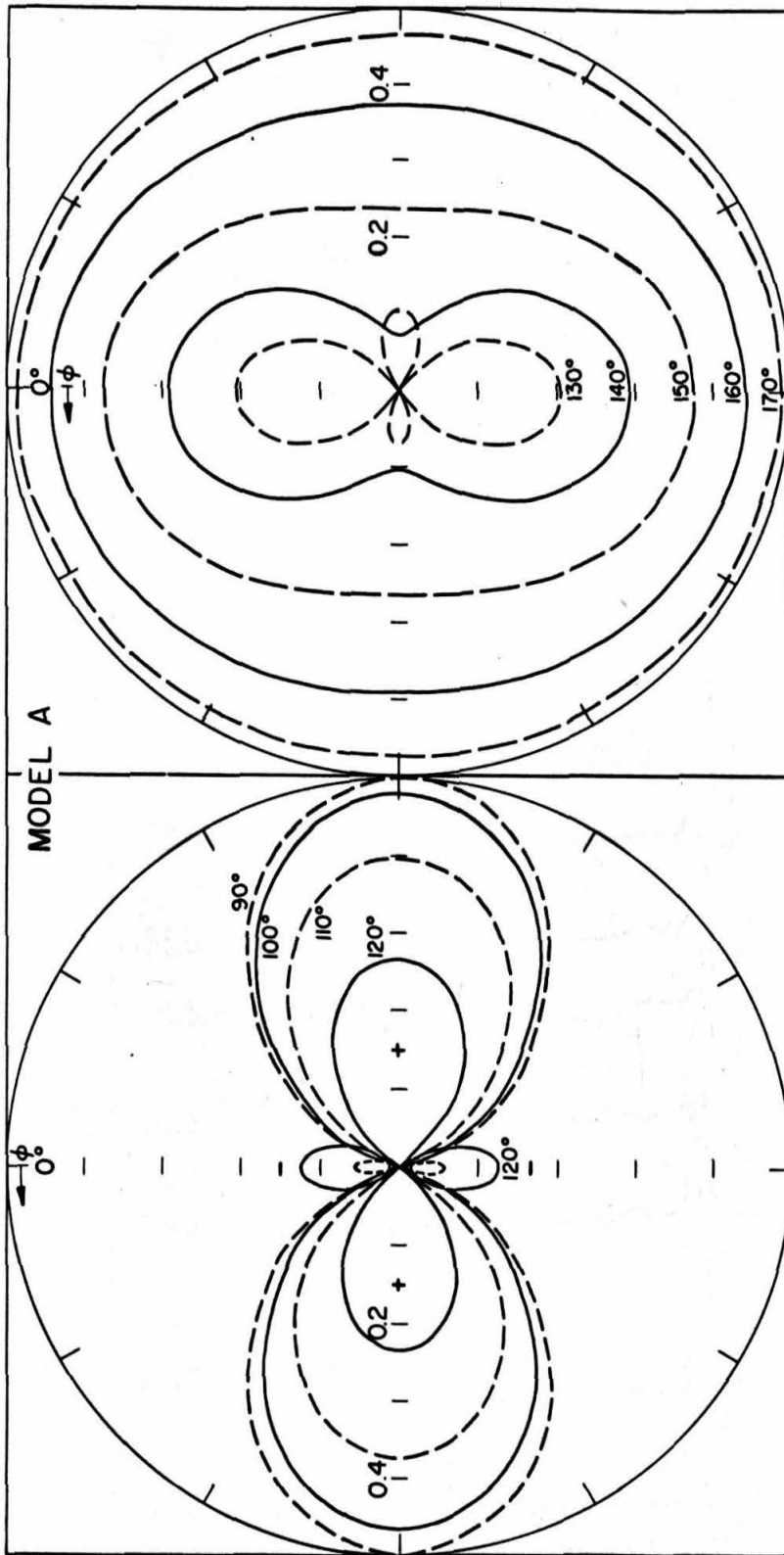


Fig. 6.7

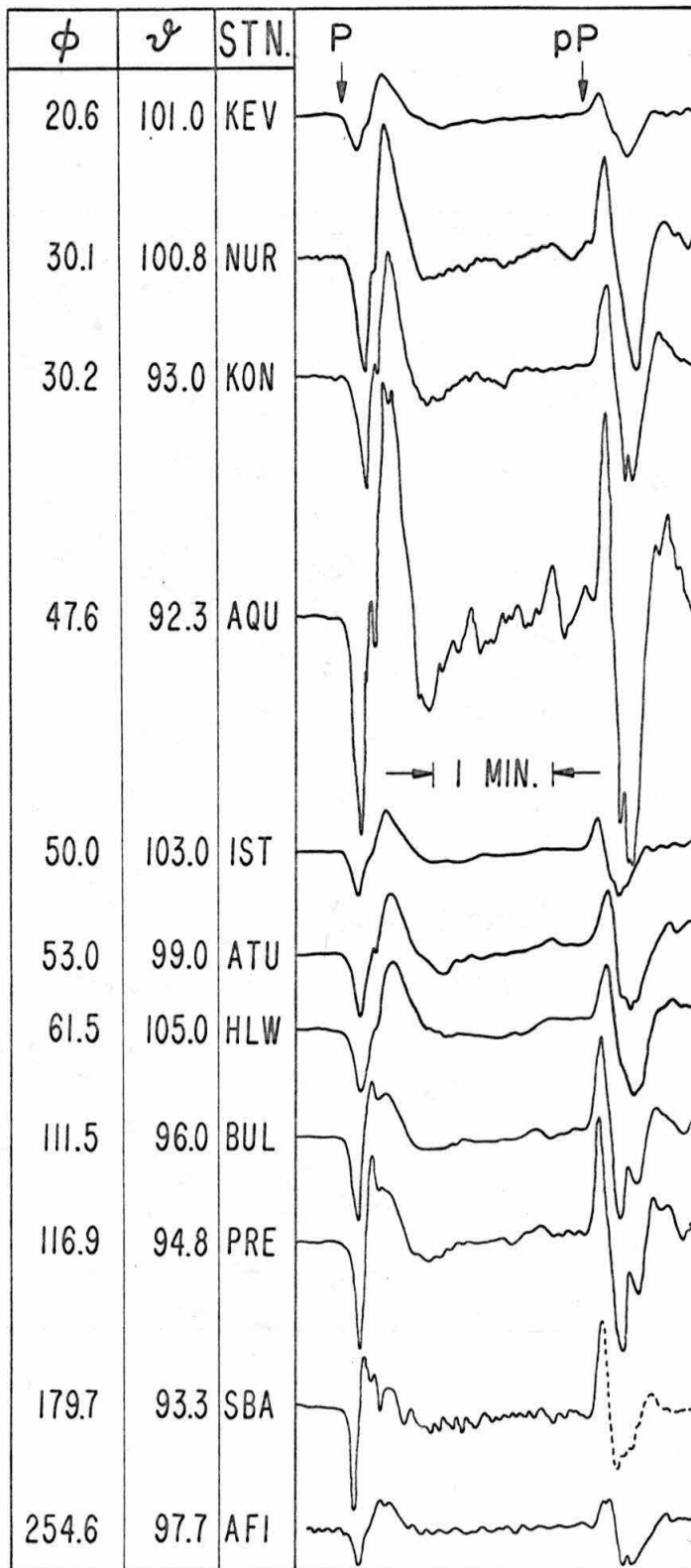


Fig. 6.8

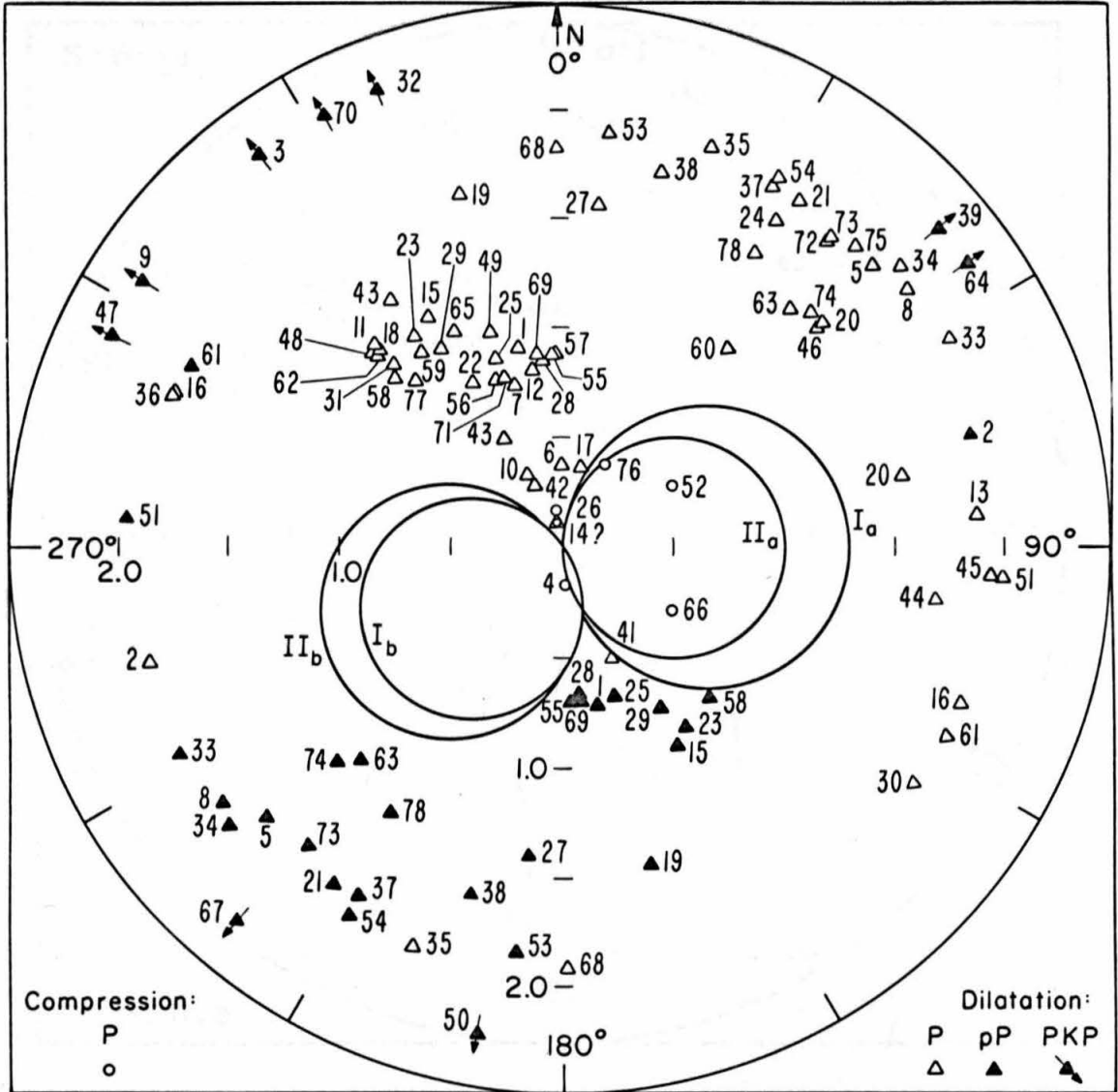


Fig. 6.9

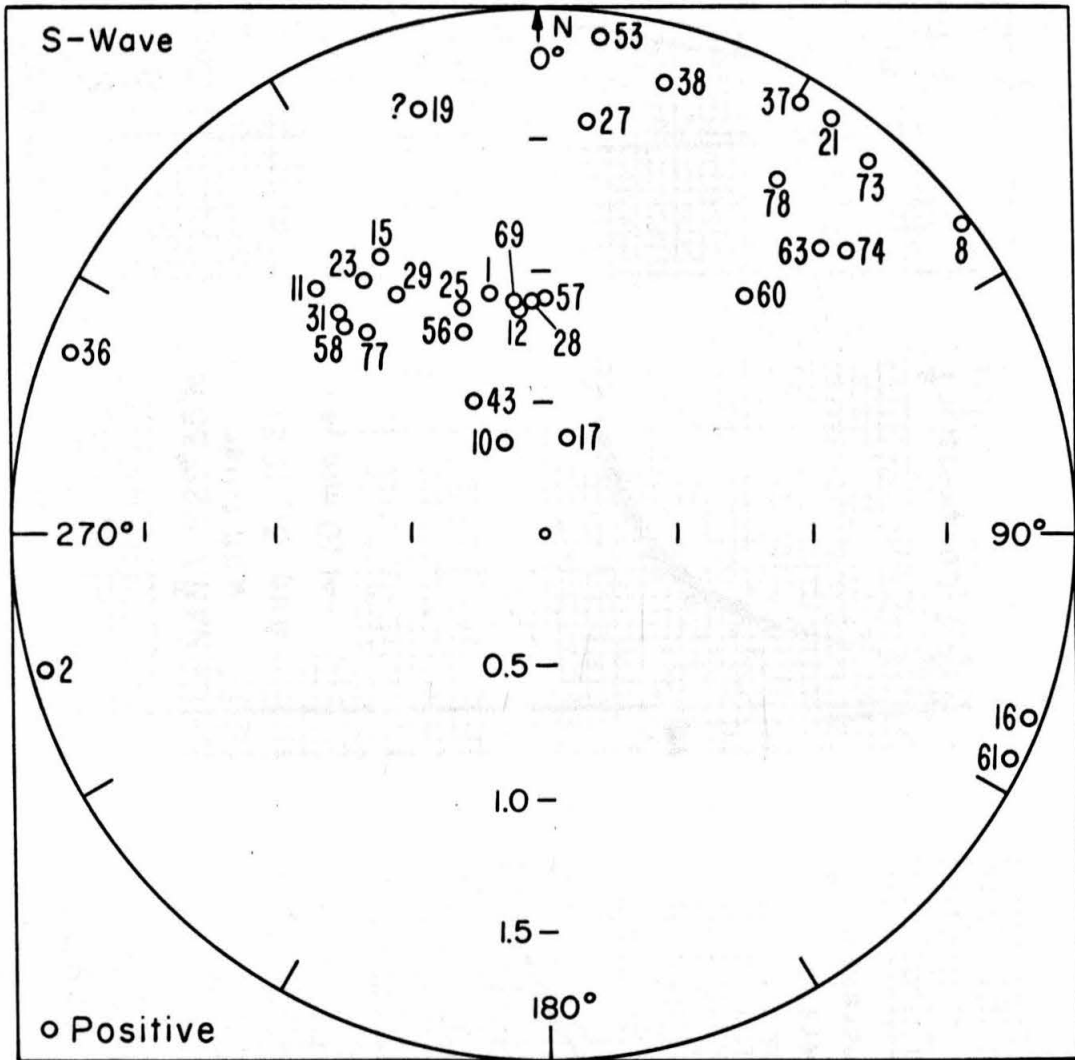


Fig. 6.10

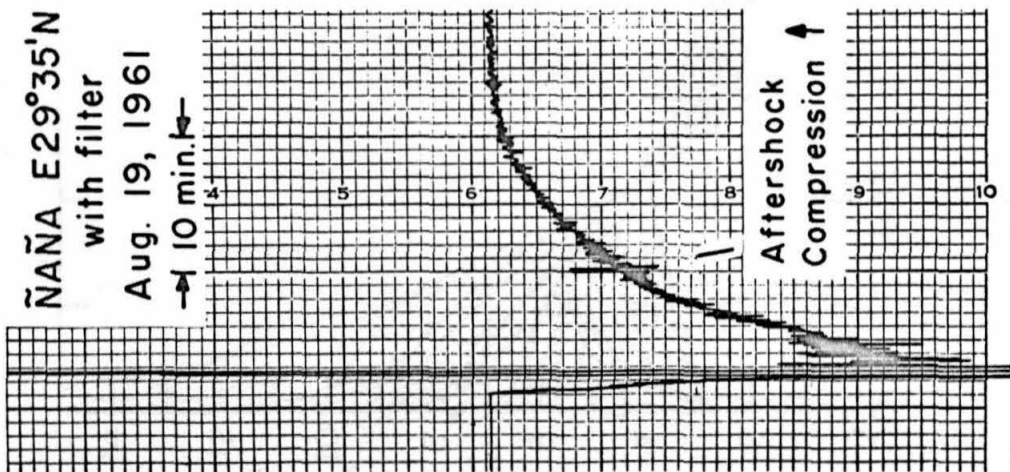
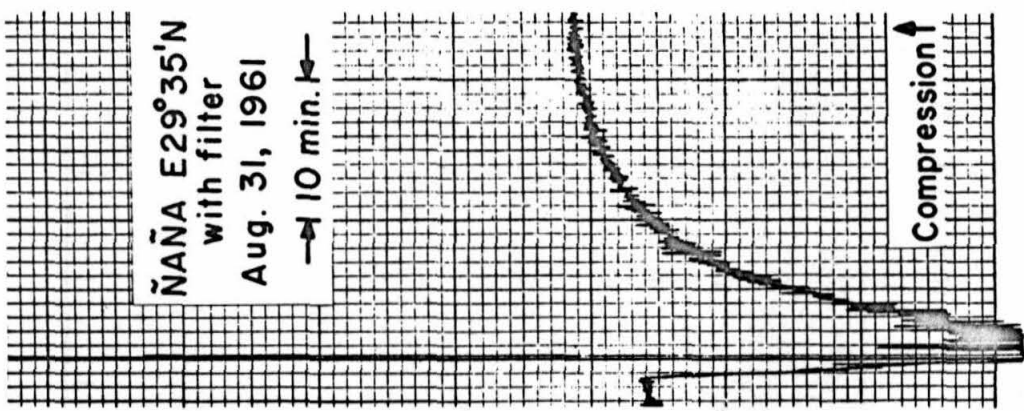
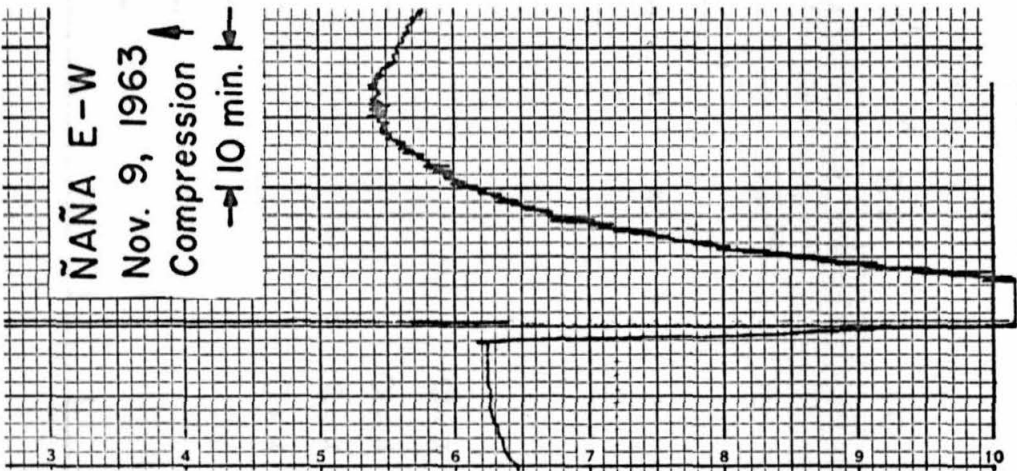


Fig. 6.11

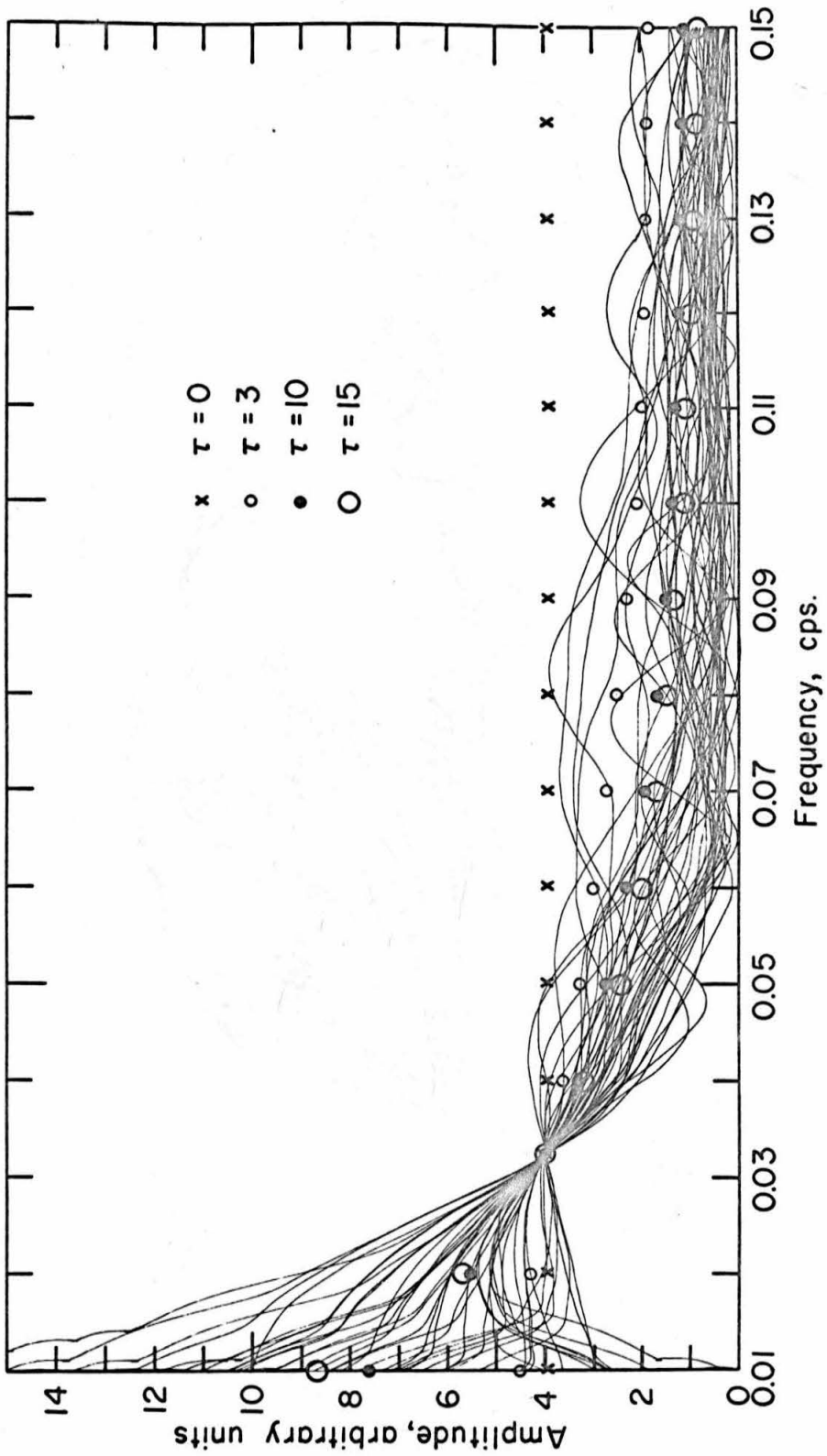


Fig. 6.12

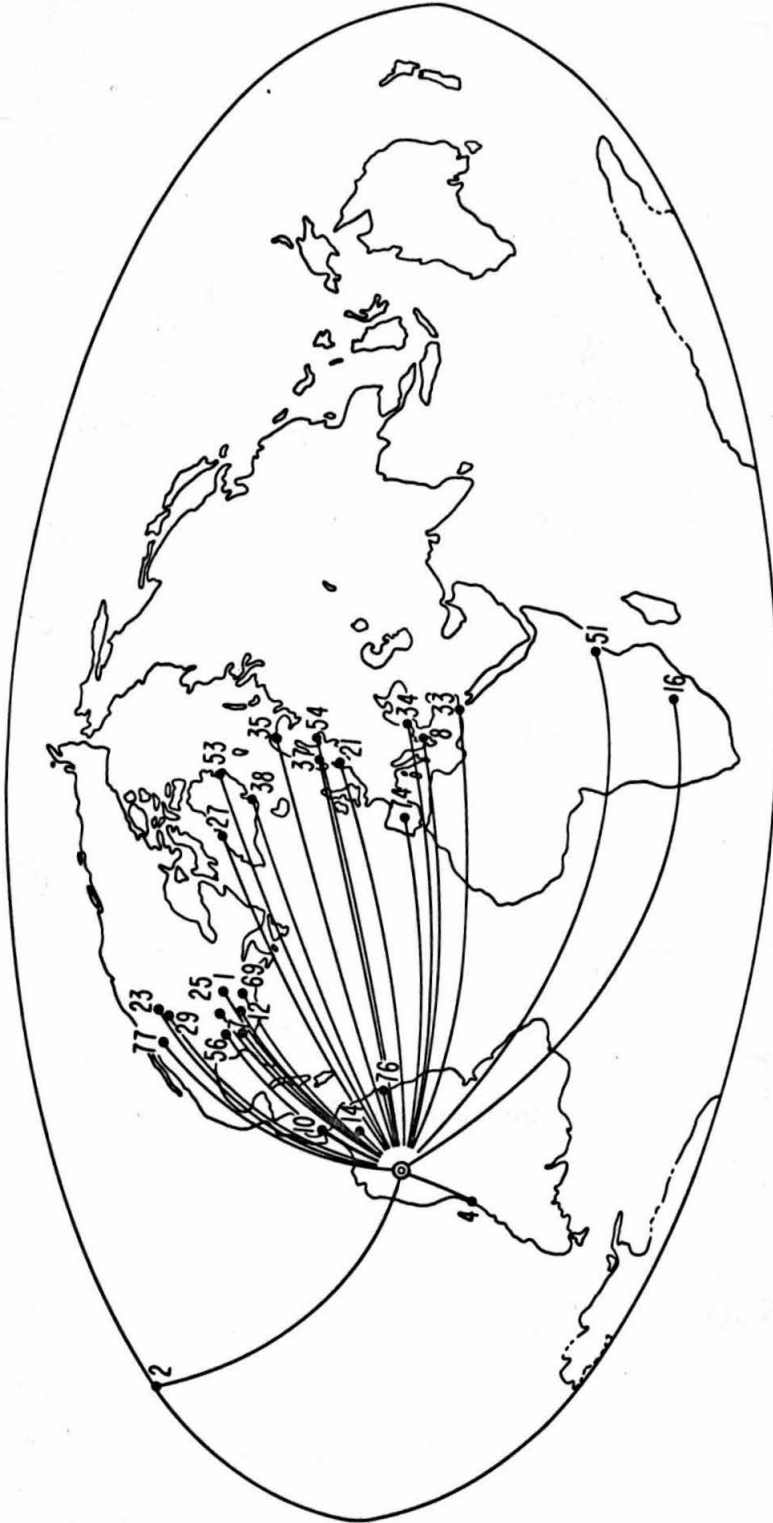


Fig. 7.1

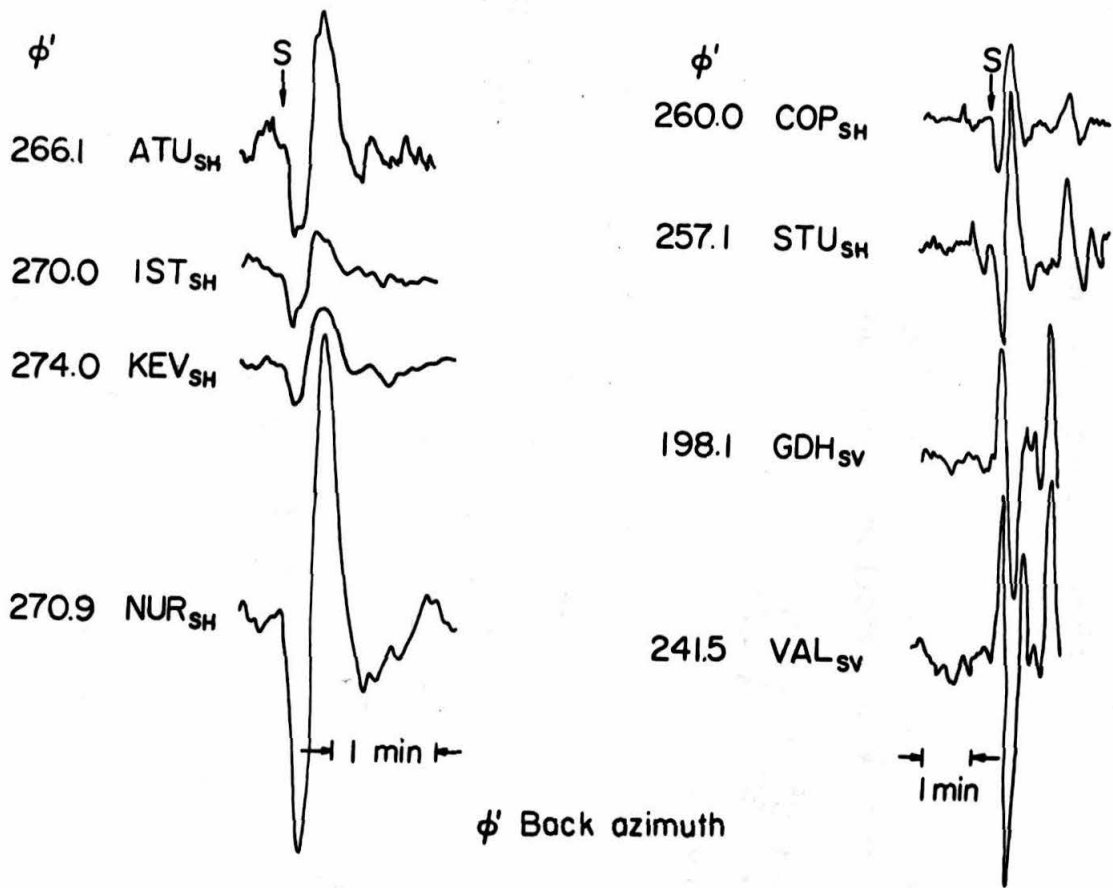


Fig. 7.2

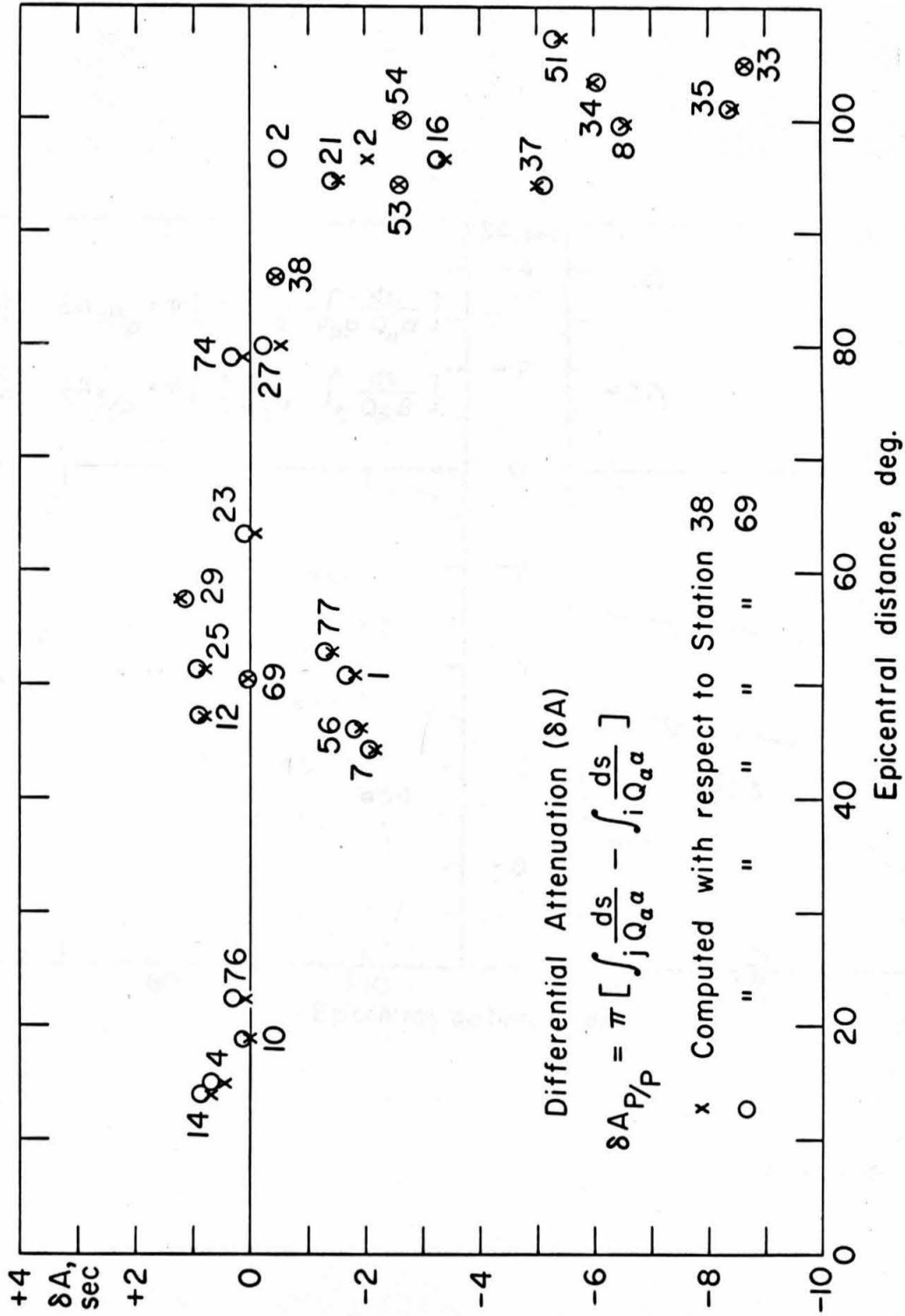


Fig. 7.3

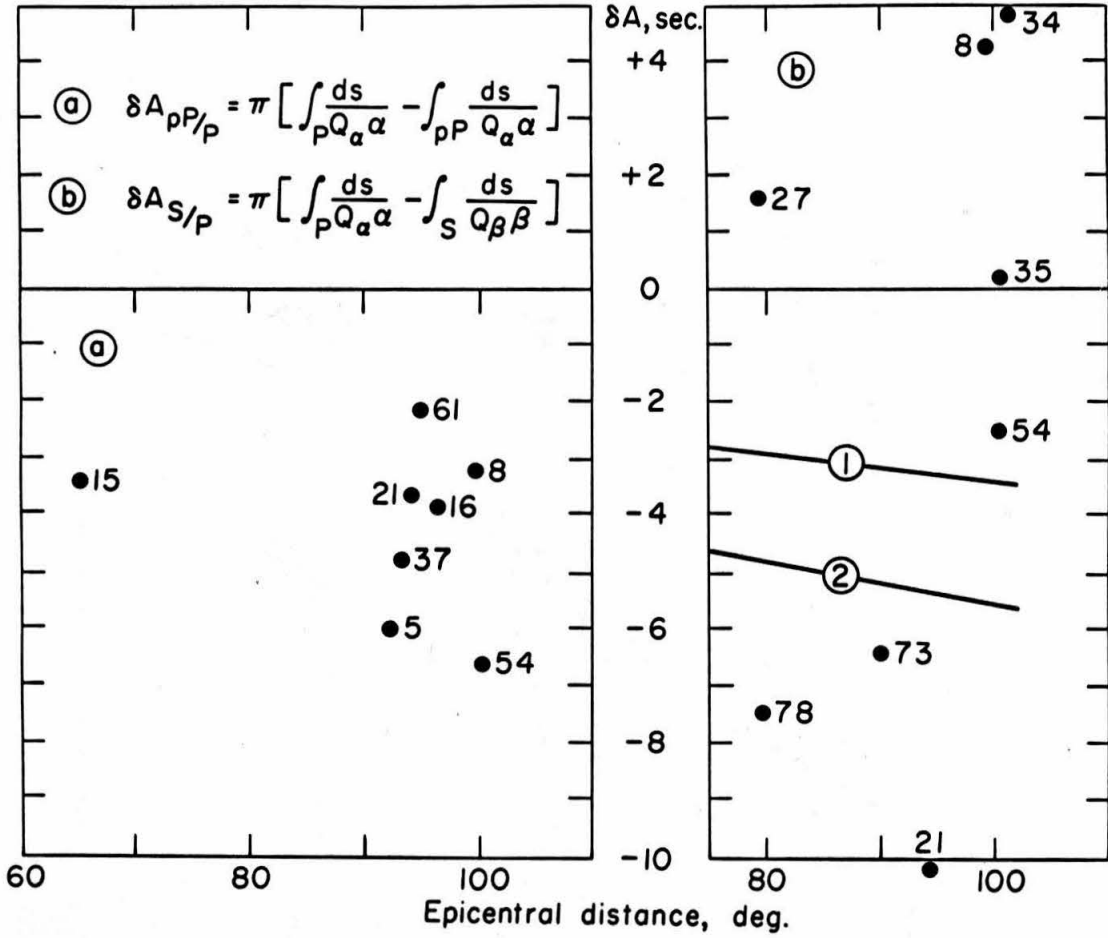


Fig. 7.4

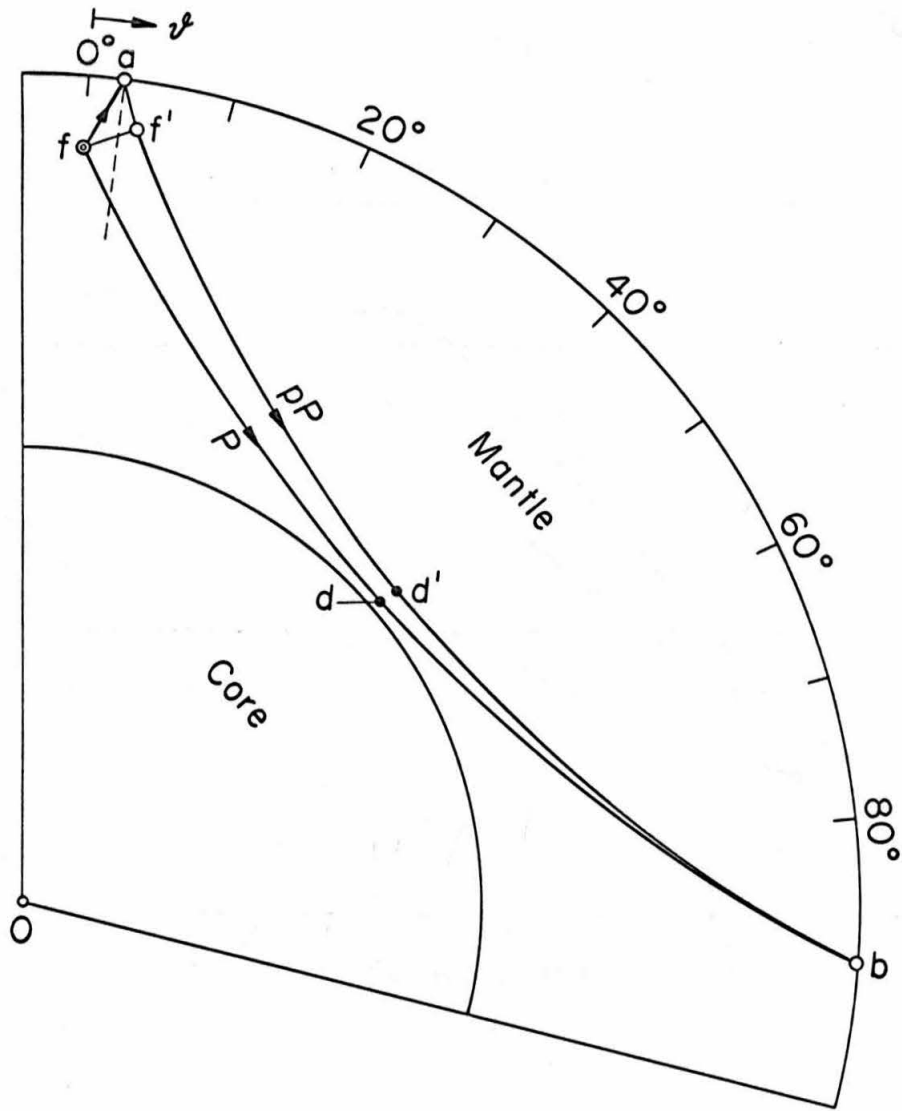


Fig. 7.5

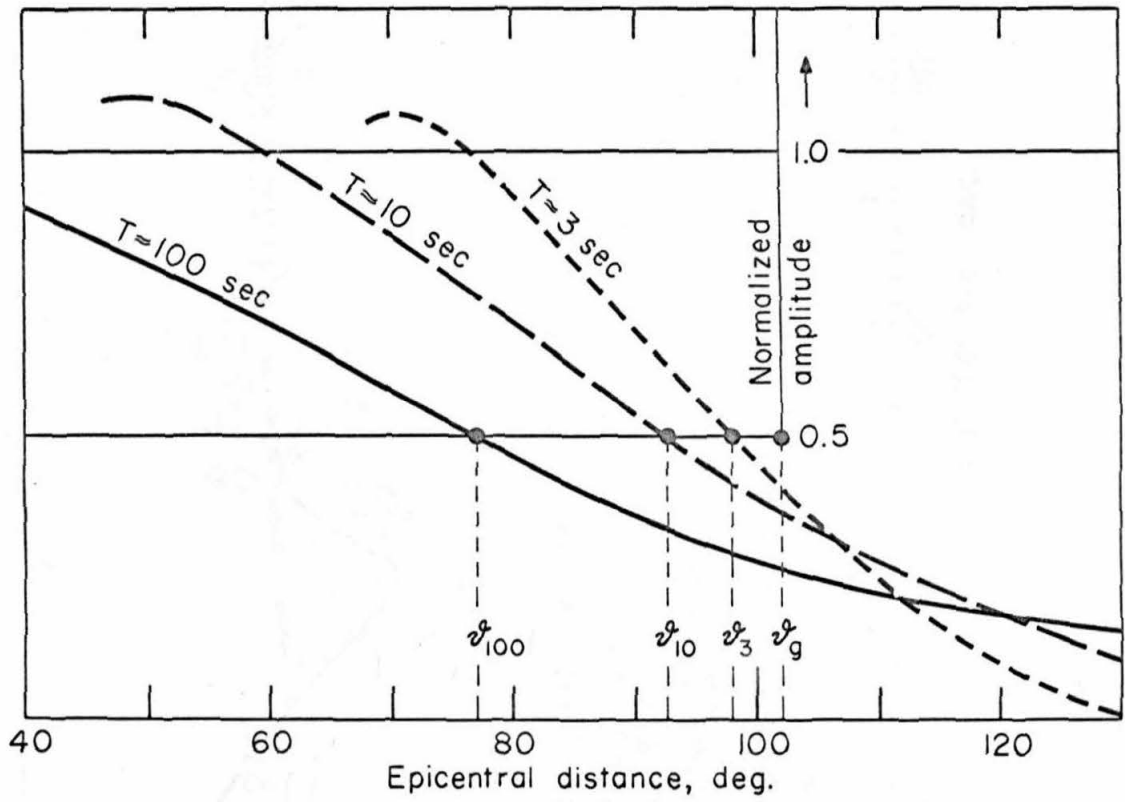


Fig. 7.6

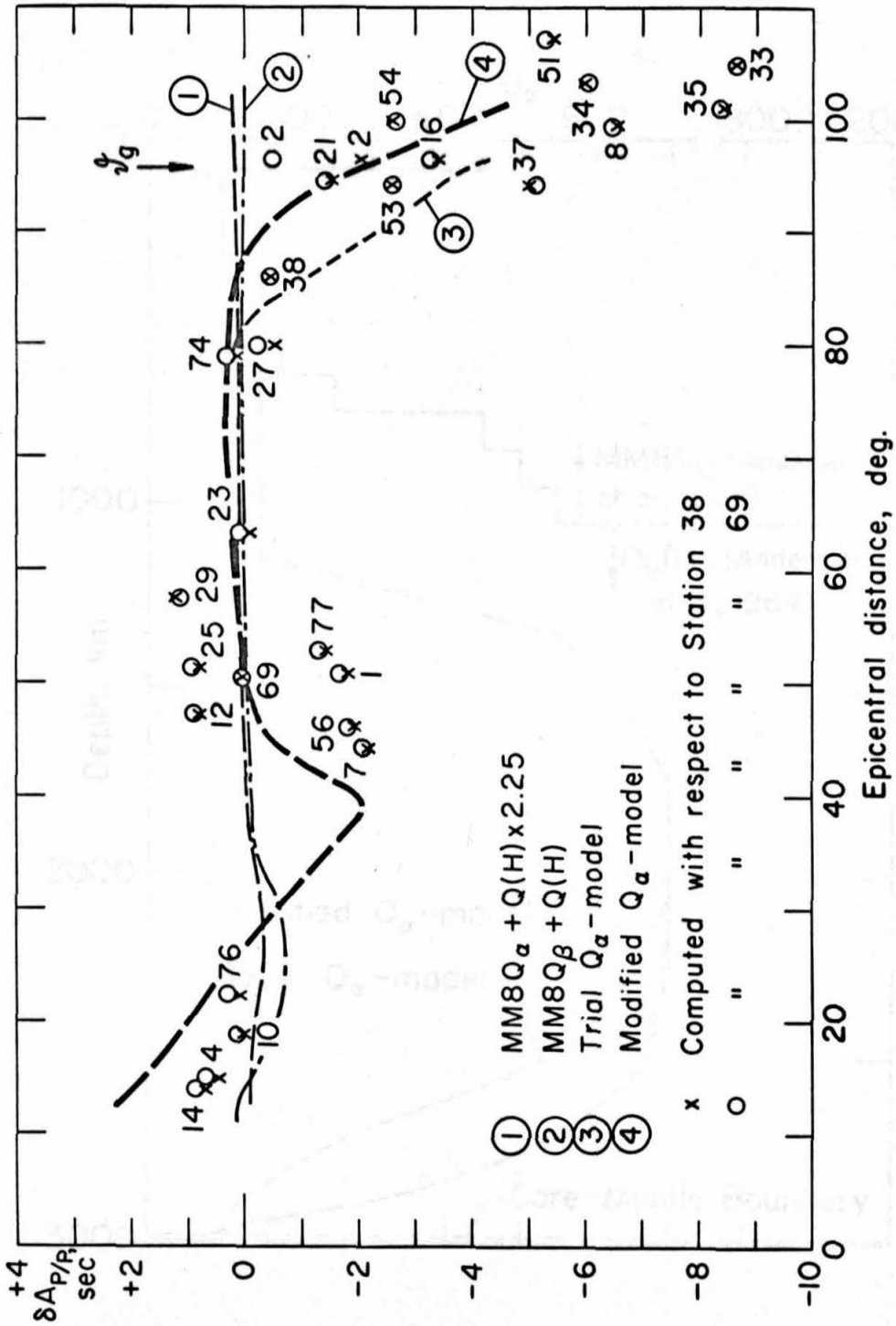


Fig. 7.7

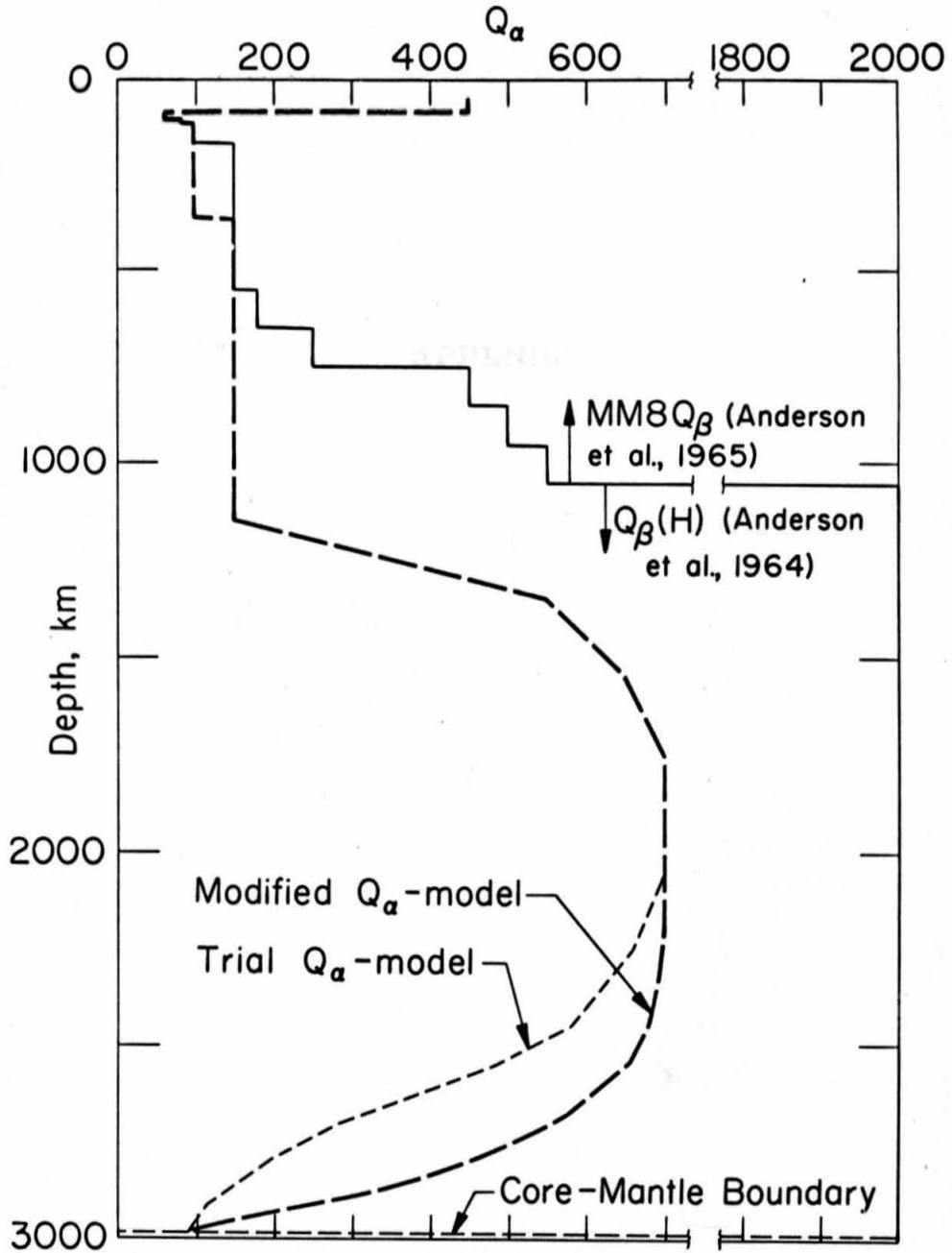


Fig. 7.8

APPENDIX

APPENDIX 1  
SOME VECTOR AND DYADIC IDENTITIES

We shall give proofs to some vector and dyadic identities used in Chapter 2. It is sufficient to prove them in cartesian coordinates.

$$1. \nabla \cdot [\vec{F} (\nabla \cdot \mathcal{Q})] = \vec{F} \cdot [\nabla (\nabla \cdot \mathcal{Q})] + (\nabla \cdot \vec{F}) (\nabla \cdot \mathcal{Q})$$

By definition, a dyadic  $\mathcal{Q}$  can be written as

$$\begin{aligned} \mathcal{Q} &= \vec{e}_1 (g_{11} \vec{e}_1 + g_{12} \vec{e}_2 + g_{13} \vec{e}_3) \\ &\quad + \vec{e}_2 (g_{21} \vec{e}_1 + g_{22} \vec{e}_2 + g_{23} \vec{e}_3) \\ &\quad + \vec{e}_3 (g_{31} \vec{e}_1 + g_{32} \vec{e}_2 + g_{33} \vec{e}_3) \\ &= \vec{e}_1 \vec{g}_1 + \vec{e}_2 \vec{g}_2 + \vec{e}_3 \vec{g}_3 \\ &= \vec{e}_i \vec{g}_i \quad (i = 1, 2, 3) \end{aligned} \tag{A1.1}$$

where the  $\vec{g}$ 's are the row vectors of the matrix of  $\mathcal{Q}$ . It then follows that

$$\nabla \cdot \mathcal{Q} = \frac{\partial}{\partial x_i} \vec{g}_i \tag{A1.2}$$

With (A1.2), we have the left-hand side.

$$\begin{aligned}
 \nabla \cdot [\vec{F}(\nabla \cdot \mathcal{Q})] &= \left( \vec{e}_i \frac{\partial}{\partial x_i} \right) \cdot \left[ (F_j \vec{e}_j) \left( \frac{\partial}{\partial x_k} \vec{g}_k \right) \right] \quad i, j, \text{ and } k = 1, 2, 3 \\
 &= \frac{\partial}{\partial x_i} \left( F_i \frac{\partial}{\partial x_k} \vec{g}_k \right) \\
 &= F_i \left[ \frac{\partial}{\partial x_i} \left( \frac{\partial}{\partial x_k} \vec{g}_k \right) \right] + \left( \frac{\partial}{\partial x_i} F_i \right) \left( \frac{\partial}{\partial x_k} \vec{g}_k \right) \\
 &= \vec{F} \cdot [\nabla(\nabla \cdot \mathcal{Q})] + (\nabla \cdot \vec{F})(\nabla \cdot \mathcal{Q})
 \end{aligned}$$

which is equal to the right-hand side.

$$2. \quad \nabla \cdot (\vec{F} \times \nabla \times \mathcal{Q}) = (\nabla \times \vec{F}) \cdot (\nabla \times \mathcal{Q}) - \vec{F} \cdot (\nabla \times \nabla \times \mathcal{Q})$$

Following (A1.1), we write for a dyadic  $\mathcal{H}$

$$\mathcal{H} = \vec{e}_i \vec{h}_i \quad (\text{A1.3})$$

where the  $\vec{h}$ 's are the row vectors of the matrix  $\mathcal{H}$ . We then have

$$\begin{aligned}
 \nabla \cdot (\vec{F} \times \mathcal{H}) &= \left( \vec{e}_i \frac{\partial}{\partial x_i} \right) \cdot [(F_j \vec{e}_j) \times (\vec{e}_k \vec{h}_k)] \\
 &= \frac{\partial}{\partial x_i} (F_j \vec{h}_k) \epsilon_{ijk} \\
 &= \left[ -F_i \left( \frac{\partial}{\partial x_j} \vec{h}_k \right) + \left( \frac{\partial}{\partial x_i} F_j \right) \vec{h}_k \right] \epsilon_{ijk} \\
 &= (\nabla \times \vec{F}) \cdot \mathcal{H} - \vec{F} \cdot (\nabla \times \mathcal{H}) \quad (\text{A1.4})
 \end{aligned}$$

where  $\epsilon_{ijk}$  is the permutation symbol.

Since curl of a dyadic is still a dyadic, we therefore put

$$\mathfrak{H} = \nabla \times \mathfrak{Q} \quad (\text{A1.5})$$

and substitute (A1.5) into (A1.4), which gives

$$\nabla \cdot (\vec{F} \times \nabla \times \mathfrak{Q}) = (\nabla \times \vec{F}) \cdot (\nabla \times \mathfrak{Q}) - \vec{F} \cdot (\nabla \times \nabla \times \mathfrak{Q})$$

$$3. \quad \nabla^2 \mathfrak{Q} = \nabla(\nabla \cdot \mathfrak{Q}) - \nabla \times \nabla \times \mathfrak{Q}$$

By definition, we have

$$\begin{aligned} \nabla \times \mathfrak{Q} &= \vec{e}_i \frac{\partial}{\partial x_i} \mathfrak{Q} \\ &= \vec{e}_i \times \frac{\partial}{\partial x_i} \vec{g}_k \epsilon_{ijk} \end{aligned} \quad (\text{A1.6})$$

With (A1.2) and (A1.6), we write the right-hand side

$$\begin{aligned} \nabla(\nabla \cdot \mathfrak{Q}) - \nabla \times \nabla \times \mathfrak{Q} &= \vec{e}_1 \left[ \frac{\partial^2}{\partial x_1^2} \vec{g}_1 + \frac{\partial^2}{\partial x_1 \partial x_2} \vec{g}_2 + \frac{\partial^2}{\partial x_1 \partial x_3} \vec{g}_3 \right] \\ &+ \vec{e}_2 \left[ \frac{\partial^2}{\partial x_2 \partial x_1} \vec{g}_1 + \frac{\partial^2}{\partial x_2^2} \vec{g}_2 + \frac{\partial^2}{\partial x_2 \partial x_3} \vec{g}_3 \right] \\ &+ \vec{e}_3 \left[ \frac{\partial^2}{\partial x_3 \partial x_1} \vec{g}_1 + \frac{\partial^2}{\partial x_3 \partial x_2} \vec{g}_2 + \frac{\partial^2}{\partial x_3^2} \vec{g}_3 \right] \\ &+ \vec{e}_1 \left[ \frac{\partial}{\partial x_2} \left( \frac{\partial}{\partial x_1} \vec{g}_2 - \frac{\partial}{\partial x_2} \vec{g}_1 \right) - \frac{\partial}{\partial x_3} \left( \frac{\partial}{\partial x_3} \vec{g}_1 - \frac{\partial}{\partial x_1} \vec{g}_3 \right) \right] \\ &+ \vec{e}_2 \left[ \frac{\partial}{\partial x_3} \left( \frac{\partial}{\partial x_2} \vec{g}_3 - \frac{\partial}{\partial x_3} \vec{g}_2 \right) - \frac{\partial}{\partial x_1} \left( \frac{\partial}{\partial x_1} \vec{g}_2 - \frac{\partial}{\partial x_2} \vec{g}_1 \right) \right] + \end{aligned}$$

$$\begin{aligned} & + \vec{e}_3 \left[ \frac{\partial}{\partial x_1} \left( \frac{\partial}{\partial x_3} \vec{g}_1 - \frac{\partial}{\partial x_1} \vec{g}_3 \right) - \frac{\partial}{\partial x_2} \left( \frac{\partial}{\partial x_2} \vec{g}_3 - \frac{\partial}{\partial x_3} \vec{g}_2 \right) \right] \\ & = \left( \frac{\partial^2}{\partial x_1^2} + \frac{\partial^2}{\partial x_2^2} + \frac{\partial^2}{\partial x_3^2} \right) (\vec{e}_i \vec{g}_i) \\ & = \nabla^2 \mathfrak{q} \end{aligned}$$

which is the left-hand side.

APPENDIX 2

LIST OF SYMBOLS USED IN THE TEXT

<u>Symbol</u>	<u>Definition</u>	<u>First Introduced in Section</u>
$\alpha$	longitudinal velocity	2.1
$\beta$	transverse velocity	
$\vec{q}$	body force density	
$\vec{f}$	arbitrary vector field	
$\vec{Q}$	Fourier transform of $\vec{q}$	
$\vec{F}$	Fourier transform of $\vec{f}$ , or the observed spectrum	
$\lambda, \mu$	Lame's constants	
$\rho$	density	
$\omega$	angular frequency	
$l$	subscript denoting longitudinal part	
$t$	subscript denoting transverse part	
$k$	wave number, $= \omega/v$	
$k_\alpha$	longitudinal wave number, $= \omega/\alpha$	
$k_\beta$	transverse wave number, $= \omega/\beta$	
$\mathcal{G}$	Green's dyadic for elastodynamics	2.2
$\mathcal{D}$	a dyadic operator defined by (2.15)	
$\delta(\vec{r})$	spatial delta function	
$\mathcal{I}$	idemfactor	
$\mathcal{E}$	a dyadic	2.3
$\vec{n}$	outward normal vector	
$\vec{r}$	position vector of a field point	
$\vec{r}'$	position vector of a source point	

<u>Symbol</u>	<u>Definition</u>	<u>First Introduced In Section</u>
$g$	scalar Green's function	2.4.1
$r, \theta, \phi$	spherical coordinates	
$\vec{e}_r, \vec{e}_\theta, \vec{e}_\phi$	unit vectors of the spherical coordinates	
$V$	volume of a domain	2.4.2
$dv$	volume element of $V$	
$S$	surface enclosing $V$	
$ds$	surface element of $S$ , or source area	
$\vec{U}_0$	source displacement	
$\vec{U}$	displacement field	
$x_1, x_2, x_3$	cartesian coordinates	
$\vec{e}_1, \vec{e}_2, \vec{e}_3$	unit vectors of the cartesian coordinates	
$\vec{a}$	an arbitrary unit vector	2.4.2.a
$L_0$	strength of source displacement	
$\tau$	time constant of the build-up step source	
$P, SH, SV$	subscripts denoting longitudinal, horizontally polarized transverse, and vertically polarized transverse wave motions, respectively	
$A_s(\theta, \phi)$	spatial radiation pattern	2.4.2.c
$\lambda, \delta$	slip and dip angles of the fault-plane source	
$b$	$= \frac{1}{2}(1 - 2\sigma)$	
$S_0$	$= 1/(3 - 4\sigma)$	
$\sigma$	Poisson's ratio	
$f_0$	strength of the body force	2.4.3
$\vec{U}^s$	displacement field due to a single force	

<u>Symbol</u>	<u>Definition</u>	<u>First Introduced in Section</u>
$\vec{U}^c$	displacement field due to a couple force	2.4.3
$F_o$	$= \int_V f_o dv$ , the total force inside $V$	
$\xi_1, \xi_2, \xi_3$	curvilinear coordinates	
$d$	separation of two opposite single forces	
$C$	arbitrary constant	
$dl$	line element	2.4.4
$u$	scalar wave function	3.1
$c$	phase velocity	
$k_o$	$= \omega/c$ , wave number	
$A(\vec{x})$	amplitude function	
$S(\vec{x})$	phase function	
$\vec{A}$	amplitude of vector wave function	
$\vec{A}_n, n=0,1,2,\dots$	coefficients of power expansion of $\vec{A}$	
$a_o$	$=  \vec{A}_o  /  \nabla S $	
$s_1, s_2$	two arbitrary points on a ray	
$\Sigma, \Sigma_1, \Sigma_2, \Sigma_3$	cross-sections of a ray tube	
$d\sigma, d\sigma_1, d\sigma_2$	surface elements of $\Sigma, \Sigma_1, \Sigma_2$ , respectively	
$K, K_1, K_2$	arbitrary constants	
$\vec{p}$	unit normal of a space curve	
$\vec{b}$	unit binormal of a space curve	
$\epsilon_o$	arbitrary initial phase	
$\epsilon_1$	phase change between $s_1$ and $s_2$	
$T$	radius of torsion of a ray	

<u>Symbol</u>	<u>Definition</u>	<u>First Introduced in Section</u>
$\vec{c}_1, \vec{c}_2$	arbitrary constant vectors	3.2
$p$	ray parameter	
$\Delta$	defined in Figure 3.1, the epicentral distance	
$G_P, G_S$	geometrical spreading factors for P and S waves	
$AT(\omega)$	damping factor, defined by (3.51)	3.3
$Q$	anelasticity of the earth	
$t^*$	imaginary part of travel time, defined by (3.53)	
$\eta$	$= r/v$	
$\theta_s$	$= \pi - \theta$	
$\theta, \theta_0$	take-off angle and incident angle of a ray	
$u_0, v_0, w_0$	surface displacements along $x_1, x_2$ and $x_3$ directions, respectively	3.4
$r_c$	radius of the earth's core	
$\Gamma_t$	transmission coefficient of a layered system	
$\Gamma_r$	reflection coefficient of a layered system	
$J_{ij}$	elements of Thomson-Haskell matrix	
$\Xi$	dilatational displacement potential	3.5
$m$	$= \beta/\alpha$	
$\sigma_j$	$j$ th root of $H_{1/3}^{(2)}(\sigma e^{\pi i}) = 0$	
$q_j$	$= (3\sigma_j/k_\alpha r)^{1/3} e^{5\pi i/6}$	
$\delta_j$	$j$ th root of equation (3.67)	
$\alpha', \rho'$	longitudinal velocity and density inside the earth's core	

<u>Symbol</u>	<u>Definition</u>	<u>First Introduced in Section</u>
$F_{PcS}(\omega)$	observed spectrum of a PcS wave	4.1
$H_{MC}(\omega)$	transfer function for wave propagating inside mantle or core	
$H_{CM}(\omega)$	transfer function accounting for the reflection off the core-mantle boundary	
$H_{CR}(\omega)$	transfer function for the crust	
$H_{INS}(\omega)$	transfer function for the instrument	
$S(\omega)$	source spectrum	
$H_{DF}(\omega)$	transfer function for the diffracted path	
$A(\omega), \Phi(\omega)$	observed amplitude and phase spectrums	
$A_o(\omega), \Phi_o(\omega)$	source amplitude and phase spectrums	
$A_{MC}(\omega), A_{CM}(\omega), A_{CR}(\omega), A_{INS}(\omega), A_{DF}(\omega)$	amplitude of the corresponding transfer function.	
$\Phi_{MC}(\omega), \Phi_{CM}(\omega), \Phi_{CR}(\omega), \Phi_{INS}(\omega), \Phi_{DF}(\omega)$	phases of the corresponding transfer function	
$T_o$	period of pendulum of the instrument	
$T_g$	period of galvanometer of the instrument	
$\omega_o$	$= 2\pi/T_o$	
$\omega_g$	$= 2\pi/T_g$	
$M$	peak magnification of the instrument	4.2
$G$	geometrical spreading factor	
$n(\omega)$	mode number function	
$r_o$	radius of the earth	
$\Delta$	$= r_o \delta$ epicentral distance in km	

<u>Symbol</u>	<u>Definition</u>	<u>First Introduced in Section</u>
$t_0$	difference between the origin time and the first arrival of a signal	4.2
$g(t)$	source time function	5.5
$M_a$	absolute moment	
$M_N$	net moment	
$E$	total energy release	
$A_t(\omega)$	source amplitude spectrum	7.2
$R(f)$	reduced spectral ratio	
$\delta A$	$= \pi \left[ \int_j \frac{ds}{Q_v} - \int_i \frac{ds}{Q_v} \right]$ , differential attenuation	
$c_1$	a constant of frequency, defined by (7.5)	
$\delta A_{P/P}$	differential attenuation based on reduced spectral ratio of two P waves observed at different stations	7.3
$\delta A_{pP/P}$	differential attenuation based on reduced spectral ratio of pP and P waves observed at the same station	
$\delta A_{S/P}$	differential attenuation based on reduced spectral ratio of S and P waves observed at the same station	
$\bar{Q}_a$	average $Q_a$ in the upper 430 km of the mantle	7.4

APPENDIX 3

COMPUTATIONS CONCERNING SEISMIC RAYS

In the following we shall describe a numerical method which computes the integrals of travel-time, distance, attenuation, and geometrical spreading for a spherically symmetric earth.

First note that the integral for  $t^*$  (3.54) is mathematically equivalent to that for  $t$  (3.45) if a transformation  $u = Qv$  is performed. So the result obtained for  $t$  applies equally well to  $t^*$ .

For a ray taking off at an angle  $\theta$  from a source at  $r = r_h$  reaching the deepest point  $r = r_d$  and arriving at the earth's surface  $r = r_o$ , the following formulas hold:

$$t = 2 \int_{r_d}^{r_h} \eta^2 r^{-1} (\eta^2 - p^2)^{-\frac{1}{2}} dr + \int_{r_h}^{r_o} \eta^2 r^{-1} (\eta^2 - p^2)^{\frac{1}{2}} dr \quad (A3.1)$$

$$\Delta = 2p \int_{r_d}^{r_h} r^{-1} (\eta^2 - p^2)^{-\frac{1}{2}} dr + p \int_{r_h}^{r_o} r^{-1} (\eta^2 - p^2)^{-\frac{1}{2}} dr \quad (A3.2)$$

$$\frac{d\Delta}{dp} = -\xi_o (\eta_o^2 - p^2)^{-\frac{1}{2}} + I \quad (A3.3)$$

where

$$\eta = \frac{r}{v(r)}$$

$$p = \frac{r \sin \theta}{v(r)}$$

$$\xi = 2 \frac{d \ln r}{d \ln \eta}$$

$$I = 2 \int_{\xi_d}^{\xi_h} (\eta^2 - p^2)^{-\frac{1}{2}} d\xi + \int_{\xi_h}^{\xi_o} (\eta^2 - p^2)^{-\frac{1}{2}} d\xi \quad (\text{A3.4})$$

For a given numerical function  $v$ , the integrals in (A3.1), (A3.2) and (A3.3) can be evaluated conveniently by dividing the earth into many concentric spherical shells. Within each shell  $v$  is approximated by a linear function of  $r$ . In so doing, the contributions of these integrals in each shell can be obtained analytically and the sum of these corresponding contributions gives the desired values of these integrals.

Suppose that the  $i$ th shell is bounded above by  $r_{i+1}$  with velocity  $v_{i+1}$ , and is bounded below by  $r_i$  with velocity  $v_i$ . Within the  $i$ th shell the velocity varies linearly as

$$v = ar + b \quad (\text{A3.5})$$

where

$$a = \frac{v_{i+1} - v_i}{r_{i+1} - r_i}$$

$$b = -ar_i + v_i$$

By (A3.5), it follows that

$$\xi = \frac{2}{b} (ar + b) \quad (\text{A3.6})$$

Let the contributions of (A3.1), (A3.2), and (A3.4) be  $t_i$ ,  $\delta_i$  and  $I_i$  within the  $i$ th shell. Putting (A3.5), (A3.6) into (A3.1), (A3.2) and

(A3.4), the integrals are just elementary ones and can be easily carried out in closed forms.

Before giving the results, we shall first define the following:

$$c \equiv 1 - a^2 p^2$$

$$d \equiv -2abp^2$$

$$e \equiv -p^2 b^2$$

$$f = (d^2 - 4ce)^{\frac{1}{2}} = 2bp \geq 0$$

$$X \equiv \frac{r}{ar + b}$$

$$Y \equiv \frac{b}{ar + b} \tag{A3.7}$$

$$Z \equiv \left(1 - \frac{2}{x}\right)^{\frac{1}{2}}$$

$$W \equiv (Cr^2 + dr + e)^{\frac{1}{2}}$$

$$J_1 \equiv a^{-1} \left[ \ln |X_{i+1} + (X_{i+1}^2 - p^2)^{\frac{1}{2}}| - \ln |X_i + (X_i^2 - p^2)^{\frac{1}{2}}| \right]$$

$$J_2 \equiv \cos^{-1} \left| \frac{p}{Y_{i+1}} \right| - \cos^{-1} \left| \frac{p}{Y_i} \right|$$

$$I_i = \int_{\xi_i}^{\xi_{i+1}} (\eta^2 - p^2)^{-\frac{1}{2}} d\xi$$

The results are:

1. for  $|a| > \frac{1}{p}$ , or  $c < 0$

$$t_i = -J_1 + (-a^2 c)^{-\frac{1}{2}} \left\{ \sin^{-1} \left[ \frac{(2cr_{i+1} + d)/f}{|f|} \right] - \sin^{-1} \left[ \frac{(2cr_i + d)/f}{|f|} \right] \right\} \quad (\text{A3.8})$$

$$\delta_i = J_2 - ap(-c)^{-\frac{1}{2}} \left\{ \sin^{-1} \left[ \frac{(c - x_{i+1})/(ap|x_{i+1}|)}{|ap|x_{i+1}||} \right] - \sin^{-1} \left[ \frac{(c - x_i)/(ap|x_i|)}{|ap|x_i||} \right] \right\} \quad (\text{A3.9})$$

$$I_i = (c\xi_{i+1}^2 - 4\xi_{i+1} + 4)^{\frac{1}{2}} - (c\xi_i^2 - 4\xi_i + 4)^{\frac{1}{2}} - (-c)^{-\frac{1}{2}} \left[ \sin^{-1} \left( \frac{c\xi_{i+1} - 2}{|2ap|} \right) - \sin^{-1} \left( \frac{c\xi_i - 2}{|2ap|} \right) \right] \quad (\text{A3.10})$$

2. for  $|a| = \frac{1}{p}$ , or  $c = 0$

$$t_i = -J_1 + \frac{2}{ad} \left[ (dr_{i+1} + e)^{\frac{1}{2}} - (dr_i + e)^{\frac{1}{2}} \right] \quad (\text{A3.11})$$

$$\delta_i = J_2 - ap(z_{i+1} - z_i)$$

$$I_i = \frac{a}{3} \left[ (1 - \xi_{i+1})^{3/2} - (1 - \xi_i)^{3/2} \right] - a \left[ (1 - \xi_{i+1})^{\frac{1}{2}} - (1 - \xi_i)^{\frac{1}{2}} \right] \quad (\text{A3.13})$$

3. for  $|a| < \frac{1}{p}$ , or  $c > 0$

$$t_i = -J_1 + (a^2 c)^{-\frac{1}{2}} \left[ \ln |2c^{\frac{1}{2}} W_{i+1} + 2cr_{i+1} + d| \right. \\ \left. - \ln |2c^{\frac{1}{2}} W_i + 2cr_i + d| \right] \quad (A3.14)$$

$$\delta_i = J_2 - apc^{-\frac{1}{2}} \left[ \ln |2c^{\frac{1}{2}}(x_{i+1}^2 - 2x_{i+1} + c)^{\frac{1}{2}} x_{i+1}^{-1} \right. \\ \left. + 2cx_{i+1}^{-1} - 2| - \ln |2c^{\frac{1}{2}}(x_i^2 - 2x_i + c)^{\frac{1}{2}} x_i^{-1} + 2cx_i^{-1} - 2| \right] \quad (A3.15)$$

$$I_i = (c\xi_{i+1}^2 - 4\xi_{i+1} + 4)^{\frac{1}{2}} - (c\xi_i^2 - 4\xi_i + 4)^{\frac{1}{2}} \\ + 2c^{-\frac{1}{2}} \left[ \ln |2c^{\frac{1}{2}}(c\xi_{i+1}^2 - 4\xi_{i+1} + 4)^{\frac{1}{2}} - 2c^{\frac{1}{2}}(c\xi_i^2 - 4\xi_i + 4)^{\frac{1}{2}} \right. \\ \left. + 2c(\xi_{i+1} - \xi_i) \right] \quad (A3.16)$$

If the earth is divided into  $n$  shells between  $r_d \leq r \leq r_h$  and  $m$  shells between  $r_h \leq r \leq r_o$ , then we have the following

$$t = 2 \sum_{i=1}^n t_i + \sum_{i=n}^{n+m} t_i \quad (A3.17)$$

$$\delta = 2 \sum_{i=1}^n \delta_i + \sum_{i=n}^{n+m} \delta_i \quad (A3.18)$$

$$I = 2 \sum_{i=1}^n I_i + \sum_{i=n}^{n+m} I_i \quad (A3.19)$$

Obviously, for  $\theta \leq \pi/2$ ,  $r_d = r_h$ , and the first terms of (A3.17), (A3.18) and (A3.19) vanish. In calculating the geometrical spreading factor, the function  $\theta(\lambda)$  is implicitly given by the result of (A3.18), and the function  $d\theta/d\lambda$  is given by (A3.3).